JET ARRAY IMPINGEMENT HEAT TRANSFER: EFFECTS OF TARGET PLATE DISTANCE, REYNOLDS NUMBER, AND HOLE SPACING

by

Zhong Ren

A THESIS

Submitted in partial fulfillment of the requirements
for the degree of Master of Science in Engineering
in
The Department of Mechanical and Aerospace
Engineering
to
The school of Graduate Studies
of
The University of Alabama in Huntsville

HUNTSVILLE, ALABAMA

2015

In presenting this thesis in partial fulfillment of the requirements for a master's degree from The University of Alabama in Huntsville, I agree that the Library of this University shall make it freely available for inspection. I further agree that permission for extensive copying for scholarly purposes may be granted by my advisor or, in his/her absence, by the Chair of the Department or the Dean of the School of Graduate Studies. It is also understood that due recognition shall be given to me and to The University of Alabama in Huntsville in any scholarly use which may be made of any material in this thesis.

Sep. 21, 2015

(student signature) (date)

THESIS APPROVAL FORM

Submitted by Zhong Ren in partial fulfillment of the requirements for the degree of Master of Science in Mechanical Engineering and accepted on behalf of the Faculty of the School of Graduate Studies by the thesis committee.

We, the undersigned members of the Graduate Faculty of The University of Alabama in Huntsville, certify that we have advised and/or supervised the candidate on the work described in this thesis. We further certify that we have reviewed the thesis manuscript and approve it in partial fulfillment of the requirements for the degree of Master of Science in Mechanical Engineering.

09/21/2015
Committee Chair
Dr. Phillip Ligrani (Date)

10/1/2015
Dr. George Nelson

10/1/2015
Dr. Babak Shotorban

Department Chair
Dr. Keith Hollingsworth

College Dean
Dr. Shankar Mahalingam

12/8/15 Graduate Dean
Dr. David Berkowitz

ABSTRACT
The School of Graduate Studies
The University of Alabama in Huntsville

Degree Master of Science in Engineering Program Mechanical Engineering

Name of Candidate Zhong Ren

Title JET ARRAY IMPINGEMENT HEAT TRANSFER: SEPARATE EFFECTS OF TARGET PLATE DISTANCE, REYNOLDS NUMBER, AND HOLE SPACINGS

The present study provides information which can be used to optimize and design impingement array configurations to satisfy high demand of surface heat transfer augmentation levels. These levels are characterized by use of local, line-averaged, and spatially-averaged distributions of the Nusselt number. In present study, to complete the investigation, data is obtained to show the effects of jet-to-target distance and jet hole spacing on cross-flows at constant Reynolds number. Next, considered are the combined and separate effects of hole array spacing, jet-to-target plate distance, and Reynolds number on cross-flows. In addition, the present investigation also shows the effects of large hole spacing. Included are the effects of jet-to-target plate distance, and jet Reynolds number.

Abstract Approval: Committee Chair _____
Dr. Phillip Ligrani

Department Chair _____
Dr. Keith Hollingsworth

Graduate Dean _____
Dr. David Berkowitz

ACKNOWLEDGEMENTS

Firstly, I would like to express my sincere gratitude to my advisor Prof. Phillip Ligrani for the continuous support of my master thesis and related research, for his patience, motivation, and immense knowledge. His guidance helped me in all the time of research and writing of this thesis. I could not have imagined having a better advisor and mentor for my master thesis.

I thank my fellow labmates in for the days and nights we were working together before deadlines, and for all the fun we have had in the past years. In particular, I am grateful to Dr. Junsik Lee and Mr. Warren Buzzard.

Last but not least, I would like to thank my family: my parents, my grandmother, and my wife for their endless love and supporting.

TABLE OF CONTENTS

LIST OF FIGURES

Figure
Page

LIST OF TABLES

Table
Page

LIST OF SYMBOLS

A_{ht}	heat transfer area on the target plate	[m^2]
D	diameter of an individual impingement hole	[m]
h_{loss}	heat transfer coefficient to account for convection and radiation loss from back side of target plate	[W/m·K]
k	ratio of specific heats	
M_a	impingement air flow Mach number	
Nu	local Nusselt number	
$\overline{Nu}$	line-averaged Nusselt number	
$\overline{\overline{Nu}}$	spatially-averaged Nusselt number	
Q	total power provided to the thermofoil heater	[W]
q_{cb}	convection heat flux from back side of the target plate	[W/ m^2]
q_{cf}	convection heat flux from front side (or impingement side) of the target plate	[W/ m^2]
q_{rb}	radiation heat flux from back side of the target plate	[W/ m^2]
q_{rf}	radiation heat flux from front side (or impingement side) of the target plate	[W/ m^2]
Re_j	impingement air flow Reynolds number	
$T_{ambient}$	ambient static temperature	[K]
T_b	local temperature on the back surface of the polystyrene target plate	[K]

T_j	impingement air static temperature	[K]
T_{oj}	impingement air stagnation temperature	[K]
T_W	local target surface temperature on the surface of the heater adjacent impingement air	[K]
u_a	impingement air velocity	[m/s]
x	streamwise coordinate	[m]
X	streamwise distance between centerlines of adjacent impingement holes	[m]
y	spanwise coordinate	[m]
Y	spanwise distance between centerlines of adjacent impingement holes	[m]
z	normal coordinate	[m]
Z	distance between target plate and impingement hole plate	[m]

Greek symbols

α	air thermal conductivity	[W/m^2 ·K]
ε_f	emissivity of the front surface of the target plate	
$\varepsilon_{\inf}$	emissivity of a plate located opposite to the target plate	
μ	absolute viscosity	[kg/m·s]
ρ_a	impingement air static density	[kg/ m^3]
σ	Boltzman constant	

CHAPTER 1

INTRODUCTION

1.1. Overview

Impingement cooling is often utilized for surface cooling for a variety of applications where management of locally augmented heat loading is required. The present impingement cooling investigation is applicable for cooling of leading edge regions of turbine blades and vanes, as well as for combustion chamber liners, transition pieces, and splash plates.

The purpose of the present research is to provide new heat transfer data for impingement jet array. Data which illustrated the separate and combined effects of jet-to-target plate distance, hole array spacing, Reynolds number, and cross flow effects are presented. Considered is low-speed impingement cooling with spent air constrained to flow out only one side of the flow passage. The present investigation is important because high-accuracy, spatially-resolved, local Nusselt number distributions are included, along with line-averaged and spatially-averaged Nusselt number results. Many researchers have investigated the performance of impingement jet array heat transfer.

1.2. Literature Survey

Related literature survey information is presented in Chapters 2, 3, and 4. Table 1 gives sample literature survey information.

Table 1 Sample literature survey

	Re	Z/D	X/D	Y/D	Hole array patterns

Kercher & Tabakoff	300~30,000	1.0~4.8	3.1~12.5	3.1~12.5	In-line
Chance	6,000~50,000	2,3,4,6,8			Square, equilateral triangle, rectangular
Metzger et al.	5,000~20,000	1,2,3	6~32	6~32	In-line, staggered
Florschuetz et al.	2,500~70,000	1~3	5~15	4~8	In-line, staggered
Obot & Trabold	1,000~21,000	2~16	5~10	4~8	
Bailey & Bunker	14,000~65,000	1.25~5.5	3,6,9	3,6,9	In-line rectangular
San et al.	5,000~15,000	1~4	4~8	4~8	
Vadiraj & Prabhu	3,000~100,000	1~3	5	2~6	In-line rectangular
Present study	**8,000~52,000**	**1.5~8.0**	**5,8,12**	**5,8,12**	**Staggered**

1.3. Objectives of the Experiment

Data are presented which illustrate surface heat transfer characteristics of an array of impingement jets on a flat plate for an impingement passage which confined on three sides. The present research is unique because the investigated values of Reynolds numbers, hole spacing, and jet-to-target plate distance are not considered in any other existing study. Considered are the combined influences of these parameters. Of particular interest are impingement passage cross flow effects. New impingement heat transfer data to illustrate the effects of large hole spacing at different Reynolds numbers and hole spacing are also included. The objectives of the present study are as follows.

(1) Understand the effects of impingement cross-flows on local, line-averaged, and spatially-averaged Nusselt numbers, as both jet-to-target distance and jet hole spacing are altered.

(2) Obtain new impingement heat transfer data which illustrate the combined and separate effects of hole array spacing, jet-to-target plate distance, and Reynolds number on cross-flows for an impingement jet array.

(3) Investigate the effects of large hole spacing. Included are the effects of jet-to-target plate distance, and jet Reynolds number.

1.4. Organization of the thesis

Chapter 2 describes cross-flow effects on impingement array heat transfer with varying jet-to-target plate distance and hole spacing. In this chapter, new impingement heat transfer data are presented for experimental conditions and configurations employed have not been previously examined, which illustrate the effects of impingement cross-flows on local, line-averaged, and spatially-averaged Nusselt numbers, as both jet-to-target distance and jet hole spacing are altered. My contributions related to material in Chapter 2 are: experimental planning, assemble experimental facilities and instrumentation, calibration of different instrumentation devices, conduct experiments to obtain experimental data, acquire data, data analysis, and assemble related reports. Chapter 3 presents additional new crossflow information from jet array impingement cooling: hole spacing, target plate distance, Reynolds number effects. This study provides experimental data for impingement configurations and flow conditions which have not been previously investigated. Of particular importance are new impingement heat transfer data which illustrate the combined and separate effects of hole array spacing, jet-to-target plate distance, and Reynolds number on cross-flows for an impingement jet array. Included is conduction analysis of the impingement cooling array target surface. My contributions related to material in Chapter 3 are: experimental

planning, assemble experimental facilities and instrumentation, calibration of different instrumentation devices, conduct experiments to obtain experimental data, acquire data, data analysis, and assemble related reports. Chapter 4 presents impingement array heat transfer with large hole spacing. Data are presented which illustrate surface heat transfer characteristics of an array of impinging jets on a flat plate. Included are the effects of jet-to-target plate distance, and jet Reynolds number. My contributions related to material in Chapter 4 are: experimental planning, assemble experimental facilities and instrumentation, calibration of different instrumentation devices, conduct experiments to obtain experimental data, acquire data, data analysis, and assemble related reports. Chapter 5 presents a summary and conclusion of the thesis. Within the Appendices, an uncertainty analysis, a data file directory, and a software directory are present.

CHAPTER 2

CROSS-FLOW EFFECTS ON IMPINGEMENT ARRAY HEAT TRANSFER WITH VARYING JET-TO-TARGET PLATE DISTANCE AND HOLE SPACING

This chapter is a reprint of a paper published International Journal of Heat and Mass Transfer, 2014. Authors are J. Lee, Z. Ren, P. M. Ligrani, D. H. Lee, M. D. Fox, and H.-K. Moon.

International Journal of Heat and Mass Transfer 75 (2014) 534–544

Contents lists available at ScienceDirect

International Journal of Heat and Mass Transfer

journal homepage: www.elsevier.com/locate/ijhmt

Cross-flow effects on impingement array heat transfer with varying jet-to-target plate distance and hole spacing

Junsik Lee [a], Zhong Ren [a], Phil Ligrani [b,*], Dae Hee Lee [c], Michael D. Fox [d], Hee-Koo Moon [d]

[a] Parks College of Engineering, Aviation, and Technology, Saint Louis University, 3450 Lindell Boulevard, St. Louis, MO 63103, USA
[b] Oliver L. Parks Endowed Chair, Parks College of Engineering, Aviation, and Technology, Saint Louis University, 3450 Lindell Boulevard, St. Louis, MO 63103, USA
[c] Department of Mechanical and Automotive Engineering, High Safety Vehicle Core Technology Research Center, Inje University, 197 Inje-ro, Gimhae, Gyeongnam 621-749, Republic of Korea
[d] Aero/Thermal & Heat Transfer, Solar Turbines, Inc. 2200 Pacific Highway, P.O. Box 85376, Mail Zone C-9, San Diego, CA 92186-5376, USA

ARTICLE INFO

Article history:
Received 26 December 2013
Received in revised form 14 March 2014
Accepted 14 March 2014
Available online 6 May 2014

Keywords:
Impinging jet
Impingement jet array cooling
Jet-to-target plate distance
Jet hole spacing
Nusselt number

ABSTRACT

New impingement heat transfer data are presented for experimental conditions and configurations employed have not been previously examined, which illustrate the effects of impingement cross-flows on local, line-averaged, and spatially-averaged Nusselt numbers, as both jet-to-target distance and jet hole spacing are altered. Data are given for a constant impingement jet Reynolds number of 8000. In general, the impingement passage cross-flows which accumulate are detrimental to local Nusselt number performance, especially for denser hole arrays with 5*D* and 8*D* hole spacing, where *D* is impingement hole diameter. This is illustrated by periodic variations of surface Nusselt numbers, which generally decrease with streamwise development, and by local Nusselt number *peak values* for hole spacings of 5*D*, 8*D*, and 12*D* which generally become smaller at successive *x/D* locations for each value of *Z/D*. Also considered are unique situations where significant accumulation of cross-flow fluid results in an opposite trend, with local Nusselt numbers which increase with streamwise development for dense hole spacing of 5*D*, and smaller jet-to-target plate distances of 1.5*D* and 3.0*D*.

1. Introduction

Impingement cooling is often utilized for surface cooling for a variety of applications where management of locally augmented heat loading is required. These applications include the leading edge regions of turbine blades and vanes, and parts of the combustor in gas turbine engines, including combustion chamber liners, transition pieces, and splash plates. For both situations, impingement cooling jets are used individually or in arrays. When employed within an airfoil leading edge region, the impingement air generally enters the leading edge cavity from an adjacent cavity through a series of crossover holes on the partition wall between the two cavities. The crossover jets then impinge on the concave leading-edge wall and subsequently exit either through film cooling holes, or though exit passages which lead to another part of the airfoil.

The present investigation considers the combined influences of the spacing between holes within the impingement array, and jet-to-target-plate spacing. The investigated values of hole spacing, and jet-to-target plate distance are not considered in any other existing study. Several other investigations consider similar parameter variations, but over different ranges of experimental and configuration conditions, in flows with low Mach numbers, and relatively low speeds. Of these studies, Kercher and Tabakoff [1] present spatially-averaged surface heat transfer coefficients beneath an array of impinging jets for *X/D* and *Y/D* from 3.1 to 12.5, *Z/D* from 1.0 to 4.8, and Reynolds numbers from 3×10^2 to 3×10^4. An in-line array of holes is employed, and spent air flow from the impingement array exits the flow passage in one direction. According to these investigators, the spatially-averaged heat transfer coefficients are influenced mostly by Reynolds number, and streamwise/spanwise hole spacing. Another related investigation, described by Chupp et al. [2], considers heat transfer on a semi-circular concave surface, with a line of circular jets impinging on the apex. The effects of target spacing, hole spacing, and Reynolds number are considered. Metzger and Korstad [3] consider target spacing and examine the influences of cross-flow on a single line of jets, emerging from circular holes, placed on one wall of a channel. They show that target spacing, jet Reynolds number, and the relative strengths of the jet flow and the cross flow are the most important factors which influence target surface heat

* Corresponding author. Tel.: +1 (314)977 8355; fax: +1 (314)977 8388.
E-mail address: pligrani@slu.edu (P. Ligrani).

http://dx.doi.org/10.1016/j.ijheatmasstransfer.2014.03.040
0017-9310/

Nomenclature

A	impingement hole area (m^2)
A_{ht}	heat transfer area on the target plate (m^2)
C_D	discharge coefficient
D	diameter of an individual impingement hole (m)
k	ratio of specific heats
M_a	impingement air flow Mach number
M_i	impingement air flow ideal Mach number
Nu	local Nusselt number
$\overline{Nu}$	line-averaged Nusselt number
$\overline{\overline{Nu}}$	spatially-averaged Nusselt number
P_a	impingement air static pressure (Pa)
P_{oj}	impingement air stagnation pressure (Pa)
Q	total power provided to the thermofoil heater (W)
q_{cb}	convection heat flux from back side of the target plate (W/m^2)
q_{cf}	convection heat flux from front side (or impingement side) of the target plate (W/m^2)
q_{rb}	radiation heat flux from back side of the target plate (W/m^2)
q_{rf}	radiation heat flux from front side (or impingement side) of the target plate (W/m^2)
R	ideal gas constant
Re_j	impingement air flow Reynolds number
Ti	impingement air ideal static temperature (K)
T_j	impingement air static temperature (K)
T_{oj}	impingement air stagnation temperature (K)
T_W	local target surface temperature on the surface of the heater adjacent impingement air (K)
u_a	impingement air velocity (m/s)
u_i	impingement air ideal velocity (m/s)
x	streamwise coordinate (m)
X	streamwise distance between centerlines of adjacent impingement holes (m)
y	spanwise coordinate (m)
Y	spanwise distance between centerlines of adjacent impingement holes (m)
z	normal coordinate (m)
Z	distance between target plate and impingement hole plate (m)

Greek symbols

α	air thermal conductivity (W/m^2 K)
μ	absolute viscosity (kg/m s)
ρ_a	impingement air static density (kg/m^3)
ρ_i	impingement air ideal static density (kg/m^3)

transfer rates. Jet-to-target-plate spacing is also considered by Chance [4], who also investigates low-speed impingement cooling with spent air constrained to flow out only one side of the flow passage. He describes static pressure variations within the impingement passage, which become larger as cross-flow velocity increases, which occurs as Z/D decreases. Reynolds numbers range from 6×10^3 to 5×10^4, and square, equilateral triangle, and rectangular jet arrays are employed. Z/D values are 2, 3, 4, 6, and 8, and ratios of impingement to surface absolute temperature are 0.77, 1.27, and 1.54.

Metzger et al. [5] and Florschuetz et al. [6] indicate that in-line jet impingement hole patterns provide better heat transfer than staggered arrangements. Investigated are Z/D values of 1, 2, and 3, X/D and Y/D ranging from 6 to 32, and Reynolds numbers from 5×10^3 to 2×10^4. Within the Florschuetz et al. [6] investigation, Reynolds numbers range from 2.5×10^3 to 7×10^4. Utilized are inline and staggered hole patterns, Z/D from 1 to 3, X/D from 5 to 15, and Y/D from 4 to 8. As for the investigation of Metzger and Korstad [3], impinging air is again constrained to exit in a single direction from the channel formed between the impingement plate and the target plate. Florschuetz et al. [6] include data on channel cross flow mass velocity and jet mass velocity (where ratios range from 0 to 0.8), and a correlation which gives Nusselt number dependence upon these parameters, as well as on impingement jet plate geometry, Prandtl number, and Reynolds number.

Jet-to-target plate distance and jet hole spacing influences are also addressed in low speed impingement flows by Obot and Trabold [7], who consider different cross-flow schemes on impingement heat transfer. Impingement jet Reynolds numbers from 1×10^3 to 2.1×10^4, Z/D values from 2 to 16, X/D values of 5 and 10, and Y/D values of 4 and 8 are employed. According to these investigators, for a given cross-flow scheme and constant jet diameter D, higher heat transfer coefficients are obtained as the number of jets over a fixed target area increases. Bailey and Bunker [8] consider axial and lateral jet spacings of 3, 6, and 9, and jet plate-to-target spacings from 1.25 to 5.5 impingement hole diameters. Impingement arrays with inline jets in a "square array" are investigated at Reynolds numbers from 1.4×10^4 to 6.5×10^4 at relatively low Mach numbers. The investigators show that each jet behaves independently for sparse impingement arrays. Also included are correlations which extend the range of applicability of the correlations presented by Florschuetz et al. [6].

Another recent investigation is described by San et al. [9], who present correlation equations which show that stagnation Nusselt numbers are proportional to the 0.7 power of Reynolds number, and the -0.49 power of the ratio of jet plate width to jet diameter. Investigated are ratios of jet target distance to jet diameter from 1 to 4, lateral and streamwise jet spacing ratios from 4 to 8, ratios of jet plate width to jet diameter ratio from 6.25 to 18.75, and Reynolds numbers from 5×10^3 to 1.5 x10^4. Miao et al. [10] consider fluid flow and heat transfer characteristics of round jet arrays impinging orthogonally onto a flat-plate with confined walls and different cross-flow arrangements. Computational fluid dynamics results are obtained for in-line and staggered hole arrays, and parallel, hybrid, and counter cross-flow configurations. Jet Reynolds numbers range from 2.44×10^3 to 1.46×10^4, and Z/D values of 1, 3, and 6 are utilized. According to these investigators, the thermal performance of multiple jet impingement is enhanced when Z/D decreases from 6 to 3, which is illustrated by correlation equations for area-averaged Nusselt number as dependent upon jet Reynolds number. Vadiraj and Prabhu [11] consider the influences of spanwise pitch jet spacing on local transfer distributions for in-line rectangular arrays of jets. Impingement jet Reynolds numbers range from 3×10^3 to 1×10^5, jet-to-target plate spacing ranges from 1 to 3 hole diameters, the X/D value is 5, and Y/D values vary from 2 to 6. Brevet et al. [12] consider optimization of heat transfer from a row of impinging jets.

The present study is aimed at providing new impingement heat transfer data on the combined effects of jet-to-target plate distance and jet hole spacing, at a constant impingement jet Reynolds number of 8000 and jet Mach numbers of approximately 0.10 to 0.14. Of particular importance are the effects of impingement cross-flows, especially their detrimental influences in reducing local surface Nusselt numbers as the impingement jets are deflected and become less coherent. Included are discharge coefficients, as well as local, line-averaged and spatially-averaged surface Nusselt

numbers. The present results are unique because the experimental conditions and configurations employed have not been previously examined. In particular, jet-to-target plate distances Z of 1.5D, 3.0D, 5.0D, and 8.0D are employed, where D is the impingement hole diameter, with non-dimensional streamwise and spanwise hole spacings, X/D and Y/D, of 5.0, 8.0, and 12.0. The thickness of each impingement plate is 1.0D. Each hole array investigated is arranged with a staggered arrangement from each streamwise row to the next. The data obtained are important because they illustrate the important effects of impingement cross-flows on local, line-averaged, and spatially-averaged Nusselt numbers, as jet-to-target distance and jet hole spacing are altered. As such, the present data are useful for the design of impingement array configurations for different engineering applications, as well as for the development of numerical models for prediction of surface heat transfer coefficient distributions from impingement array cooling.

2. Experimental apparatus and procedures

2.1. Impingement flow facility, and impingement plate

Schematic diagrams of the laboratory facility used for heat transfer measurements are presented in Figs. 1 and 2. The facility is constructed of 6.1 mm thick ASTM A38 steel plates, and A53 Grade B ARW steel piping. The air stream through the plenums and channel is drawn from the laboratory atmosphere. To achieve the Reynolds number of the present study, a New York Blower Co. 7.5 HP, size 1808 pressure blower is employed. The air mass flow rate provided to the test section is measured using an ASME standard orifice plate, flow-mounted calibrated copper-constantan thermocouples, and Validyne DP15–22 and DP15–32 pressure transducers (with diaphragms rated at 1.40 and 14.0 kPa, respectively) connected to Validyne Model CD15 Carrier Demodulators. Each of these thermocouples measures recovery temperature, which is used with local velocity magnitude to determine gas static temperature. The blower exits into a series of two plenums arranged in series, where the upstream plenum is 0.63 m in length along each side, and the downstream plenum dimensions are 0.63 m long, 0.77 m tall, and 0.77 m wide. A Bonneville cross-flow heat exchanger is located within each plenum. As the air exits the heat exchanger, and the second plenum, the air passes into a 0.22 m outer diameter pipe, which contains the ASME Standard orifice plate employed to measure the air mass flow rate. This pipe then connects to the 0.635 m by 0.635 m side of a third plenum.

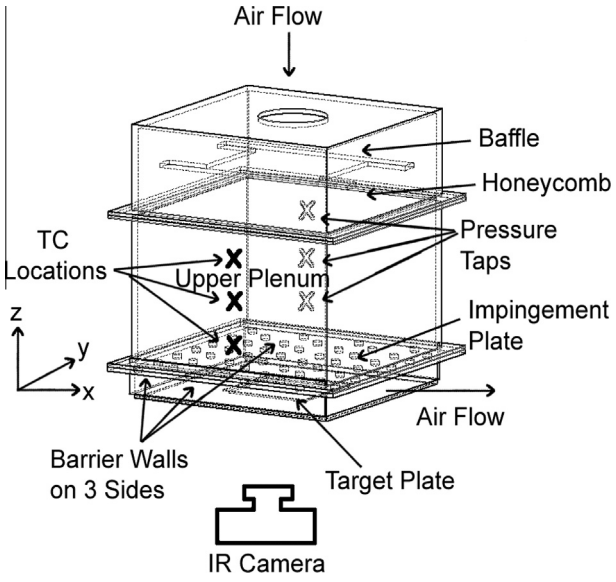

Fig. 2. Impingement flow facility test section, including impingement plenum, and impingement channel.

Upon entering this plenum, the air first encounters the honeycomb, followed by other flow straightening devices. These are followed by the upper plenum, located below the honeycomb and flow straightening devices (as shown in Fig. 2), with top dimensions of 0.635 m and 0.635 m, and height of 0.40 m.

Individual plates with holes used to produce the impingement jets are located at the bottom of this plenum, as shown in Fig. 2. The plenum is thus designed so that different impingement plates can be installed at this location. Fig. 3 shows that each impingement plate consists of 10 rows of holes in the streamwise direction, arranged so that holes in adjacent rows are staggered with respect to each other. With this arrangement, either 9 or 10 holes are located in each streamwise row. The spacing between holes in the streamwise direction X are either 5D, 8D, or 12D, and the spacing between holes in the spanwise direction Y are also either 5D, 8D, or 12D. The thickness of each impingement plate is 1D. The spacing between the hole exit planes and the target plate is denoted Z/D, with values employed in the present investigation of 1.5, 3.0, 5.0, and 8.0. Note that the coordinate systems employed are also shown in Fig. 3. The impingement cooling flow which issues from these holes is contained within the channel formed

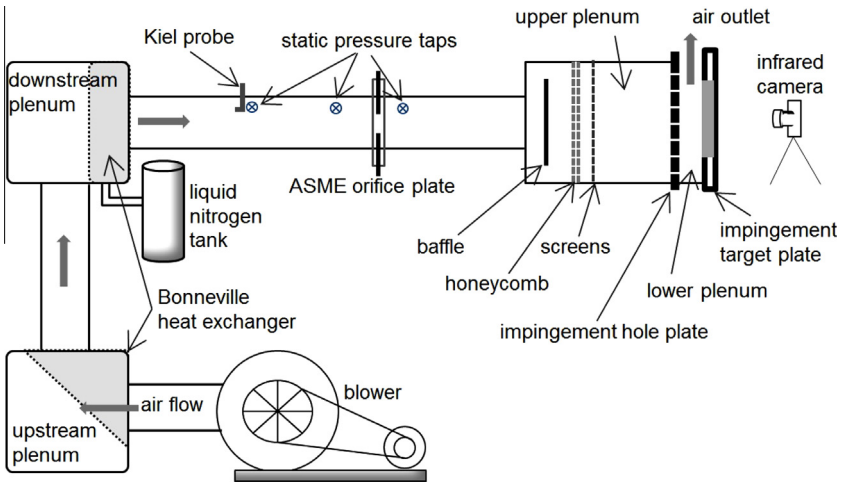

Fig. 1. Impingement flow facility.

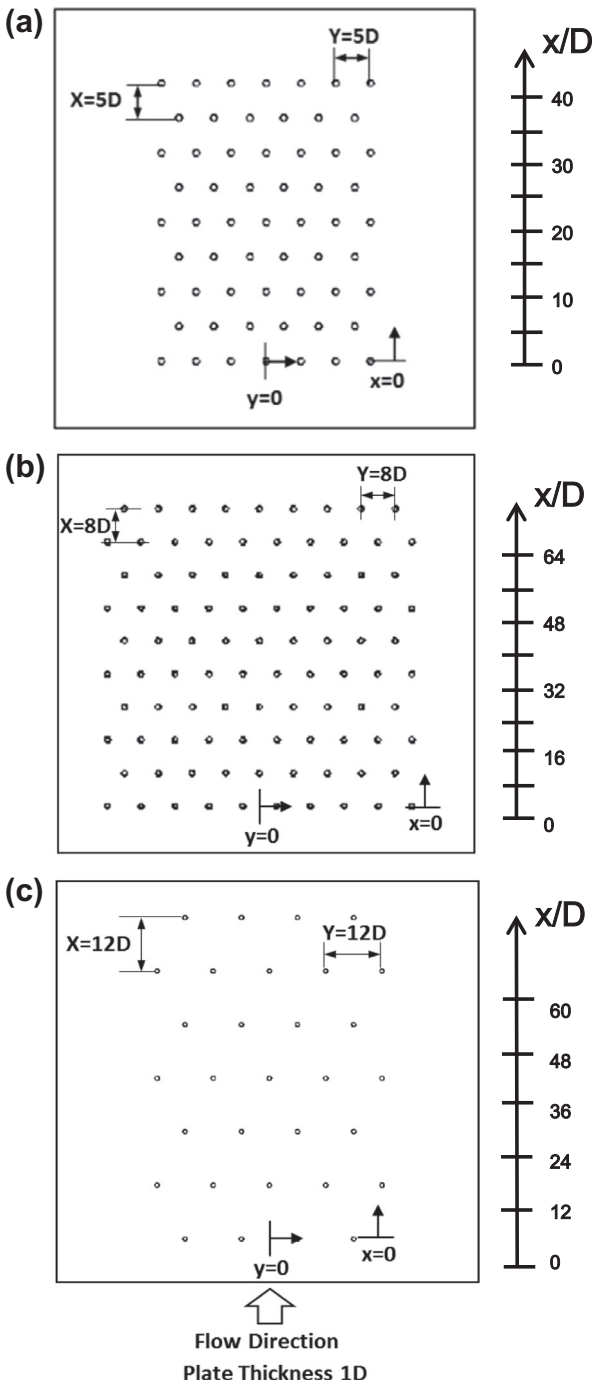

Fig. 3. Impingement test plate configuration: (a) $X/D = Y/D = 5$, (b) $X/D = Y/D = 8$, (c) $X/D = Y/D = 12$.

by the impingement jet plate and the target surface, and is constrained to exit in a single direction, which here, is denoted as the x-direction. This channel is called the lower plenum or impingement plenum. The impingement plenum channel is made up of a volume of air between the target and impingement jet plate, with $4D$ spanwise margins on each side. In the present study, the hole diameter size, D, blower, mass flow rate, and pressure level are employed so that the Mach numbers of approximately 0.1–0.14 and the Reynolds numbers is approximately 8000. This range of Mach numbers are selected because previous investigations show that local and spatially-averaged Nusselt numbers show no dependence on Mach number, when values are less than approximately 0.25.

Additional discussion of related apparatus and procedures is provided by Lee et al. [23].

2.2. Target plate test surfaces for measurements of surface Nusselt numbers

Local surface Nusselt number are measured on a heated polystyrene target plate, with a size of 126 mm by 254 mm by 1.31 mm. The target plate is mounted on the bottom surface of the impingement plenum. A mounting frame is also employed to hold the solid polystyrene target plate in place, and to keep it smooth (without bending or wrinkles), and normal to the impingement jets, as testing is underway. Eight type-T copper-constantan thermocouples are placed at different streamwise and spanwise locations within the polystyrene target plate. These provide measurements of local surface temperatures, after correction for thermal contact resistance and temperature drop through the 0.016 cm thickness of polystyrene. Spatially-resolved distributions of surface heat transfer coefficients and Nusselt numbers are measured on the polystyrene target plates with heaters and thermocouples attached. This heater is located adjacent to the air stream with the impinging air jets to provide a constant surface heat flux boundary condition adjacent to the impingement air stream. The back side of this polystyrene plate is viewed by the infrared camera as spatially-resolved measurements of surface temperature are obtained. Each polystyrene target plate is 1.31 mm thick and each heater is approximately 0.29 mm thick, giving a total target plate thickness of 1.60 mm. Additional related apparatus and procedure details are described by Lee et al. [23].

2.3. Local impingement air pressure and temperature measurements

As shown in Fig. 2, three wall static pressure taps are located on the surface of the upper plenum. Two wall pressure taps are also located on the surface of the lower plenum for measurement of local static pressures. As tests are conducted, calibrated Validyne Model DP15–22 and DP15–32 pressure transducers driven by Validyne Model CD15 Carrier Demodulators are used to sense pressures from these static pressure taps. Local airflow recovery temperatures are measured using two Omega T-type copper-constantan thermocouples located in the central part of the lower plenum, and three copper-constantan thermocouples located in the central part of the upper plenum. Voltages from the carrier demodulators and all thermocouples employed in the study are read sequentially using National Instruments NI-USB 6210 and NI-USB 9162 Data Acquisition terminals, respectively. These terminals relay the information to a Dell Precision T3500 computer. The voltage outputs from this unit are acquired by the computer through its USB port, using LABVIEW 10.0 software.

A Kiel-type stagnation pressure probe is used to measure the total pressure in the pipe at a position which is located upstream of the orifice plate employed to measure mass flow rate. A wall pressure tap located on the surface of the pipe, and a calibrated copper-constantan thermocouple positioned within the air stream are used to sense static pressure and flow recovery temperature, respectively, at the same streamwise location. Pressures and temperatures measured using the thermocouple, probe, and tap are sensed and processed using the same types of instrumentation mentioned earlier. The velocities deduced from this arrangement are used to provide a cross-check on the velocities deduced from mass flow rates, which are measured using the ASME standard orifice plate. With impingement static temperature Tj, impingement flow Mach number M_a, and other parameters known, the impingement Reynolds number is given by an equation of the form

$$Re_j = \rho_a u_a D/\mu \quad (1)$$

2.4. Local Nusselt number measurement

A detailed summary of surface Nusselt number measurement procedures is provided by Lee et al. [23]. The power to the thermofoil heater, mounted on the target plate, is controlled and regulated using an alternating current to direct current Price-Putzebeck POW-R-PAC 160 V transformer power supply. Energy balances, and analysis to determine temperature values on the two surfaces of the target plate, then allow determination of the magnitude of the total convective power (due to impingement cooling) for a particular test. To determine the surface heat flux (used to calculate heat transfer coefficients and local Nusselt numbers), the total convective power level, provided by the particular thermofoil heater employed, is divided by the single surface area of this heater.

One step in this procedure utilizes a one-dimensional conduction analysis, which is applied between the surface *within* the target plate where the thermocouples are located (between the heater and the polystyrene target plate), and the ambient air environment behind the target plate. With these temperatures known, the radiation heat flux and the convection heat flux from the back side of the target plate are determined using correlation equations given by Lee et al. [23]. The radiation heat flux on the front (or impingement side) of the target plate is determined using similar procedures [23]. Another part of this procedure uses a one-dimensional conduction analytical model for the heater, which includes source generation of thermal energy, to provide a relation between *TW*, *Ttc*, and *qcf*. This one-dimensional conduction approach is employed since magnitudes of lateral conduction within the target plate are very small and mostly insignificant (from three-dimensional analyses), relative to impingement convective heat flux levels [23].

The convection heat flux from the front side (or impingement side) of the target plate is then given by

$$q_{cf} = Q/A_{ht} - q_{rf} - q_{rb} - q_{cb} \tag{2}$$

The local Nusselt number is then given as

$$Nu = q_{cf}D/((T_W - T_{oj})\alpha) \tag{3}$$

As impingement heat transfer measurements are made, spatially-resolved distributions of the target test surface temperature T_W are determined using infrared imaging in conjunction with thermocouples, energy balances, digital image processing, and *in situ* calibration procedures. These are then used to determine spatially-resolved surface Nusselt numbers. To accomplish this, the infrared radiation emitted by the heated interior surface of the channel is captured using a ImagIR InSB Digital 320 × 256 infrared camera, which operates at infrared wavelengths from 5.2 μm to 9.1 μm. Temperatures, measured using the calibrated, copper-constantan thermocouples distributed along the test surface adjacent to the flow, are used to perform the *in situ* calibrations simultaneously as the radiation contours from surface temperature variations are recorded [23].

This is accomplished as the camera views the test surface from behind, as shown in Fig. 2. In general, all eight thermocouple junction locations are present in the infrared field viewed by the camera. The exact spatial locations and pixel locations of these thermocouple junctions and the coordinates of the field of view are known from calibration maps obtained prior to measurements. During this procedure, the camera is focused, and rigidly mounted and oriented relative to the test surface in the same way as when radiation contours are recorded. Voltages from the thermocouples are acquired using the apparatus mentioned earlier. With these data, gray scale values at pixel locations within digital images from the infrared imaging camera are readily converted to local Nusselt number values. Because such calibration data depend strongly on camera adjustment, the same brightness, contrast, and aperture camera settings are used to obtain the experimental data. The *in situ* calibration approach rigorously and accurately accounts for these variations [23].

Images from the infrared camera are recorded as 8-bit gray scale directly into the memory of a Dell Precision T3500 computer using a Matrox Frame grabber video card and the infrared camera interface program, WINIR. One set of 50 frames is taken in ten frames sets at five random intervals. All of the resulting images are then ensemble averaged to obtain the final gray scale data image. This final data set is then imported into MATLAB software to convert each of 256 possible gray scale values to local Nusselt number at each pixel location using calibration data. Each individual image covers a 256 pixel by 320 pixel area [23].

2.5. Discharge coefficients

Discharge coefficients are determined using

$$C_D = \rho_a u_a / \rho_i u_i \tag{4}$$

The first step in determining the ideal impingement mass flux $\rho_i u_i$ is obtaining an ideal impingement Mach number M_i using

$$P_{oj}/P_a = [1 + M_i^2(k-1)/2]^{k/k-1} \tag{5}$$

Next, impingement ideal static temperature T_i is determined using T_{oj}, the ideal Mach number M_i, and the appropriate ideal gas isentropic relationship. Impingement ideal static density is given by $\rho_i = P_a/RT_i$, and impingement ideal velocity is given by $u_i = M_i(kRT_i)^{1/2}$. Note that, in most cases, discharge coefficients are determined which are based on P_a, the spatially-averaged static pressure at the exits of the impingement holes.

2.6. Experimental uncertainty estimates

Uncertainty estimates are based on 95% confidence levels and are determined using methods described by Kline and McClintock [13] and Moffat [14]. Uncertainty of temperatures measured with thermocouples is ±0.15 °C. Spatial and temperature resolutions achieved with infrared imaging are about 0.1 mm to 0.2 mm, and 0.4 °C, respectively. This magnitude of temperature resolution is due to uncertainty in determining the exact locations of thermocouples with respect to pixel values used for the *in situ* calibrations. Of the different quantities considered, the uncertainty associated with surface temperature makes the largest contribution to overall Nusselt number uncertainty. Note that the overall Nusselt number uncertainty also includes possible contributions from lateral conduction within the test plates, although, in general, magnitudes of lateral conduction (in the *x* and *y* directions) are generally insignificant relative to overall convective heat flux levels from impingement. Table 1 shows that the total local Nusselt number uncertainty is approximately ±6.0%. This uncertainty magnitude represents the maximum value which is encountered for all test conditions within the present investigation. As such, the influences of all relevant quantities to Nusselt number uncertainty are

Table 1
Experimental uncertainty magnitudes for the local Nusselt number, and quantities employed to determine the local Nusselt number.

Quantity	Experimental uncertainty (%)
A_{ht}	1.394
D	4.919
T_w	2.706
T_{oj}	0.722
α	0.541
Nu	6.043

considered, including contributions from the uncertainty in measured local surface temperature.

3. Experimental results

The impingement test plate configurations and the experimental test conditions of the present investigation are presented in Table 2.

3.1. Discharge coefficients

Discharge coefficients represent average values for all of the impingement holes on a particular test plate, and are presented in Fig. 4. Here, the discharge coefficients for Z/D of 5 and 12 generally increase slightly as the Z/D value increases. When $Z/D = 1.5$, C_D values are generally lower than other Z/D values (when compared at constant hole spacing), as a result of greater flow confinement, which increases as the jet-to-target plate distance decreases. In addition, C_D values for $Z/D = 1.5$ are higher for 12D hole spacing than for the 5D hole spacing. This is due to increased interactions between adjacent jets, with greater second law losses, for the more dense hole array. Overall, these data illustrate appropriate performance of the cooling supply system for the impingement facility, without the presence of leaks or obstructions producing unnecessary pressure decreases.

3.2. Spatially-resolved local Nusselt numbers

Spatially-resolved surface Nusselt number distributions are presented in Figs. 5–7 for the three different jet hole spacings of 5D, 8D, and 12D, respectively. These data are provided for a constant impingement jet Reynolds number Re_j of approximately 8000. Associated respective Mach numbers Ma, according to Table 2, are between approximately 0.10 and 0.14. Because these values are less than 0.25, little or no Mach number dependence is expected [15]. The different views of the test surface in Figs. 5–7 are due to different infrared camera views of the target plate, as different impingement plates with different hole spacing are employed.

For each of the three hole spacings, Figs. 5–7 show that the qualitative distributions of local Nusselt numbers produced by each impingement jet are similar, with good periodic repeatability in the spanwise direction for each streamwise row of impact locations. Note that the highest local maximum Nusselt numbers in Figs. 5 and 6 for X/D and Y/D equal to 5 and 8 appear to be associated with $Z/D = 3.0$. In contrast, Fig. 7 for $X/D = Y/D = 12$ shows that the highest local maximum Nusselt numbers appear to be associated with $Z/D = 5.0$. The local Nusselt number for 5D and 8D hole spacing in Figs. 5 and 6 are also higher than for 12D hole spacing in Fig. 7. This is a result of the cumulative effects of the interactions between adjacent jets, and the resulting cross-flows for an arrangement where the jets are more closely spaced together.

Figs. 5–7 also generally show that local Nusselt number *peak values* generally become smaller at successive x/D locations for

Table 2
Impingement test plate configurations and experimental test conditions.

X/D, Y/D	Re_j	Ma	Z/D	Hole diameter (mm)	Plate thickness (mm)	Hole spacings (mm)
5	8000	0.14	1.5	4.5	4.5	22.5
5	8000	0.11	3.0	4.5	4.5	22.5
5	8000	0.10	5.0	4.5	4.5	22.5
5	8000	0.10	8.0	4.5	4.5	22.5
8	8200	0.13	1.5	4.5	4.5	36
8	8200	0.11	3.0	4.5	4.5	36
8	8200	0.10	5.0	4.5	4.5	36
8	8200	0.10	8.0	4.5	4.5	36
12	8000	0.14	1.5	3.5	3.5	42
12	8000	0.13	3.0	3.5	3.5	42
12	8000	0.13	5.0	3.5	3.5	42
12	8000	0.13	8.0	3.5	3.5	42

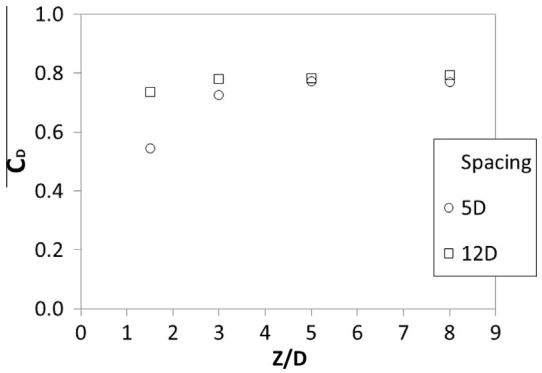

Fig. 4. Discharge coefficient variations with Z/D for hole spacing of 5D and 12D at a constant Re_j of 8000.

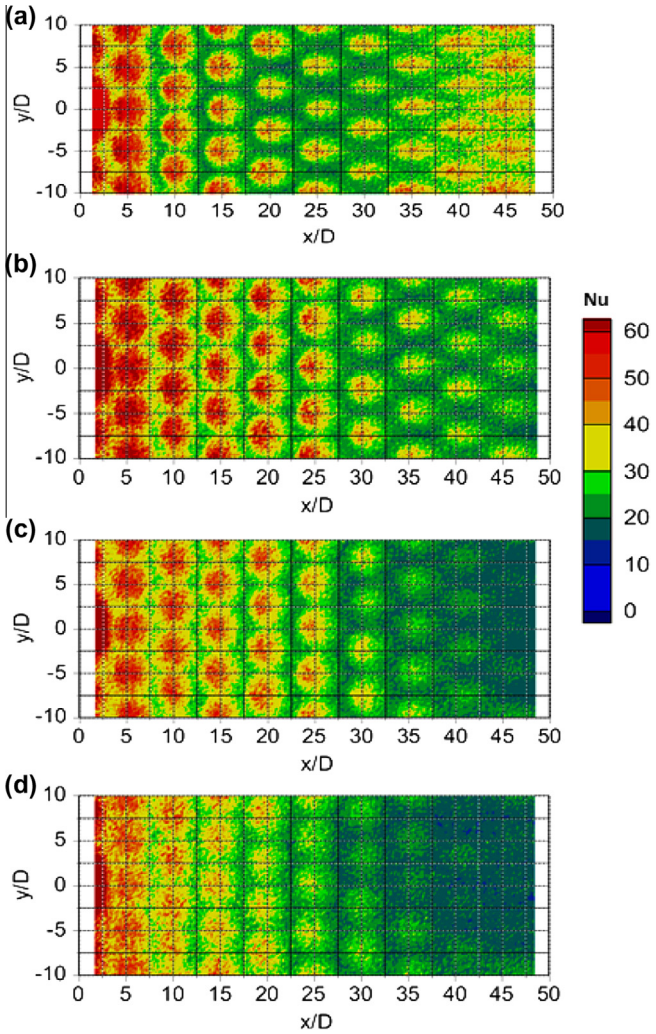

Fig. 5. Local Nusselt number variations for $Re_j \approx 8000$ for different Z/D values and $X/D = Y/D = 5$: (a) $Z/D = 1.5$, (b) $Z/D = 3.0$, (c) $Z/D = 5.0$, (d) $Z/D = 8.0$.

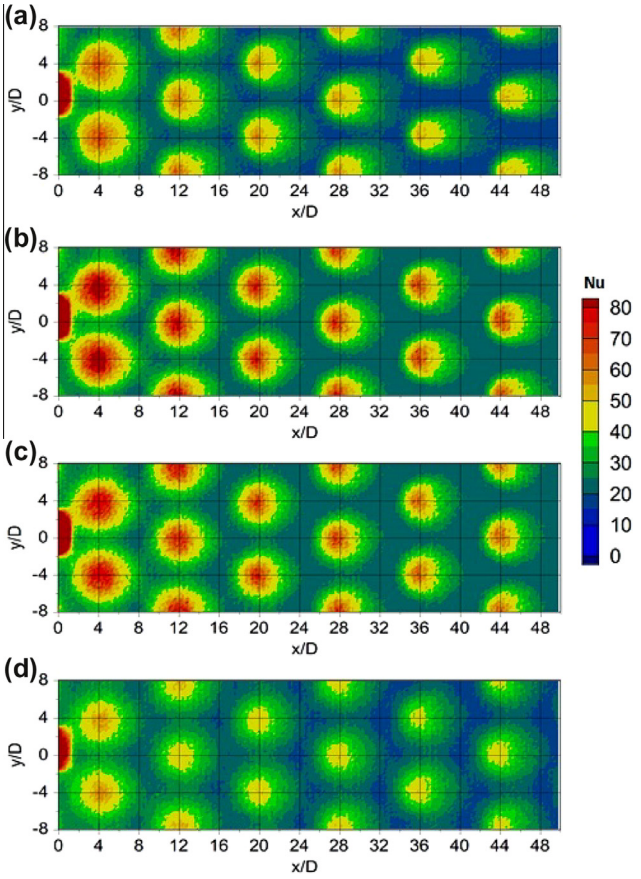

Fig. 6. Local Nusselt number variations for $Re_j \approx 8200$ for different Z/D values and $X/D = Y/D = 8$: (a) $Z/D = 1.5$, (b) $Z/D = 3.0$, (c) $Z/D = 5.0$, (d) $Z/D = 8.0$.

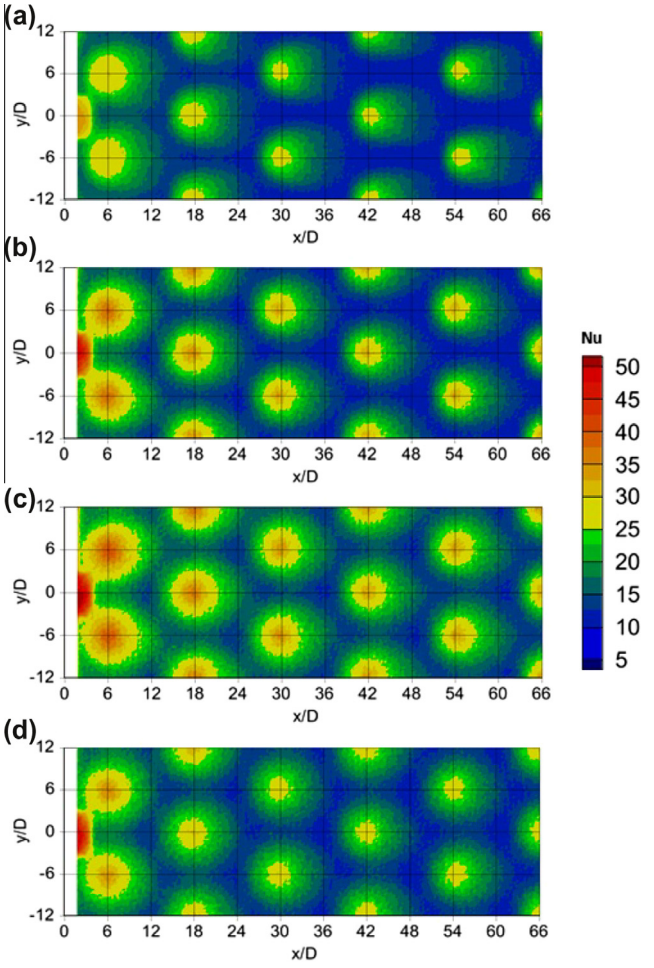

Fig. 7. Local Nusselt number variations for $Re_j \approx 8000$ for different Z/D values and $X/D = Y/D = 12$: (a) $Z/D = 1.5$, (b) $Z/D = 3.0$, (c) $Z/D = 5.0$, (d) $Z/D = 8.0$.

each value of Z/D, due to the detrimental effects of spent air cross-flow on surface heat transfer coefficients. Several exceptions are evident, including the surface Nusselt number distribution for $Z/D = 1.5$ with $5D$ hole spacing, which is presented in Fig. 5a. Such behavior is a consequence of augmented flow mixing and increased local turbulent transport levels. These occur at this experimental condition because the dense hole array and the small jet-to-target plate distance result in increased interactions between adjacent jet fluid concentrations, and between the impingement jet fluid and surrounding cross-flows.

Figs. 8–10 present comparisons of local surface Nusselt number distributions for three different hole spacings $X/D = Y/D$ of $5D$, $8D$, and $12D$, respectively. These results are given for a constant impingement jet Reynolds numbers of approximately 8000, and for normalized jet-to-target plate distances Z/D of 1.5, 3.0, 5.0, and 8.0. Each set of local Nusselt number data are presented as dependent upon y/D for particular values of x/D, and as dependent upon x/D for particular values of y/D. For each of the three hole spacings, local Nusselt numbers at each x/D and y/D location generally decrease continually in a periodically repeating fashion with increasing x/D. The largest decreases with x/D are present with $5D$ hole spacing, whereas the smallest decreases are evident when the hole spacing is $12D$. Such variations are a direct result of the intensity of the cross-flows which develop within the impingement passage. Such cross flows increase as the hole spacing becomes less and the hole spacing arrangements are more dense, and as impingement flow passages are more confined with smaller Z/D values. Additional discussion of cross-flow effects is provided by Yang et al. [24], who also present numerical visualizations of impingement jet trajectories, as well as by Chauhan and Thakur [25], who provide impingement heat transfer and friction factor correlations. Another recent investigation by Gao [26] compares experimental data from in-line impingement arrays to correlations from Kercher and Tabakoff [1] and from Florscheutz et al. [6]. According to this investigator, both correlations "over-estimate the heat transfer coefficient for the first impingement jet row and under-predict the heat transfer coefficient for strong cross-flow situations."

Exceptions are evident for $5D$ hole spacing and Z/D of 1.5 in Fig. 8b, and for $5D$ hole spacing and Z/D of 3.0, also in Fig. 8b. For these situations, increases in local mixing and local turbulent transport levels are more important than the cross-flows, in regard to their influence in altering local Nusselt numbers.

Figs. 8–10 additionally show that the highest local maximum Nusselt numbers are generally associated with Z/D of 3.0 (when $X/D = Y/D = 5$ and $X/D = Y/D = 8$) and with Z/D of 5.0 (when $X/D = Y/D = 12$). Associated local Nusselt number values also generally decrease as Z/D increases, relative to these values, at most all x/D and y/D values. Such variations are especially apparent in Fig. 8 when denser hole spacing is employed. This is due to diminished coherence of the shear layers which form around each jet. The associated Kelvin–Helmholtz generated vortices, which occur as jet advection distances become larger, also play a role in altering local surface Nusselt number distributions [16–22]. According to Lee et al. [23], associated overall and local Nusselt number changes with Z/D (at most all x/D and y/D values) are due to the competing influences of jet/shear layer coherence, and Kelvin–Helmholtz

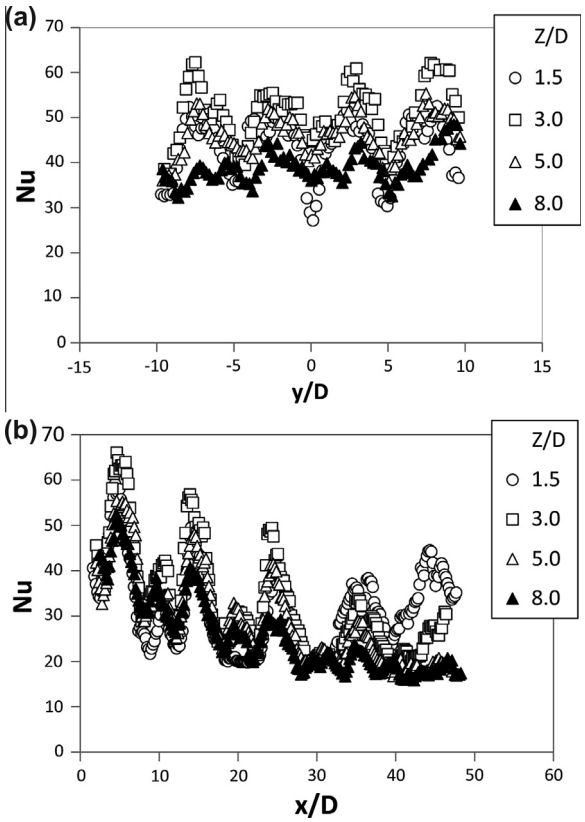

Fig. 8. Local Nusselt number variations for $Re_j \approx 8000$ for different Z/D values and $X/D = Y/D = 5$: (a) variations with y/D for $x/D = 20$, (b) variations with x/D for $y/D = 5$.

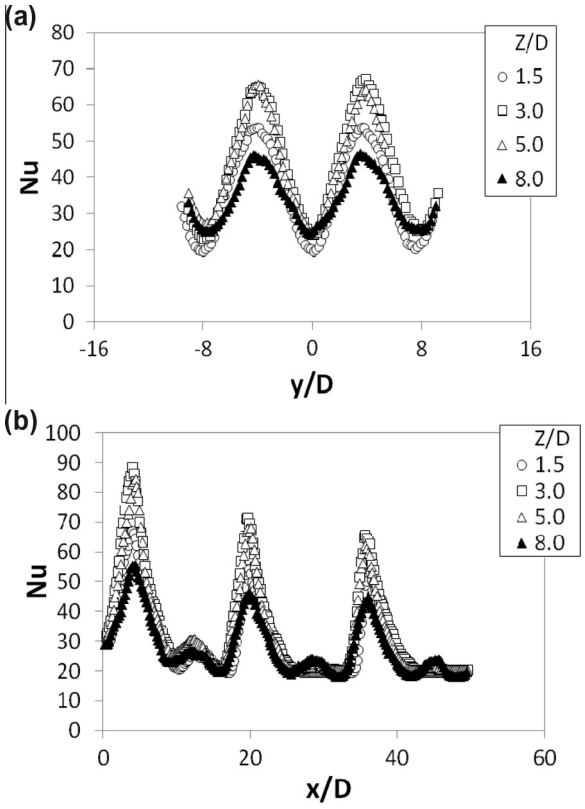

Fig. 9. Local Nusselt number variations for $Re_j \approx 8200$ for different Z/D values and $X/D = Y/D = 8$: (a) variations with y/D for $x/D = 20$, (b) variations with x/D for $y/D = 4$.

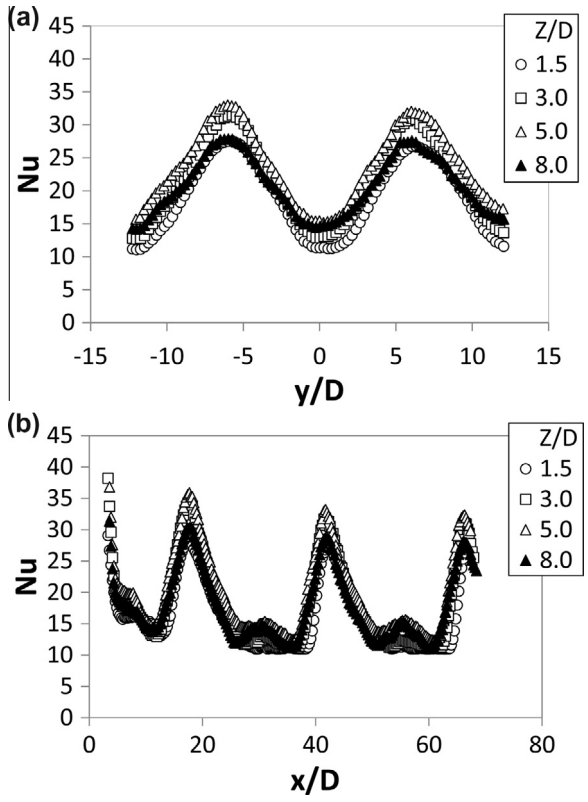

Fig. 10. Local Nusselt number variations for $Re_j \approx 8000$ for different Z/D values and $X/D = Y/D = 12$: (a) variations with y/D for $x/D = 30$, (b) variations with x/D for $y/D = 0$.

generated vortices. In general, the former are believed to be more influential for smaller jet advection distances, whereas the latter are likely more important as jet advection distances become larger.

For the 5D and 8D hole spacing, the influences of surrounding jets, including the cumulative accumulation of cross-flows from sequential rows of jets, reduces the effectiveness of each individual jet by increasing amounts with streamwise development. The accumulated cross-flow causes each impingement jet concentration to deflect and bend in the downstream direction. This distributes the impingement coolant concentrations over larger volumes, which often makes jet coolant concentrations less coherent, as shear stress magnitudes adjacent to impingement jet concentrations are redistributed. As a result, periodic variations of surface Nusselt numbers generally decrease with streamwise development. With larger hole spacing of 12D, cumulative cross-flow mass velocities are smaller, and the influences of surrounding jets are weaker because the behavior of each impingement jet approximates that of a single jet.

Note that x/D and y/D ranges of values, and the numbers of impingement jet events are different in Figs. 8–10, as well as in many figures which follow. This is because the dimensional field of view of the camera is approximately invariant. In addition, impingement holes with different diameters (with associated configuration parameters scaled accordingly) are utilized (as listed in Table 2). As a result, Fig. 8b provides evidence of approximately 5 primary and 4 secondary impingement jet events, whereas Fig. 9b and Fig. 10b provide evidence of approximately 3 primary and 3 secondary impingement jet events.

3.3. Line-averaged Nusselt numbers

Figs. 11–13 present Nusselt numbers which are line-averaged over y/D from −5.0 to +5.0 for a hole spacing of 5D, from −8.0 to

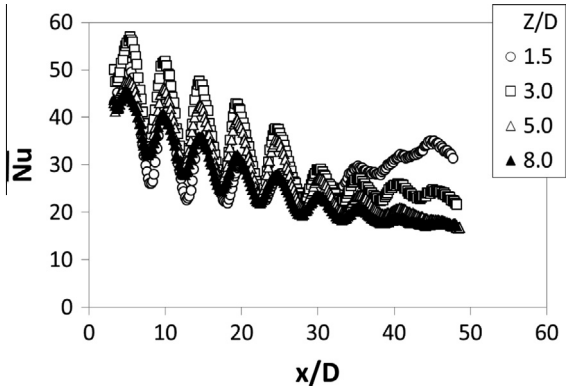

Fig. 11. Line-averaged Nusselt numbers as dependent upon x/D for different Z/D values, $Re_j \approx 8000$, and $X/D = Y/D = 5$.

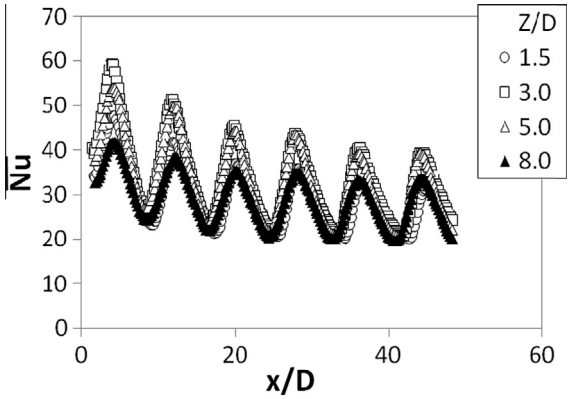

Fig. 12. Line-averaged Nusselt numbers as dependent upon x/D for different Z/D values, $Re_j \approx 8200$, and $X/D = Y/D = 8$.

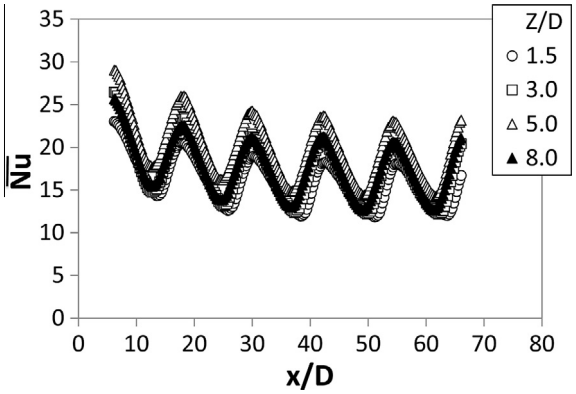

Fig. 13. Line-averaged Nusselt numbers as dependent upon x/D for different Z/D values, $Re_j \approx 8000$, and $X/D = Y/D = 12$.

+8.0 for a hole spacing of 8D, and from −12.0 to +12.0 for a hole spacing of 12D, respectively. Comparisons of the data in the three figures show that line-averaged Nusselt number data generally increase at each x/D as Z/D approaches 3.0 when $X/D = Y/D = 5$, as Z/D approaches 3.0 when $X/D = Y/D = 8$, and as Z/D approaches 5.0 when $X/D = Y/D = 12$. As such, the present results illustrate different Nusselt number dependence upon jet-to-target plate distance, as array hole spacing changes. Consideration of these results at particular values of hole spacing and Z/D shows that periodic line-averaged Nusselt numbers generally decrease at the successive x/D locations, such that successive maximum and minimum values become lower and lower as the impingement flows advect downstream. For 12D hole spacing in Fig. 13, line-averaged Nusselt numbers show somewhat less variation with x/D. This is partially because the large hole spacing causes the behavior of each impingement jet to approximate that of a single jet.

Within Fig. 11, the $X/D = Y/D = 5$ and $Z/D = 1.5$ data set, and the $X/D = Y/D = 5$ and $Z/D = 3.0$ data set show important deviations and different qualitative trends, compared to most other results at different values of X/D, Y/D, and Z/D. Here, line-averaged Nusselt numbers decrease as x/D approaches 30. Line-averaged Nusselt number values then increase somewhat as x/D increases further. This is due to: (a) the cross-flow accumulation of impingement coolant where the flow is confined and restricted, (b) extra mixing caused by coolant interactions, and (c) interactions between accumulated cross-flows and impingement jet fluid from different rows of holes. The overall consequence is increased magnitudes of local shear stress and local turbulent transport within the confined downstream portions of the impingement cooling passage.

3.4. Spatially-averaged Nusselt numbers

Spatially-averaged Nusselt numbers for Z/D values of 1.5, 3.0, 5.0, and 8.0 are presented in Figs. 14–17, respectively, as dependent upon x/D. In each figure, data are presented for jet hole spacings $X/D = Y/D$ of 5, 8, and 12. Each spatially-averaged value is determined over an area which extends over an x/D range from −2.5 to + 2.5 for 5D hole spacing, −4.0 to + 4.0 for 8D hole spacing, and −6.0 to + 6.0 for 12D hole spacing, relative to each streamwise row location. Each value is also averaged over a y/D range comprised of one or two complete periods of local spanwise Nusselt number variation. Here, the spatially-averaged Nusselt numbers for 8D jet hole spacing are generally higher than values for 12D jet hole spacing at each x/D location. The data for 12D jet hole spacing also show less variation with x/D, which is consistent with lower magnitudes of cross-flow.

Figs. 14–17 show that spatially-averaged Nusselt numbers for 8D and 12D hole spacings generally decrease at successive x/D locations when Z/D is either 1.5, 3.0, 5.0, or 8.0. In contrast, Fig. 14 for $Z/D = 1.5$ shows that the 5D hole spacing data initially decrease as x/D increases. As this occurs, spatially-averaged Nusselt number values for 5D and 8D hole spacings are similar in magnitude for $x/D < 20$, regardless of the value of Z/D. However, as x/D exceeds 30, spatially-averaged $X/D = Y/D = 5$ Nusselt numbers in Fig. 14 then increase substantially with streamwise development. This behavior is due to the cross-flow accumulation of impingement coolant within the downstream confined coolant passage,

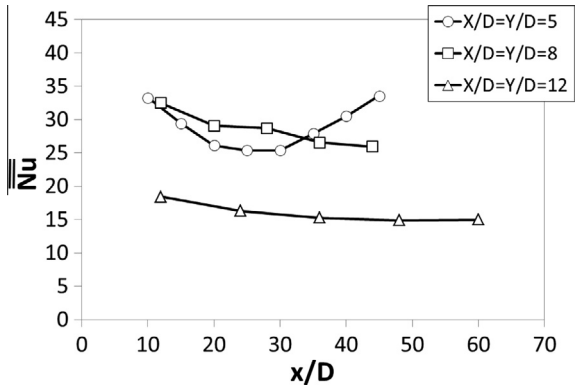

Fig. 14. Spatially-averaged Nusselt numbers as dependent upon x/D for different hole spacings ($X/D = Y/D$) values, $Re_j \approx 8000$, $Z/D = 1.5$.

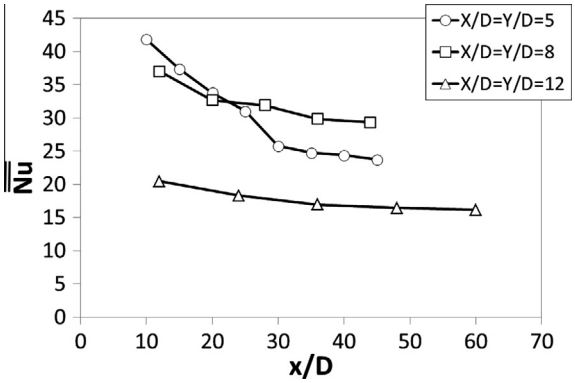

Fig. 15. Spatially-averaged Nusselt numbers as dependent upon x/D for different hole spacings ($X/D = Y/D$) values, $Re_j \approx 8000$, $Z/D = 3.0$.

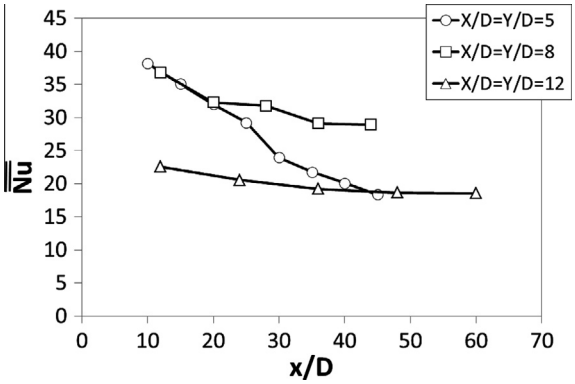

Fig. 16. Spatially-averaged Nusselt numbers as dependent upon x/D for different hole spacings ($X/D = Y/D$) values, $Re_j \approx 8000$, $Z/D = 5.0$.

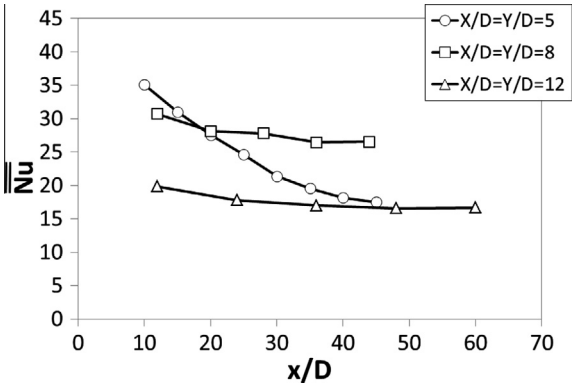

Fig. 17. Spatially-averaged Nusselt numbers as dependent upon x/D for different hole spacings ($X/D = Y/D$) values, $Re_j \approx 8000$, $Z/D = 8.0$.

extra mixing caused by coolant interactions, and interactions between cross-flows and impingement jets from different rows of holes, as mentioned earlier.

When Z/D equals 3.0, 5.0, or 8.0, the data trends for the $X/D = Y/D = 5$ data in Figs. 15–17 are substantially different compared to results for $X/D = Y/D$ equal to 8 and 12. For all three Z/D values, the $X/D = Y/D = 5$ data show more substantial decreases with streamwise development compared to $X/D = Y/D = 8$ and $X/D = Y/D = 12$ data. This larger decrease with streamwise development is due to the detrimental effects of cross flows, which are more substantial for the smaller hole spacing. This cross-flow detriment from smaller hole spacing is present regardless of the value of Z/D, provided $Z/D \geqslant 3.0$.

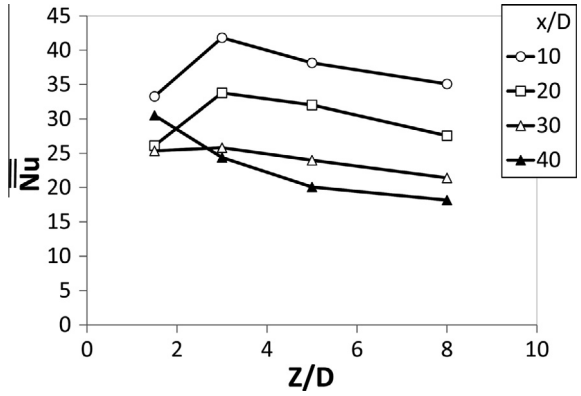

Fig. 18. Spatially-averaged Nusselt numbers as dependent upon Z/D for different x/D values, $Re_j \approx 8000$, and $X/D = Y/D = 5$.

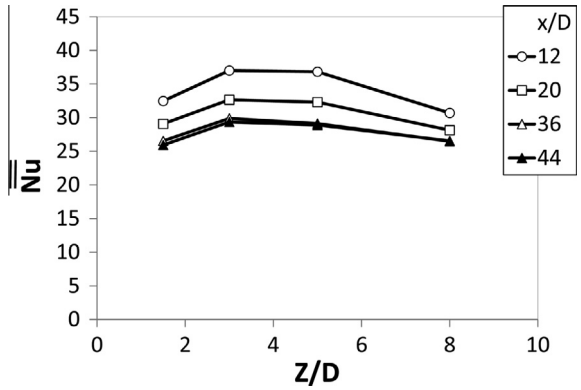

Fig. 19. Spatially-averaged Nusselt numbers as dependent upon Z/D for different x/D values, $Re_j \approx 8000$, and $X/D = Y/D = 8$.

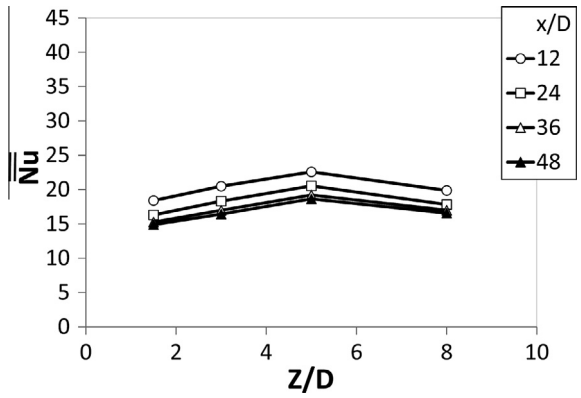

Fig. 20. Spatially-averaged Nusselt numbers as dependent upon Z/D for different x/D values, $Re_j \approx 8000$, and $X/D = Y/D = 12$.

Figs. 18–20 present spatially-averaged Nusselt numbers as dependent upon Z/D for different x/D locations and for each jet hole spacings of 5D, 8D, and 12D, respectively. All of these data are provided for a constant Reynolds number Re_j of approximately 8000. In general, spatially-averaged Nusselt numbers are often higher as jet hole spacing ($X/D = Y/D$) decreases because of greater accumulations of coolant within the impingement flow passage. Figs. 18 and 19 show that the highest spatially-averaged Nusselt numbers for 5D and 8D hole spacings are generally present for $Z/D = 3.0$. Fig. 20 for 12D jet hole spacing shows that spatially-averaged Nusselt numbers are highest for $Z/D = 5.0$.

4. Summary and conclusions

New impingement heat transfer data are presented, which illustrate the effects of impingement cross-flows, especially their detrimental influences in reducing local surface Nusselt numbers as the impingement jets are deflected and become less coherent. A constant impingement jet Reynolds number of 8000 is employed, with jet Mach numbers of approximately 0.10 to 0.14. Jet-to-target plate distances Z of 1.5D, 3.0D, 5.0D, and 8.0D are utilized, where D is the impingement hole diameter, with non-dimensional streamwise and spanwise hole spacings, X/D and Y/D, of 5.0, 8.0, and 12.0. The thickness of each impingement plate is 1.0D. Each hole array investigated is arranged with a staggered arrangement from each streamwise row to the next.

In general, the impingement passage cross-flows which accumulate are detrimental to local Nusselt number performance, especially for denser hole arrays with 5D and 8D hole spacing. The accumulated cross-flow causes each impingement jet concentration to deflect and bend in the downstream direction. This distributes the impingement coolant concentrations over larger volumes, which often makes jet coolant concentrations less coherent, as shear stress magnitudes adjacent to impingement jet concentrations are redistributed. Also important are the interactions of the Kelvin–Helmholtz vortex structures which initially form around the jets and then impact and then advect away from stagnation points along the impingement target surface. Thus, the influences of surrounding jets, including the cumulative accumulation of cross-flows from sequential rows of jets, cause the effectiveness of each individual jet to diminish by greater amounts as these jets are located farther downstream. As a result, periodic variations of surface Nusselt numbers generally decrease with streamwise development, and local Nusselt number *peak values* for hole spacings of 5D, 8D, and 12D generally become smaller at successive x/D locations for each value of Z/D. In particular, for all three Z/D values, the $X/D = Y/D = 5$ data show more substantial decreases with streamwise development compared to $X/D = Y/D = 8$ and $X/D = Y/D = 12$ data. This larger decrease is due to more substantial cross flows for the smaller hole spacing. With larger hole spacing of 12D, cumulative crossflow mass velocities are smaller, and the influences of surrounding jets are weaker because the behavior of each impingement jet approximates that of a single jet.

Of particular importance are unique situations where significant accumulation of cross-flow fluid results in an opposite trend, with augmented local Nusselt numbers with streamwise development. In the present investigation, this occurs for $X/D = Y/D = 5$ and $Z/D = 1.5$, and for $X/D = Y/D = 5$ and $Z/D = 3.0$. For these situations, local, line-averaged and spatially-averaged Nusselt numbers decrease as x/D approaches 30. Nusselt number values then increase as x/D increases further. This is a result of: (i) the cross-flow accumulation of impingement coolant where the flow is confined and restricted, (ii) extra mixing caused by vigorous coolant interactions, and (iii) interactions between accumulated cross-flows and impingement jet fluid from different rows of holes. The overall consequence is increased magnitudes of local shear stress and local turbulent transport within the confined downstream portions of the impingement cooling passage. Such arrangements should be utilized wherever possible to optimize local heat transfer efficiency.

Acknowledgements

The research presented in this paper was sponsored by Solar Turbines Inc., located in San Diego, California.

References

[1] D.M. Kercher, W. Tabakoff, Heat transfer by a square array of round air jets impinging perpendicular to a flat surface including the effect of spent air, ASME Trans., J. Eng. Power 92 (1970) 73–82.
[2] R. Chupp, H. Helms, P. McFadden, T. Brown, Evaluation of internal heat-transfer coefficients for impingement cooled turbine airfoils, AIAA J. Aircraft 6 (3) (1969) 203–208.
[3] D.E. Metzger, R. Korstad, Effects of crossflow on impingement heat transfer, ASME Trans. J. Eng. Power 94 (1972) 35–41.
[4] J.L. Chance, Experimental investigation of air impingement heat transfer under an array of round jets, TAPPI 57 (6) (1974) 108–112.
[5] D.E. Metzger, L.W. Florschuetz, D.I. Takeuchi, R.D. Behee, R.A. Berry, Heat transfer characteristics for inline and staggered arrays of circular jets with crossflow of spent air, ASME Trans. J. Heat Transfer 101 (1979) 526–531.
[6] L.W. Florschuetz, C.R. Truman, D.E. Metzger, Streamwise flow and heat transfer distributions for jet array impingement with crossflow, ASME Trans. J. Heat Transfer 103 (1981) 337–342.
[7] N.T. Obot, T.A. Trabold, Impingement heat transfer within arrays of circular jets: Part 1-Effects of minimum, intermediate, and complete crossflow for small and large spacings, ASME Trans. J. Heat Transfer 109 (1987) 872–879.
[8] J.C. Bailey, R.S. Bunker, Local heat transfer and distributions for impinging jet arrays of dense and sparse extent, ASME Paper No. GT-2002-30473 (2002).
[9] J.Y. San, Y.M. Tsou, Z.C. Chen, Impingement heat transfer of staggered arrays of air jets confined in a channel, Int. J. Heat Mass Transf. 50 (19–20) (2007) 3718–3727.
[10] J.M. Miao, C.Y. Wu, P.H. Chen, Numerical investigation of confined multiple-jet impingement cooling over a flat plat at different crossflow orientations, Numer. Heat Transfer A: Appl.: Int. J. Comput. Methodol. 55 (11) (2009) 1019–1050.
[11] K. Vadiraj, S.V. Prabhu, Influence of spanwise pitch on local heat transfer distribution for in-line arrays of circular jets with spent air flow in two opposite directions, Exp. Thermal Fluid Sci. 33 (2008) 84–95.
[12] P. Brevet, C. Dejeu, E. Dorignac, M. Jolly, J.J. Vullierme, Heat transfer to a row of impinging jets in consideration of optimization, Int. J. Heat Mass Transf. 45 (2002) 4191–4200.
[13] S.J. Kine, F.A. McClintock, Describing uncertainties in single sample experiments, Mech. Eng. 75 (1953) 3–8.
[14] R.J. Moffat, Describing the uncertainties in experimental results, Exp. Thermal Fluid Sci. 1 (1) (1988) 3–17.
[15] J. Park, M. Goodro, P.M. Ligrani, M. Fox, H.K. Moon, Separate effects of Mach number and Reynolds number on jet array impingement heat transfer, ASME Trans. J. Turbomach. 129 (2) (2007) 269–280.
[16] Y.M. Chung, K.H. Luo, Unsteady heat transfer analysis on an impinging jet, ASME Trans. J. Heat Transfer 124 (2002) 1039–1048.
[17] D.H. Lee, H.J. Park, P.M. Ligrani, Visualization and structure of confined, milliscale, unsteady impinging slot jets and associated vortices, Exp. Fluids 54 (2013) 1420–1434.
[18] C.O. Popiel, O. Trass, Visualization of a free and impinging round jet, Exp. Thermal Fluid Sci. 4 (1992) 106–115.
[19] M. Angioletti, R.M. Di Tommaso, E. Nino, G. Ruocco, Simultaneous visualization of flow field and evaluation of local heat transfer by transitional impinging jets, Int. J. Heat Mass Transf. 46 (2003) 1703–1713.
[20] T.S. O'Donovan, D.B. Murray, Jet impingement heat transfer – Part II: A temporal investigation of heat transfer and local fluid velocities, Int. J. Heat Mass Transf. 50 (2007) 3302–3314.
[21] M.D. Fox, M. Kurosaka, L. Hedges, K. Hirano, The influence of vertical structures on the thermal fields of jets, J. Fluid Mech. 255 (1993) 447–472.
[22] M. Goodro, P.M. Ligrani, H.K. Moon, Mach number, Reynolds number, jet spacing variations: full array of impinging jets, AIAA J. Thermophys. Heat Transfer 24 (1) (2010) 133–144.
[23] J. Lee, Z. Ren, J. Haegele, G. Potts, J.S. Jin, P.M. Ligrani, M. Fox, H.-K. Moon, Effects of jet-to-target plate distance and Reynolds number on jet array impingement Heat transfer, ASME Trans. J. Turbomach. (2014), in press.
[24] L. Yang, J. Ren, H. Jiang, P.M. Ligrani, Experimental and numerical investigation of unsteady impingement cooling within a blade leading edge passage, Int. J. Heat Mass Transf. 71 (2014) 57–68.
[25] R. Chauhan, N.S. Thakur, Heat transfer and friction factor correlations for impingement jet solar air heater, Exp. Thermal Fluid Sci. 44 (2013) 760–767.
[26] L. Gao, Effect of jet hole arrays arrangement on impingement heat transfer, M.S. Thesis, Mechanical Engineering Department, Louisiana State University, 2003.

CHAPTER 3

CROSSFLOWS FROM JET ARRAY IMPINGEMENT COOLING: HOLE SPACING, TARGET PLATE DISTANCE, REYNOLDS NUMBER EFFECTS

This chapter is a reprint of a paper published the International Journal of Thermal Sciences, 2015. Authors are J. Lee, Z. Ren, P. M. Ligrani, M. D. Fox, and H.-K. Moon.

International Journal of Thermal Sciences 88 (2015) 7–18

Contents lists available at ScienceDirect

International Journal of Thermal Sciences

journal homepage: www.elsevier.com/locate/ijts

Crossflows from jet array impingement cooling: Hole spacing, target plate distance, Reynolds number effects

Junsik Lee [a], Zhong Ren [b], Phil Ligrani [b, *], Michael D. Fox [c], Hee-Koo Moon [c]

[a] Parks College of Engineering, Aviation, and Technology, Saint Louis University, 3450 Lindell Boulevard, St. Louis, MO 63103, USA
[b] Propulsion Research Center, Department of Mechanical and Aerospace Engineering, College of Engineering, University of Alabama in Huntsville, Technology Boulevard, Olin B. King Technology Hall S236, Huntsville, AL 35899, USA
[c] Aero/Thermal & Heat Transfer, Solar Turbines, Inc., 2200 Pacific Highway, P. O. Box 85376, Mail Zone C-9, San Diego, CA 92186-5376, USA

ARTICLE INFO

Article history:
Received 16 March 2014
Received in revised form
2 September 2014
Accepted 3 September 2014
Available online

Keywords:
Nusselt number
Impingement cooling
Jet hole array
Jet-to-target plate distance
Impingement jet
Heat transfer augmentation

ABSTRACT

Data which illustrate the combined and separate effects of hole array spacing, jet-to-target plate distance, and Reynolds number on *cross-flows*, and the resulting heat transfer, for an impingement jet array are presented. The array of impinging jets are directed to one flat surface of a channel which is bounded on three sides. Considered are Reynolds numbers ranging from 8000 to 50,000, jet-to-target plate distances of 1.5*D*, 3.0*D*, 5.0*D*, and 8.0*D*, and steamwise and spanwise hole spacing of 5*D*, 8*D*, and 12*D*, where *D* is the impingement hole diameter. In general, the cumulative accumulations of cross-flows, from sequential rows of jets, reduce the effectiveness of each individual jet (especially for jets at larger streamwise locations). In other situations, the impingement cross-flow results in locally augmented Nusselt numbers. Such variations most often occur at larger downstream locations, as jet interactions are more vigorous, and local magnitudes of mixing and turbulent transport are augmented. This occurs in channels at lower Reynolds numbers, where impingement jets are confined by smaller hole spacing, and smaller jet-to-target plate distance. The overall result is complex dependence of local, line-averaged, and spatially-averaged Nusselt numbers on hole array spacing, jet-to-target plate distance, and impingement jet Reynolds number.

1. Introduction

The present impingement cooling investigation is applicable for cooling of leading edge regions of turbine blades and vanes, as well as for combustion chamber liners, transition pieces, and splash plates. Considered are the separate and combined effects of jet-to-target plate distance, Reynolds number, and hole spacing within the impingement array.

Of other recent investigations which consider similar effects in flows with low Mach numbers, and relatively low speeds, Kercher and Tabakoff [1] present spatially-averaged surface heat transfer coefficients beneath an array of impinging jets with an in-line arrangement. Spent air flow from the impingement array exits the flow passage in one direction. Reynolds numbers range from 3×10^2 to 3×10^4, with X/D and Y/D from 3.1 to 12.5, and Z/D from 1.0 to 4.8. Results show that Reynolds number, and streamwise/spanwise hole spacing are the most important parameters which affect magnitudes of spatially-averaged heat transfer coefficients. The influences of cross-flow on a single line of jets, emerging from circular holes, placed on one wall of a channel, are considered by Metzger and Korstad [2]. These researchers also consider target spacing, and show that target spacing, jet Reynolds number, and the relative strengths of the jet flow and the crossflow influence heat transfer on the target wall. Jet-to-target-plate distance influences are also investigated by Chance [3]. Considered is low-speed impingement cooling with spent air constrained to flow out only one side of the flow passage. Larger static pressure variations and higher cross-flow velocities are observed as jet-to-target-plate distance decreases. Addressed are Reynolds numbers from 6×10^3 to 5×10^4. Square, equilateral triangle, and rectangular jet arrays are used, with ratios of impingement to surface absolute temperature of 0.77, 1.27, and 1.54.

Metzger et al. [4] indicate that in-line jet impingement hole patterns provide better heat transfer than staggered arrangements for low-speed environments. Investigated are Z/D values of 1, 2, and

* Corresponding author. Tel.: +1 256 824 5173; fax: +1 256 824 7205.
E-mail addresses: pml0006@uah.edu, p_ligrani@msn.com (P. Ligrani).

http://dx.doi.org/10.1016/j.ijthermalsci.2014.09.003
1290-0729/

Nomenclature

A	impingement hole area
A_{ht}	heat transfer area on the target plate
c_a	impingement air flow sonic velocity
D	diameter of an individual impingement hole
k	ratio of specific heats
$\dot{m}$	impingement air mass flow rate
M_a	impingement air flow Mach number
M_i	impingement air flow ideal Mach number
N	number of impingement holes
Nu	local Nusselt number
$\overline{Nu}$	line-averaged Nusselt number
$\overline{\overline{Nu}}$	spatially-averaged Nusselt number
P_a	impingement air static pressure
Q	total power provided to the thermofoil heater
q_{cb}	convection heat flux from back side of the target plate
q_{cf}	convection heat flux from front side (or impingement side) of the target plate
q_{rf}	radiation heat flux from front side (or impingement side) of the target plate
R	ideal gas constant
Re_j	impingement air flow Reynolds number
T_b	local temperature on the back surface of the polystyrene target plate
T_i	impingement air ideal static temperature
T_j	impingement air static temperature
T_{oj}	impingement air stagnation temperature
T_{tc}	local thermocouple temperature between the heater and the polystyrene target plate
T_W	local target surface temperature on the surface of the heater adjacent impingement air
u_a	impingement air velocity
x	streamwise coordinate
y	spanwise coordinate
z	normal coordinate
X	streamwise distance between centerlines of adjacent impingement holes
Y	spanwise distance between centerlines of adjacent impingement holes
Z	distance between target plate and impingement hole plate
α	air thermal conductivity
ρ_a	impingement air static density
μ	absolute viscosity

3, X/D and Y/D ranging from 6 to 32, and Reynolds numbers from 5×10^3 to 2×10^4. Florschuetz et al. [5] describe another low-speed investigation wherein Reynolds numbers range from 2.5×10^3 to 7×10^4. Considered are inline and staggered hole patterns, Z/D from 1 to 3, X/D from 5 to 15, and Y/D from 4 to 8. Impinging air is constrained to exit in a single direction from the channel formed between the impingement plate and the target plate. Included is a correlation which gives Nusselt number dependence on flow parameters, jet impingement plate geometry, Prandtl number, and Reynolds number. Effects of jet-to-target-plate distance in low speed flows are also considered by Obot and Trabold [6]. In this investigation, considered are impingement jet Reynolds numbers from 1×10^3 to 2.1×10^4, Z/D values from 2 to 16, X/D values of 5 and 10, and Y/D values of 4 and 8. According to these investigators, for a given crossflow scheme and constant jet diameter D, higher heat transfer coefficients are obtained as the number of jets over a fixed target area increases.

San et al. [7] present correlation equations, also for low-speed arrangements, which show that stagnation Nusselt numbers are proportional to the 0.7 power of Reynolds number, and the −0.49 power of the ratio of jet plate width to jet diameter. Investigated are ratios of jet target distance to jet diameter from 1 to 4, lateral and streamwise jet spacing ratios from 4 to 8, ratios of jet plate width to jet diameter ratio from 6.25 to 18.75, and Reynolds numbers from 5×10^3 to 1.5×10^4. Miao et al. [8] consider fluid flow and heat transfer characteristics of round jet arrays impinging orthogonally onto a flat-plate with confined walls and different crossflow arrangements. Computational fluid dynamics results are

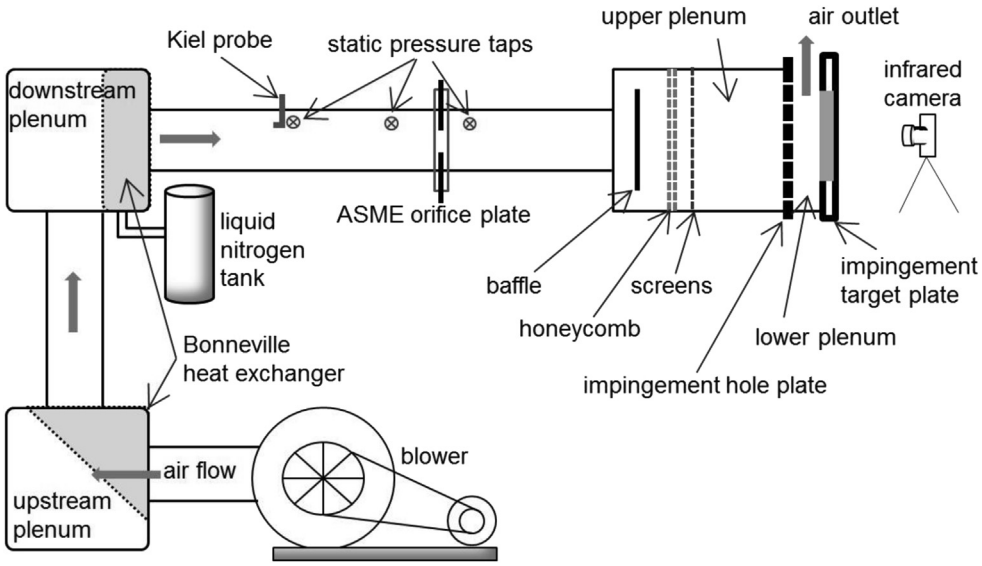

Fig. 1. Impingement flow facility.

obtained for in-line and staggered hole arrays, with parallel, hybrid, and counter cross-flow configurations. Jet Reynolds numbers range from 2.44×10^3 to 1.46×10^4, and Z/D values of 1, 3, and 6 are utilized. According to these investigators, the thermal performance of multiple jet impingement is enhanced when Z/D decreases from 6 to 3, which is illustrated by correlation equations for area-averaged Nusselt number as dependent upon jet Reynolds number. Vadiraj and Prabhu [9] consider the influences of spanwise pitch jet spacing on local heat transfer distributions for in-line rectangular arrays of jets. Impingement jet Reynolds numbers range from 3×10^3 to 1×10^5, jet-to-target plate spacing ranges from 1 to 3 hole diameters, the X/D value is 5, and Y/D values vary from 2 to 6.

The present study provides experimental data for impingement configurations and flow conditions which have not been previously investigated. Of particular importance are new impingement heat transfer data which illustrate the combined and separate effects of hole array spacing, jet-to-target plate distance, and Reynolds number on *cross-flows* for an impingement jet array. Included is conduction analysis of the impingement cooling array target surface. The impingement holes are arranged with a staggered array from one streamwise row to the next. The thickness of each impingement plate is 1D, where D is the impingement hole diameter. Considered are Reynolds numbers ranging from 8000 to 50,000, jet-to-target-plate distances of 1.5D, 3.0D, 5.0D, and 8.0D, and steamwise and spanwise hole spacings of 5D, 8D, and 12D. Mach numbers range from 0.10 to 0.22, and as such, are low enough that spatially-averaged Nusselt number data generally show no Mach number dependence. Presented are local, line-averaged, and spatially-averaged target surface Nusselt numbers.

The present study is also different from many other impingement array investigations [1–3,6–9] because a staggered hole array is utilized. Compared to other studies wherein staggered hole arrays are also employed [4,5], the present results are different because a wider range of Z/D values are employed, and because the combined and separate effects of jet-to-target plate distance, jet array hole spacing, and impingement jet Reynolds number are considered. This is significant because different jet-to-target-plate distances, with different hole spacings at different Reynolds numbers, result in different amounts of coherence of the shear layers which form adjacent to impingement jets. In addition, the interactions of the vortex structures which initially form around the jets change as different parameters are varied, especially as they then impact and then advect away from stagnation points along the impingement target surface. The present investigation is also important because high-accuracy, spatially-resolved, local Nusselt number distributions are included, along with line- and spatially-averaged Nusselt number results.

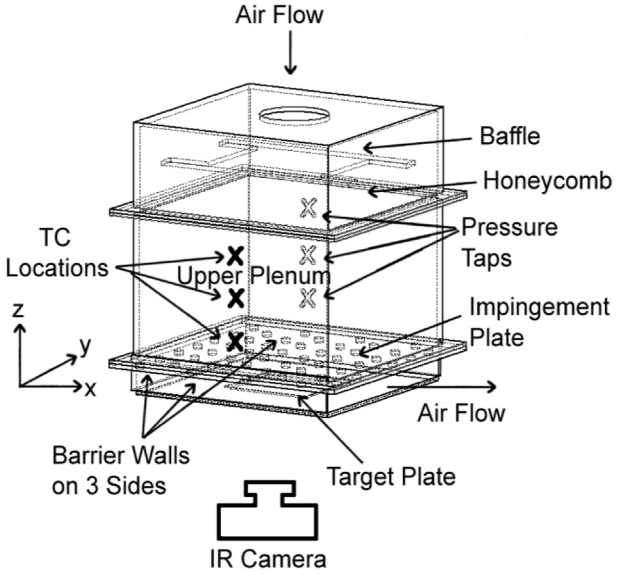

Fig. 2. Impingement flow facility test section, including impingement plenum, and impingement channel.

2. Experimental apparatus and procedures

2.1. Impingement flow facility, and impingement plate

Schematic diagrams of the laboratory facility used for heat transfer measurements are presented in Figs. 1 and 2. The facility is constructed of 6.1 mm thick ASTM A38 steel plates, and A53 Grade B ARW steel piping. The air stream through the plenums and channel is drawn from the laboratory atmosphere. To achieve the Reynolds number of the present study, a New York Blower Co. 7.5 HP, size 1808 pressure blower is employed. The air mass flow rate provided to the test section is measured using an ASME standard orifice plate, flow-mounted calibrated copper-constantan thermocouples, and Validyne DP15-22 and DP15-32 pressure transducers (with diaphragms rated at 1.40 and 14.0 kPa, respectively) connected to Validyne Model CD15 Carrier Demodulators. Each of these thermocouples measures recovery temperature, which is used with local velocity magnitude to determine gas static temperature. The blower exits into a series of two plenums arranged in series, where the upstream plenum is 0.63 m in length along each side, and the downstream plenum dimensions are 0.63 m long, 0.77 m tall, and 0.77 m wide. A Bonneville cross-flow heat exchanger is located within each plenum. As the air exits the heat exchanger, and the second plenum, the air passes into a 0.22 m outer diameter pipe, which contains the ASME Standard orifice plate employed to measure the air mass flow rate. This pipe then connects to the 0.635 m by 0.635 m side of a plenum. Upon entering this plenum, the air first encounters a flow baffle to distribute the flow, and a honeycomb and screens to straighten the flow. These are followed by the upper plenum, located below the honeycomb and flow straightening devices (as shown in Fig. 2), with top dimensions of 0.635 m and 0.635 m, and height of 0.40 m.

Individual plates with holes used to produce the impingement jets are located at the bottom of this plenum, as shown in Fig. 2. The plenum is thus designed so that different impingement plates can be installed at this location. Fig. 3 shows that each impingement plate consists of 7–10 rows of holes in the streamwise direction, arranged so that holes in adjacent rows are staggered with respect to each other. With this arrangement, from 3 to 10 holes are located in each streamwise row. The spacing between holes in the streamwise direction X is either 5D, 8D, or 12D, and the spacing between holes in the spanwise direction Y is either 5D, 8D, or 12D. The thickness of each impingement plate is 1D. The spacing between the hole exit planes and the target plate is denoted Z/D, with values employed in the present investigation of 1.5, 3.0, 5.0, and 8.0. Note that the coordinate systems employed are also shown in Fig. 3. The impingement cooling flow which issues from these holes is contained within the channel formed by the impingement jet plate and the target surface, and is constrained to exit in a single direction, which here, is denoted as the x-direction. This channel is called the lower plenum or impingement plenum. The impingement plenum channel is made up of a volume of air between the target and jet impingement plate, with 4D spanwise margins on each side. In the present study, the hole diameter size, D, blower, mass flow rate, and pressure level are employed so that the Mach number ranges from 0.1 to 0.2 and the Reynolds number is between

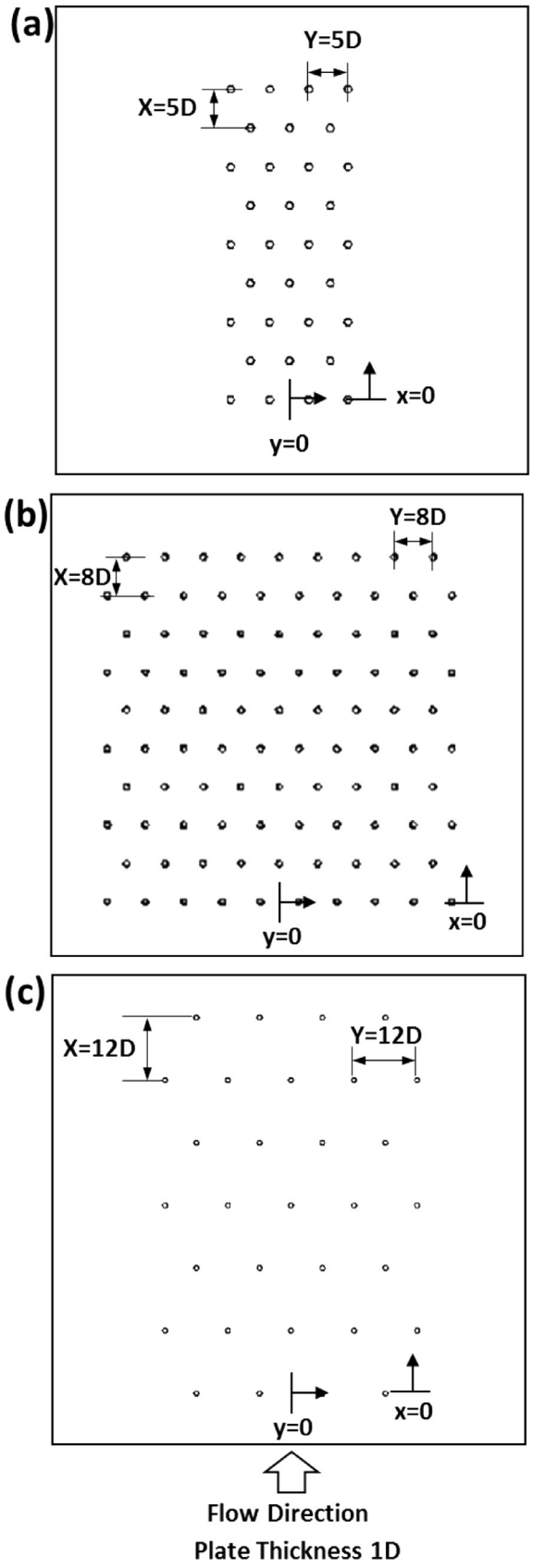

Fig. 3. Impingement test plate configurations. (a) $X/D = Y/D = 5$. (b) $X/D = Y/D = 8$. (c) $X/D = Y/D = 12$.

7700 and 52,000. This range of Mach numbers are selected because previous investigations show that local and spatially-averaged Nusselt numbers show no dependence on Mach number, when values are less than approximately 0.25.

2.2. Target plate test surfaces for measurements of surface Nusselt numbers

Local surface Nusselt numbers are measured on a heated target plate, which is comprised of polystyrene layer which is 1.31 mm thick, and an attached heater, which is approximately 0.29 mm thick, giving a total target plate thickness of 1.60 mm. The size of the target plate is 126 mm by 254 mm. The heater is located adjacent to the air stream with the impinging air jets, and the back side of this polystyrene plate is viewed by the infrared camera as spatially-resolved measurements of surface temperature are obtained.

The target plate is mounted on the bottom surface of the impingement plenum. Eight type-T copper-constantan thermocouples are placed at different streamwise and spanwise locations within the polystyrene target plate so that each senses a different temperature as data are acquired. These provide measurements of local surface temperatures, after correction for thermal contact resistance and temperature drop through the 0.016 cm thickness of polystyrene. Thermocouple lead wires are placed in grooves along the polystyrene, and bonded into place with epoxy having approximately the same thermal conductivity as polystyrene, to minimize thermal disturbances resulting from their presence. The custom-made HK5184R26 thermo-foil heaters are manufactured by Minco Products Inc. Each heater is encased between two layers of DuPont Kapton polyimide film. This heater provides a constant surface heat flux boundary condition adjacent to the impingement air stream. Each target plate assembly is mounted within a frame to minimize distortion and shape variations which may occur as heat transfer tests are underway. Each target plate is also replaced after 3 or 4 test sequences with a new plate, because of shape changes which occur within the plates when they are utilized for more than this number of repeated test sequences.

Additional target plate test surface details are provided by Park et al. [10] and Goodro et al. [11].

2.3. Local impingement air pressure and temperature measurements

As shown in Fig. 2, three wall static pressure taps are located on the surface of the upper plenum. Two wall pressure taps are also located on the surface of the lower plenum for measurement of local static pressures. As tests are conducted, calibrated Validyne Model DP15-22 and DP15-32 pressure transducers driven by Validyne Model CD15 Carrier Demodulators are used to sense pressures from these static pressure taps. Local air flow recovery temperatures are measured using 2 Ω T-type copper-constantan thermocouples located in the central part of the lower plenum,

Table 1
Experimental uncertainty magnitudes for the local Nusselt number, and quantities employed to determine the local Nusselt number.

Quantity	Xi	δXi	
A_{ht}	0.03175 m^2	0.0005	
D	0.015 m	0.00025	
T_W	36.35 °C	0.85	
T_{oj}	22.9 °C	0.15	
α	0.0226 W/(m K)	0.000138	
Total Nusselt number uncertainty (percent)			*8.2*

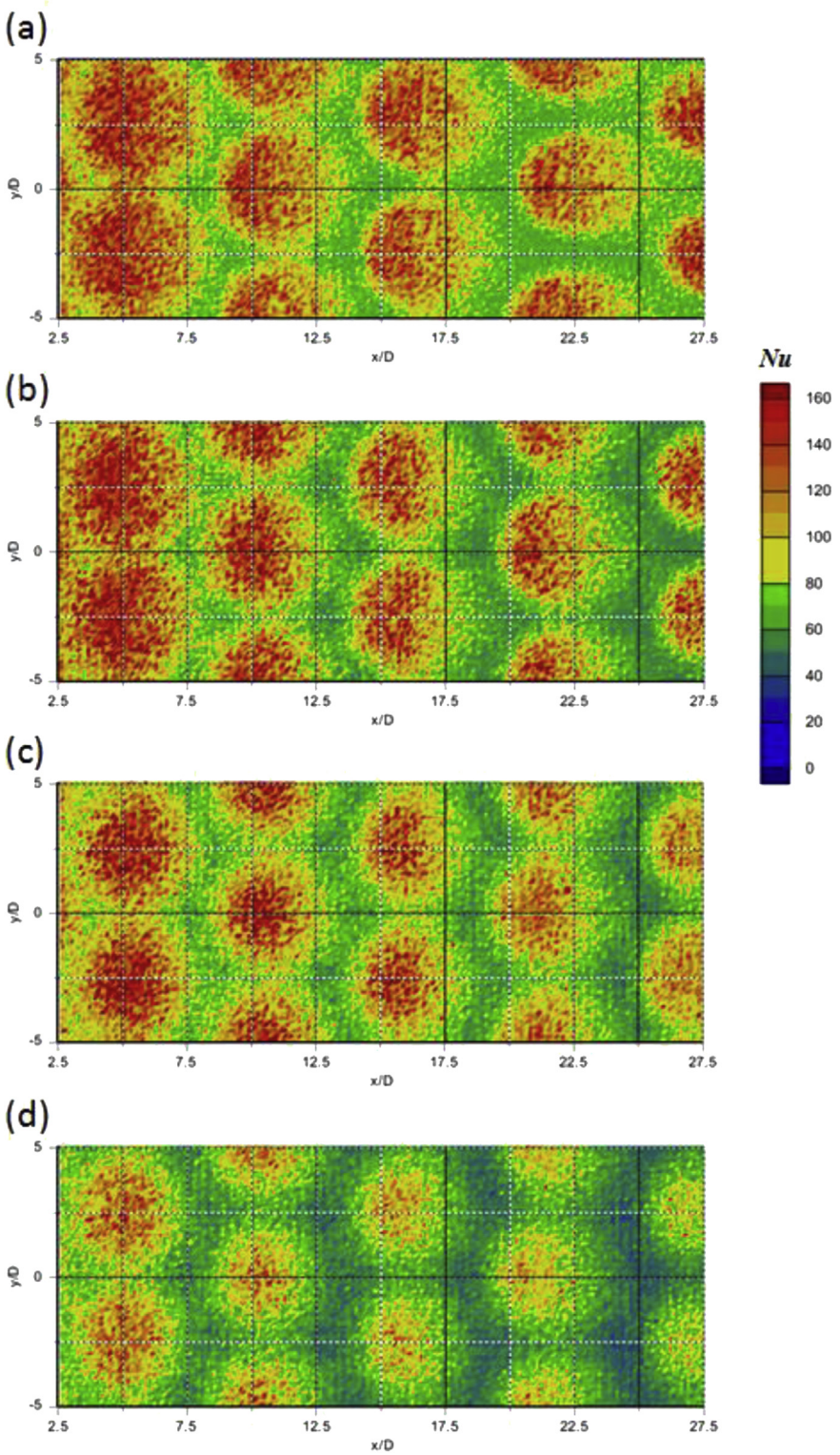

Fig. 4. Local surface Nusselt number variations for $Re_j \approx 30{,}000$ for different Z/D values and $X/D = Y/D = 5$. (a) $Z/D = 1.5$. (b) $Z/D = 3.0$. (c) $Z/D = 5.0$. (d) $Z/D = 8.0$.

and three copper-constantan thermocouples located in the central part of the upper plenum. Voltages from the carrier demodulators and all thermocouples employed in the study are read sequentially using National Instruments NI-USB 6210 and NI-USB 9162 Data Acquisition terminals, respectively. These terminals relay the information to a Dell Precision T3500 computer. The voltage outputs from this unit are acquired by the computer through its USB port, using LABVIEW 10.0 software.

An iterative procedure is then used to determine the impingement static temperature T_j, and the impingement flow Mach number M_a. With impingement static temperature T_j, impingement flow Mach number M_a, and other parameters known, the

impingement Reynolds number is subsequently given by an equation of the form.

$$Re_j = \rho_a u_a D/\mu \quad (1)$$

Note that Re_j is equivalent to $4\dot{m}/\pi ND\mu$, where N is the total number of impingement holes.

A Kiel-type stagnation pressure probe is used to measure the total pressure in the pipe at a position which is located upstream of the orifice plate employed to measure mass flow rate. A wall pressure tap located on the surface of the pipe, and a calibrated copper-constantan thermocouple positioned within the air stream are used to sense static pressure and flow recovery temperature, respectively, at the same streamwise location. Pressures and temperatures measured using the thermocouple, probe, and tap are sensed and processed using the same types of instrumentation mentioned earlier. The velocities deduced from this arrangement are used to provide a cross-check on the velocities deduced from mass flow rates, which are measured using the ASME standard orifice plate.

Park et al. [10] and Goodro et al. [11] provide additional measurement details on related apparatus and procedures.

2.4. Local Nusselt number measurements

The power to the thermo-foil heater, mounted on the target plate, is controlled and regulated using an alternating current to direct current Price-Putzebeck POW-R-PAC 160 V transformer power supply. The power supply is directed by a covered switchboard where the voltage is read by a Fluke 8846 A 6.5 Digit Precision Multimeter, and the amperage is read by both a Simpson 260 Series 8P Ammeter and an Agilent 34401 A Digit Benchtop Multimeter. Energy balances, and analysis to determine temperature values on the two surfaces of the target plate, then allow determination of the magnitude of the total convective power (due to impingement cooling) for a particular test. To determine the surface heat flux (used to calculate heat transfer coefficients and local Nusselt numbers), the total convective power level, provided by the particular thermo-foil heater employed, is divided by the single surface area of this heater, denoted A_{ht}.

One step in this procedure utilizes a one-dimensional conduction analysis, which is applied between the surface *within* the target plate where the thermocouples are located (between the heater and the polystyrene target plate), and the ambient air environment behind the target plate. This is used to determine T_b, the local temperature on the back surface of the polystyrene target plate, adjacent to the surrounding ambient air environment. Also required for this analysis is T_{tc}, the local temperature within the target plate between the heater and the polystyrene plate, which is determined from thermocouple measurements. With these temperatures known, the radiation heat flux and the convection heat flux from the back side of the target plate, q_{rb} and q_{cb}, respectively, are determined [10,11]. The radiation heat flux q_{rf} on the front (or impingement side) of the target plate is determined using the appropriate analytic and empirical equations [10,11]. Note that T_W, the local target surface temperature on the surface of the heater adjacent impingement air, must be known to determine q_{rf}. Because of the inter-dependence of T_W, q_{rf}, and q_{cf} (the convection heat flux from the front side or impingement side of the target plate), an iterative procedure is required to determine these quantities. The next part of this procedure uses a one-dimensional conduction analytical model for the heater, which includes source generation of thermal energy, to provide a relation between T_W, T_{tc}, and q_{cf}. Also included in the analysis is thermal contact resistance between the internal thermocouples and the adjacent heater. This one-dimensional conduction approach is employed since magnitudes of lateral conduction within the target plate are very small and mostly insignificant (from three-dimensional analyses), relative to impingement convective heat flux levels.

The convection heat flux from the front side (or impingement side) of the target plate is then given by.

$$q_{cf} = Q/A_{ht} - q_{rf} - q_{rb} - q_{cb} \quad (2)$$

The local Nusselt number is then given as.

$$Nu = q_{cf}D/((T_W - T_{oj})\alpha) \quad (3)$$

As impingement heat transfer measurements are made, spatially-resolved distributions of the target test surface temperature T_W are determined using infrared imaging in conjunction with thermocouples, energy balances, digital image processing, and *in situ* calibration procedures. These are then used to determine spatially-resolved surface Nusselt numbers. To accomplish this, the infrared radiation emitted by the polystyrene surface of the impingement test plate is captured using a ImagIR InSB Digital 320×256 infrared camera, which operates at infrared wavelengths from 5.2 μm to 9.1 μm. Temperatures, measured using the calibrated, copper-constantan thermocouples distributed along the test surface adjacent to the flow, are used to perform the *in situ*

Table 2
Impingement test plate configurations and experimental conditions [14].

X/D, $Y/D = 5$				X/D, $Y/D = 8$				X/D, $Y/D = 12$			
Z/D	Re_j	M_a	D(mm)	Z/D	Re_j	M_a	D(mm)	Z/D	Re_j	M_a	D(mm)
1.5	8000	0.14	4.5	1.5	8200	0.13	4.5	1.5	8000	0.14	3.5
3.0	8000	0.11	4.5	3.0	8200	0.11	4.5	3.0	8000	0.13	3.5
5.0	8000	0.10	4.5	5.0	8200	0.10	4.5	5.0	8000	0.13	3.5
8.0	8000	0.10	4.5	8.0	8200	0.10	4.5	8.0	8000	0.13	3.5
1.5	20,000	0.17	8.0	1.5	20,900	0.15	8.0	1.5	20,000	0.13	8.0
3.0	20,000	0.14	8.0	3.0	20,900	0.14	8.0	3.0	20,000	0.14	8.0
5.0	20,000	0.14	8.0	5.0	20,900	0.14	8.0	5.0	20,000	0.14	8.0
8.0	20,000	0.14	8.0	8.0	20,900	0.14	8.0	8.0	20,000	0.13	8.0
1.5	30,000	0.24	8.0	1.5	31,000	0.23	8.0	1.5	30,000	0.21	8.0
3.0	30,000	0.21	8.0	3.0	31,000	0.21	8.0	3.0	30,000	0.21	8.0
5.0	30,000	0.20	8.0	5.0	31,000	0.22	8.0	5.0	30,000	0.21	8.0
8.0	30,000	0.20	8.0	8.0	31,000	0.21	8.0	8.0	30,000	0.21	8.0
1.5	50,000	0.21	15	1.5	52,000	0.22	15	1.5	50,000	0.21	15
3.0	50,000	0.21	15	3.0	52,000	0.21	15	3.0	50,000	0.20	15
5.0	50,000	0.21	15	5.0	52,000	0.21	15	5.0	50,000	0.20	15
8.0	50,000	0.21	15	8.0	52,000	0.21	15	8.0	50,000	0.20	15

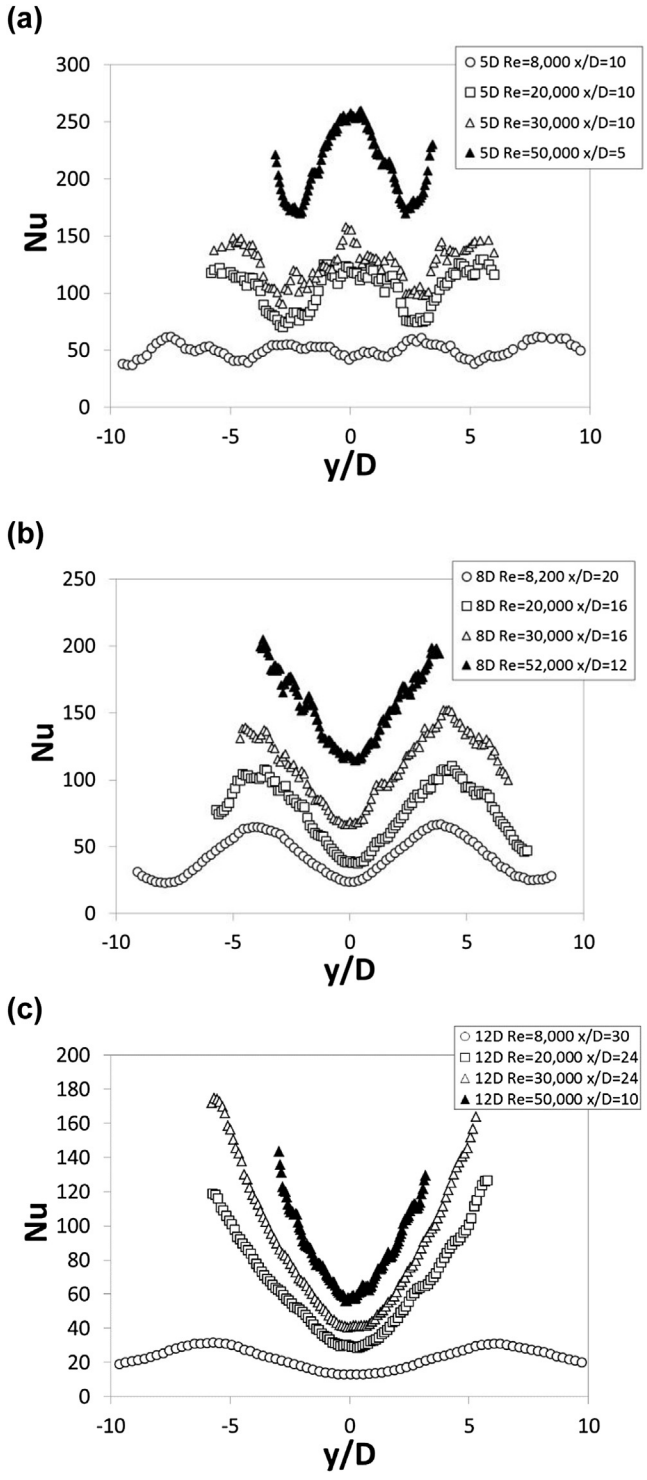

Fig. 5. Local Nusselt number variations for $Z/D = 3.0$ for different Re_j values of 8,000, 20,000, 30,000, and 50,000. (a) 5*D* hole spacing, spanwise variations. (b) 8*D* hole spacing, spanwise variations. (c) 12*D* hole spacing, spanwise variations.

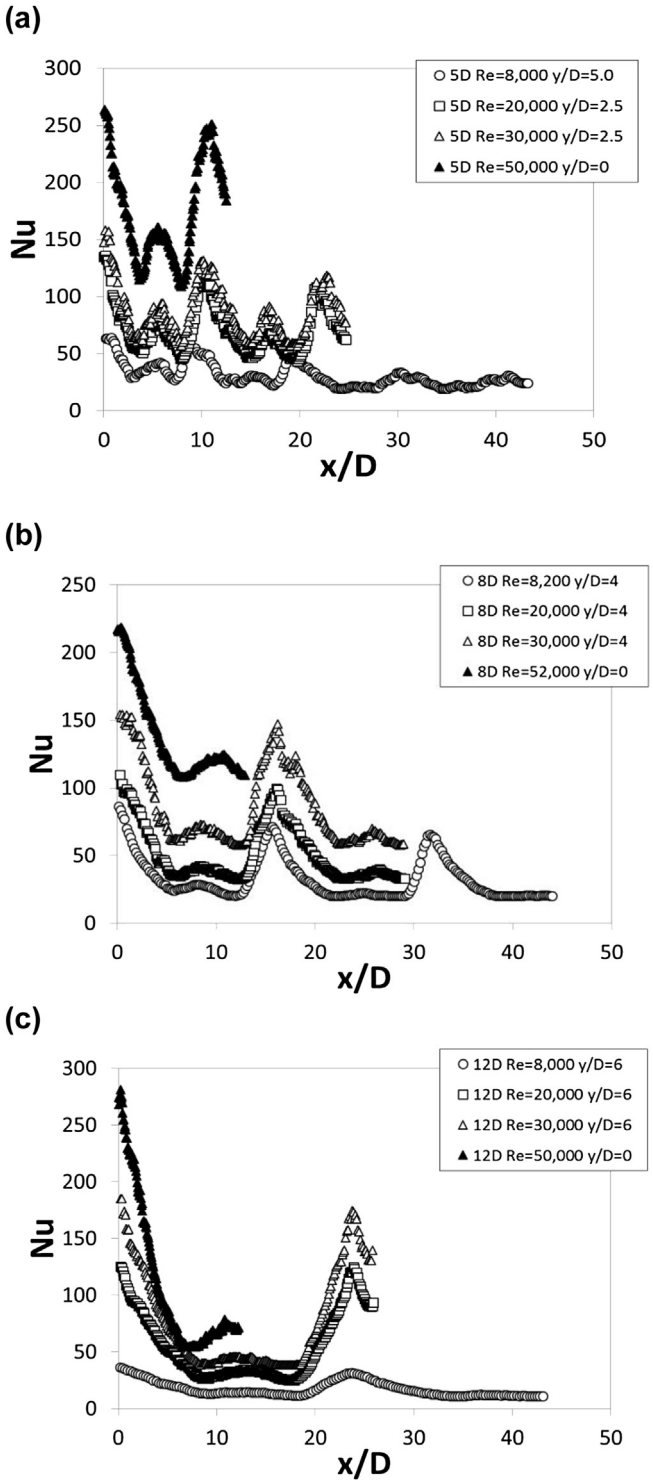

Fig. 6. Local Nusselt number variations for $Z/D = 3.0$ for different Re_j values of 8,000, 20,000, 30,000, and 50,000. (a) 5*D* hole spacing, streamwise variations. (b) 8*D* hole spacing, streamwise variations. (c) 12*D* hole spacing, streamwise variations.

calibrations simultaneously as the radiation contours from surface temperature variations are recorded.

This is accomplished as the camera views the test surface from behind, as shown in Fig. 2. In general, all eight thermocouple junction locations are present in the infrared field viewed by the camera. The exact spatial locations and pixel locations of these thermocouple junctions and the coordinates of the field of view are known from calibration maps obtained prior to measurements. During this procedure, the camera is focused, and rigidly mounted and oriented relative to the test surface in the same way as when radiation contours are recorded. Voltages from the thermocouples are acquired using the apparatus mentioned earlier.

Images from the infrared camera are recorded as 8-bit gray scale directly into the memory of a Dell Precision T3500 computer using

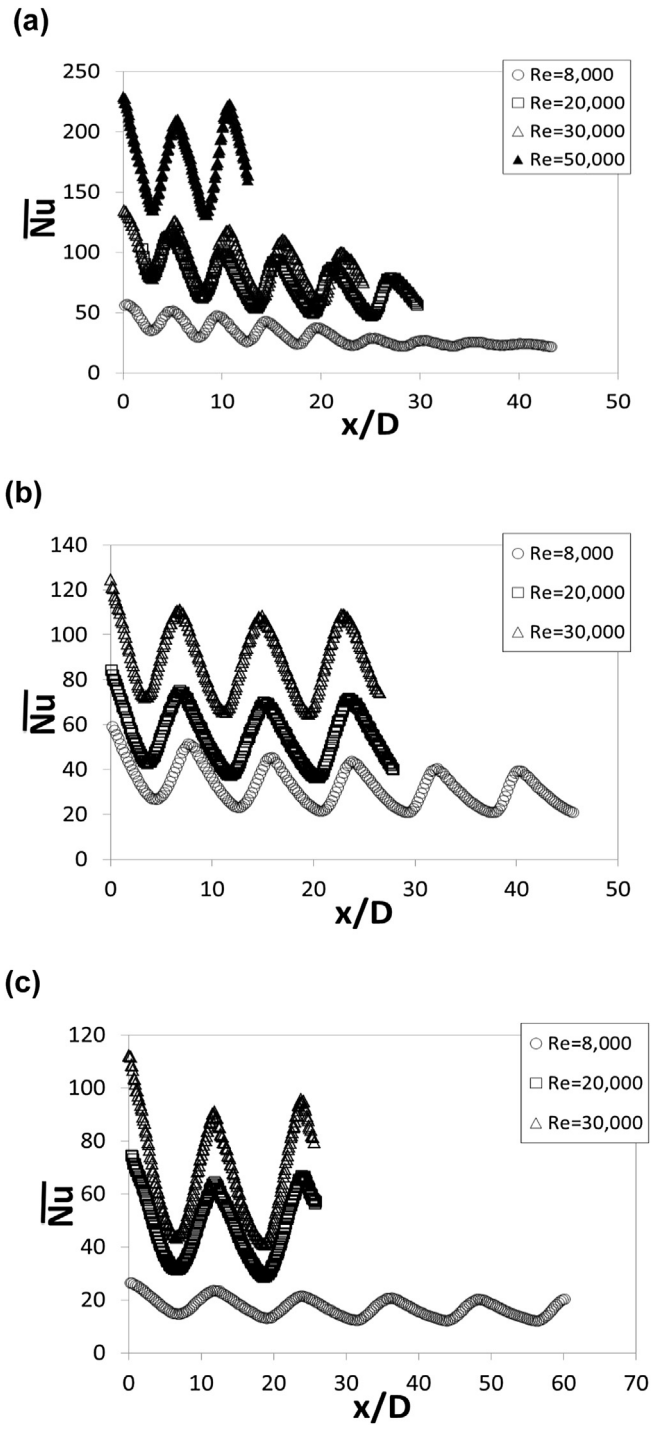

Fig. 7. Line-averaged Nusselt number variations for $Z/D = 3.0$ for different Re_j values of 8,000, 20,000, 30,000, and 50,000. (a) 5D hole spacing. (b) 8D hole spacing. (c) 12D hole spacing.

a MATROX Frame grabber video card and the infrared camera interface program, WINIR. One set of 50 frames is taken in ten frames sets at five random intervals. All of the resulting images are then ensemble averaged to obtain the final gray scale data image. This final data set is then imported into MATLAB software to convert each of 256 possible gray scale values to local Nusselt number at each pixel location using calibration data. Each individual image covers a 256 pixel by 320 pixel area.

Park et al. [10] and Goodro et al. [11] provide additional details regarding local Nusselt number measurement apparatus and procedures.

2.5. Experimental uncertainty estimates

Uncertainty estimates are based on 95 percent confidence levels and are determined using methods described by Kline and McClintock [12] and Moffat [13]. Uncertainty of temperatures measured with thermocouples is ±0.15 °C. Spatial and temperature resolutions achieved with infrared imaging are about 0.1 mm–0.2 mm, and 0.4 °C, respectively. This magnitude of temperature resolution is due to temperature resolution is due to uncertainty in determining the exact locations of thermocouples with respect to pixel values used for the *in situ* calibrations. Of the different quantities considered, the uncertainty associated with surface temperature (with a maximum value of approximately ±0.85 °C) makes the largest contribution to overall Nusselt number uncertainty. Note that the overall Nusselt number uncertainty also includes possible contributions from lateral conduction within the test plates, although, in general, magnitudes of lateral conduction (in the x and y directions) are generally insignificant relative to overall convective heat flux levels from impingement.

Numerical predictions of target plate internal conduction, using SC/Tetra Version 10, indicate that Nusselt number variations from lateral conduction within the target plate are less than the overall Nusselt number experimental uncertainty. These predictions also show that lateral conduction magnitudes are very small or negligible for the $X/D = Y/D = 5$, $Re_j \approx 30{,}000$, $Z/D = 3.0$ test case. As such, no significant alteration of surface Nusselt number distributions or surface temperature distributions are present from lateral conduction (which occurs in the x and y directions).

Table 1 shows that the total local Nusselt number uncertainty is approximately ±8.2 percent. This uncertainty magnitude represents the maximum value which is encountered for all test conditions within the present investigation.

3. Experimental results and discussion

3.1. Spatially-resolved local Nusselt numbers

Fig. 4 shows spatially-resolved surface Nusselt number distributions for $X/D = Y/D = 5$ hole spacing for Re_j of approximately 30,000. From Table 2 [14], associated Mach numbers M_a range between 0.20 and 0.24. Because these values are less than 0.25, little or no Mach number dependence is present in regard to spatially-averaged.

Nusselt number distributions [10]. Note that a different view of the test surface is apparent in Fig. 4, compared to local data in the figures which follow for other Reynolds number values. This is because of different infrared camera views of the target plate are used as different impingement plates are employed. This is because the impingement plates which are employed are different sizes with different sizes of hole diameters. Note that Table 2 also provides the dimensional hole diameters utilized to obtain the different data sets. Changing the impingement plate hole diameter provides a means to alter the impingement jet air flow Reynolds number as the impingement jet Mach number is maintained approximately constant. No other hole diameter or jet size effect is observed in the present data.

Regardless of the Reynolds number and Z/D value, qualitative distributions of local Nusselt numbers produced by each impingement jet are generally similar, with good quantitative periodic repeatability in the spanwise direction for each streamwise row of impact locations. Note that the highest local maximum Nusselt numbers in Fig. 4 are associated with $Z/D = 3.0$ and $Z/D = 1.5$. Fig. 4

also shows that local Nusselt number *peak values* for 5*D* hole spacing generally become smaller at successive x/D locations for each value of Z/D and Re_j. This is due to the detrimental effects of spent air crossflow on impingement coolant distributions. Local maximum *Nu* values are spaced approximately 5*D* apart in the streamwise direction, as a result of the impacts of different impingement jets onto the target surface. These spacings increase somewhat with streamwise development due to bending and rearrangement of coolant concentrations by spent air crossflow, which accumulates in a progressive manner, as additional streamwise rows of holes are encountered.

3.2. Spatially-resolved local Nusselt numbers – effects of Reynolds number and hole spacing

Figs. 5 and 6 give local Nusselt number variations for $Z/D = 3.0$ for different Re_j values of 8,000, 20,000, 30,000, and 50,000. Here, the results in part a of both figures are presented for 5*D* hole spacing, the results in part b of both figures are presented for 8*D* hole spacing, and the results in part c of both figures are given for 12*D* hole spacing. In all parts of Fig. 5, spanwise variations with y/D are shown, presented for fixed values of x/D. In all parts of Fig. 6, streamwise variations with x/D are shown, presented for fixed values of y/D. These fixed values of y/D and x/D are selected to provide local Nusselt number variations which are representative of the associated experimental conditions for each data set. In all cases, locally increased surface Nusselt number variations are present beneath jet impingement impact locations. Fig. 6 also shows secondary Nusselt number peaks which correspond to spanwise locations between jet impingement impact locations. In general, local Nusselt numbers increase with increasing Reynolds number at each x/D and y/D test surface location.

3.3. Line-averaged Nusselt numbers – effects of Reynolds number and hole spacing

Fig. 7 presents line-averaged Nusselt number variations for $Z/D = 3.0$ for different Re_j values of 8,000, 20,000, 30,000, and 50,000. Here, the results are given for 5*D* hole spacing, 8*D* hole spacing, and 12*D* hole spacing in the a, b, and c parts of the figure.

Comparison of results in Fig. 7 shows that line-averaged Nusselt numbers at each x/D and y/D location generally increase continually as the impingement jet Reynolds number Re_j increases. For the $X/D = Y/D = 8$ and $X/D = Y/D = 5$ hole spacings, in particular, the influences of surrounding jets, including the cumulative accumulation of cross-flows from sequential rows of jets, reduce the effectiveness of each individual jet (especially for jets at larger x/D locations). The result is sequentially decreasing periodic line-averaged Nusselt number variations with x/D. The data in Fig. 7 indicate that such detrimental effects become more significant as the Reynolds number increases. Another effect of crossflow is varying individual jet spatially-averaged velocity, and local blowing ratio along the length of the impingement channel. Such local blowing ratio variations are a result of local changes of static pressure and passage flow velocities, as sequential amounts of impingement air accumulate with increasing x/D [10,11].

Note that x/D and y/D ranges of values, and the numbers of impingement jet events are different in Figs. 5–9, as well as in many figures which follow. This is because the dimensional field of view of the camera is approximately invariant, and because different Reynolds numbers are produced using impingement holes with different diameters (see Table 2) with all associated configuration parameters scaled accordingly.

Note that investigations by Park et al. [10] and Goodro et al. [11] compare $Z/D = 3$ data with results from Florschuetz et al. [5]. These comparisons show that baseline data are in good agreement with

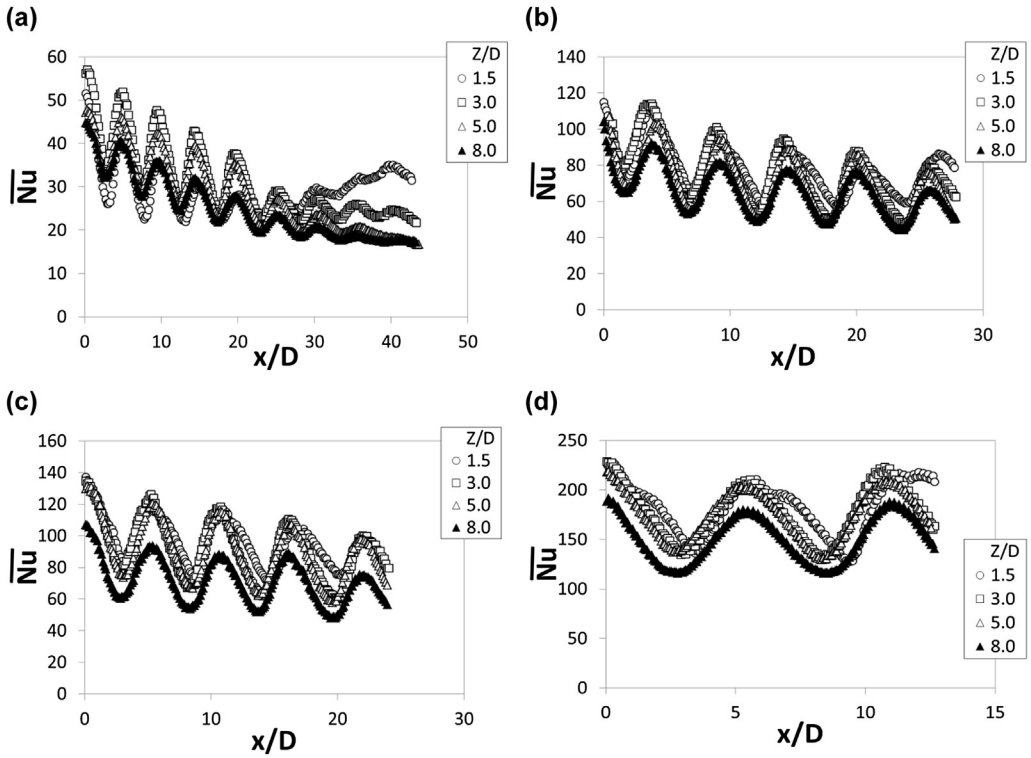

Fig. 8. Line-averaged Nusselt number variations for 5*D* hole spacing, for different Z/D values of 1.5, 3.0, 5.0, and 8.0. (a) $Re_j \approx 8000$. (b) $Re_j \approx 20{,}000$. (c) $Re_j \approx 30{,}000$. (d) $Re_j \approx 50{,}000$.

spatially-averaged data from Florschuetz et al. [5] at similar experimental conditions.

3.4. Line-averaged Nusselt numbers – effects of jet-to-target plate distance and Reynolds number

Fig. 8 presents line-averaged Nusselt number variations for 5*D* hole spacing, for different *Z*/*D* values of 1.5, 3.0, 5.0, and 8.0. Within the a, b, c, and d parts of this figure, data are given for Reynolds number Re_j values of 8,000, 20,000, 30,000, and 50,000, respectively. These Nusselt numbers are line-averaged over *y*/*D* from −5.0 and +5.0 for a hole spacing of 5*D*.

Consideration of these results at particular values of Re_j and *Z*/*D* shows that periodic line-averaged Nusselt numbers generally decrease at the successive *x*/*D* locations. This occurs such that successive maximum and minimum values become lower and lower as the impingement flows advect downstream. Fig. 8a–c (for Re_j of 8,200, 20,000, and 30,000, respectively) also show that data generally increase as *Z*/*D* approaches 3.0 (either from above or below) near jet impact locations (where local *maxima* locations are present in line-averaged $\overline{Nu}$ data). Somewhat smaller changes with *Z*/*D* are evident at locations where local $\overline{Nu}$ *minima* are present at different Re_j values. For Re_j = 20,900, in particular, almost no changes with *Z*/*D* are evident between jet impact regions where $\overline{Nu}$ are minimum. Fig. 8d shows that line-averaged Nusselt numbers increase at most all *x*/*D* locations as *Z*/*D* approaches 3.0 to 5.0 (either from above or below) for Re_j = 52,000. Such variations are due, in part, to the coherence of the shear layers which form near the edges of the impingement jets, and the unsteady vortex structures and vortex rings which initially form around the periphery parts of the impingement jets [10,11,15–18]. Associated local and line-averaged Nusselt number decreases with increasing *Z*/*D* (at most all *x*/*D* and *y*/*D* values) are due to diminished jet coherence, as well as diminished coherence of associated Kelvin–Helmholtz generated vortices, which occur as jet advection distances become larger [10,11].

Also important are cross-flow effects. In general, the cumulative accumulations of cross-flows, from sequential rows of jets, result in sequentially decreasing periodic Nusselt number variations with streamwise development. In general, Figs. 7 and 8 show that these decreases become more pronounced as the Reynolds number increases, and as hole spacing decreases. The data in Fig. 8 also show that streamwise locations of local maximum line-averaged Nusselt numbers shift to larger *x*/*D* locations as the normalized jet-to-target distance increases, for each value of Re_j, This occurs because of larger advection distances between the impingement hole exits and the target plate, as *Z*/*D* increases. As this occurs, crossflows exert greater influences in shifting the locations of jet impact stagnation points.

Kelvin–Helmholtz instability generated vortices, which are present along the interface between each jet and the surrounding air, prior to their impingement upon the target plate, also play a role in this process [10,11,15]. Popiel and Trass [16], Angioletti et al. [17], and O'Donovan and Murray [18] also consider the development and effects of Kelvin–Helmholtz generated vortices around impingement jets.

Fig. 8a–d shows that cross-flows can also result in local augmentation of Nusselt numbers. Such behavior is evident for 5*D* hole spacing, Re_j = 8,000, and *Z*/*D* of 1.5, 3.0 in Fig. 8a, provided $x/D \geq 30$. Fig. 8b–d show local line-averaged Nusselt number increases from cross-flow effects at larger *x*/*D* locations when Re_j is 20,000, 30,000, and 50,000, and *Z*/*D* = 1.5. Such Nusselt number augmentations occur as interactions between impingement jets become more vigorous. As a result, local magnitudes of mixing and turbulent transport are increased. This occurs most often in channels at lower Reynolds numbers, where impingement jet fluid distributions are confined by smaller hole spacing, and smaller jet-to-target plate distance.

3.5. Line-averaged Nusselt numbers – effects of hole spacing and Reynolds number

Fig. 9 presents line-averaged Nusselt number variations for different *X*/*D* = *Y*/*D* hole spacing values for a jet-to-target-plate distance *Z*/*D* value of 3. Data are presented in parts a, b, and c for

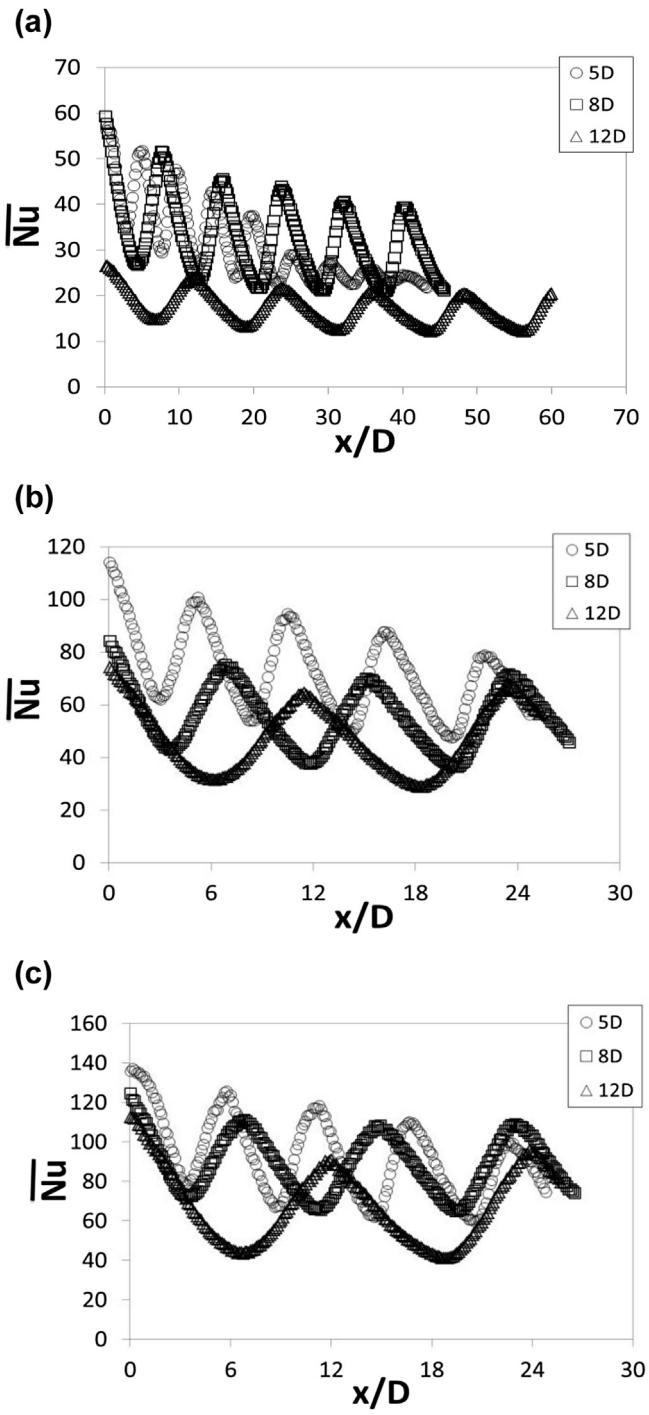

Fig. 9. Line-averaged Nusselt numbers for Z/*D* = 3 for different *X*/*D* = *Y*/*D* hole spacing values of 5, 8, and 12. (a) $Re_j \approx$ 8000. (b) $Re_j \approx$ 20,000. (c) $Re_j \approx$ 30,000.

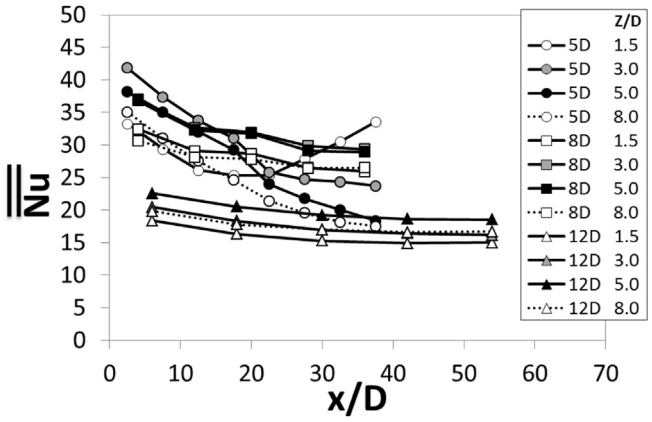

Fig. 10. Spatially-averaged Nusselt numbers for $Re_j \approx 8000$ as dependent upon x/D, hole spacing, and Z/D value.

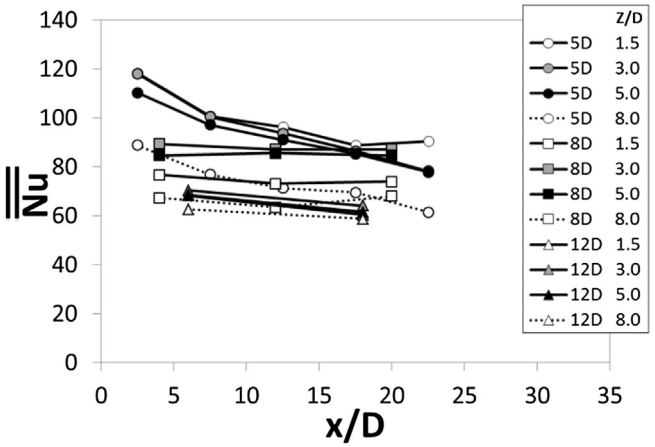

Fig. 12. Spatially-averaged Nusselt numbers for $Re_j \approx 30{,}000$ as dependent upon x/D, hole spacing, and Z/D value.

Reynolds number Re_j values of 8,000, 20,000, and 30,000, respectively. These Nusselt numbers are line-averaged over y/D from −5.0 and +5.0 for a hole spacing of 5D, over y/D from −4.0 and +4.0 for a hole spacing of 8D, and over y/D from −6.0 and +6.0 for a hole spacing of 12D. Note that values presented in Fig. 9 correctly represent line-averaged magnitudes, even though different span dimension extents are used to determine line-averaged Nusselt numbers for different hole spacing arrangements.

Overall, the line-averaged data in Fig. 9a–c shows that x/D locations of Nusselt number maxima are wider apart and more spread out as $X/D = Y/D$ hole spacing increases. In addition, overall Nusselt number magnitudes generally decrease as $X/D = Y/D$ increases. An exception is evident in Fig. 9a for $Re_j = 8{,}000$, where the 5D hole spacing data are somewhat lower than the 8D hole spacing data. This is a result of cross-flow effects, which are more pronounced for lower Reynolds numbers and smaller values of $X/D = Y/D$. Also note that line-averaged Nusselt number values between peak values, near local minimum locations, often decease as $X/D = Y/D$ hole spacing increases.

3.6. *Spatially-averaged Nusselt numbers – effects of hole spacing, Reynolds number, and jet-to-target plate distance*

Figs. 10–13 present area-averaged Nusselt number variations for Re_j Reynolds number values of approximately 8,000, 20,000, 30,000, and 50,000, respectively. In each of these figures, spatially-averaged Nusselt numbers are given as they vary with x/D, hole spacing $X/D = Y/D$, and jet-to-target-plate distance Z/D. Each spatially-averaged value is determined over an area which extends over an x/D range from $-X/2D$ to $+X/2D$ relative to each streamwise row location, and over a y/D range comprised of one or two complete periods of local spanwise Nusselt number variation.

In general, the results in Figs. 10–13 show that area-averaged Nusselt numbers often increase at each x/D location as either the Reynolds number increases, or as the $X/D = Y/D$ hole spacing decreases. The highest spatially-averaged Nusselt numbers are generally present for $Z/D = 3.0$ for the three lowest Re_j values (as well as for $Z/D = 5.0$ when $Re_j = 8200$). When $Re_j = 52{,}000$, spatially-averaged Nusselt numbers in Figs. 10–13 show that the highest measured values are generally present for Z/D of either 1.5, 3.0, or 5.0, depending upon magnitudes of Re_j, X/D, Y/D, and streamwise location x/D.

Local increases of area-averaged Nusselt numbers from positive cross-flow influences are also evident in Figs. 10–13 for particular configurations and experimental conditions. Resulting variations are evident in Fig. 10 when $x/D \geq 25$–30, provided hole spacing is 5D, $Re_j = 8{,}000$, and Z/D is equal to either 1.5 or 3.0. Area-averaged Nusselt number increases from cross-flow effects are also evident for $Z/D = 1.5$ at larger x/D locations in Figs. 11 and 12, when $Re_j = 20{,}000$ and $Re_j = 30{,}000$, respectively.

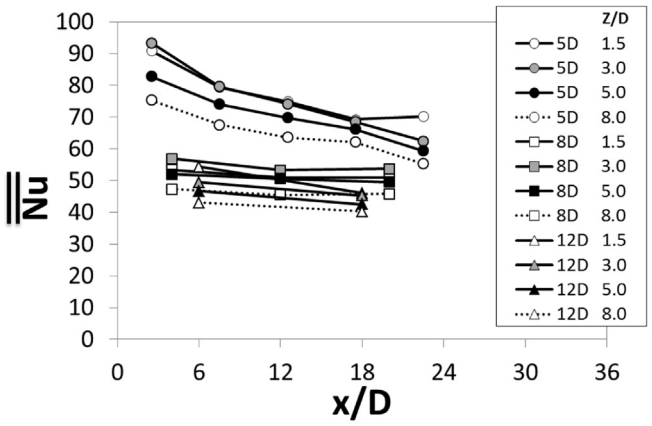

Fig. 11. Spatially-averaged Nusselt numbers for $Re_j \approx 20{,}000$ as dependent upon x/D, hole spacing, and Z/D value.

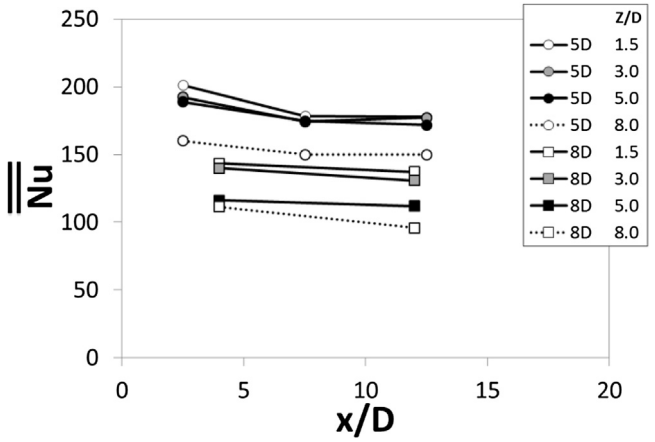

Fig. 13. Spatially-averaged Nusselt numbers for $Re_j \approx 50{,}000$ as dependent upon x/D, hole spacing, and Z/D value.

4. Summary and conclusion

Experimental results are presented which illustrate the effects of jet-to-target plate distance, hole array spacing, and Reynolds number on *cross-flow phenomena*, and associated surface heat transfer distributions, for an array of jets impinging on a flat plate. The array of impinging jets is directed to one flat surface of a channel which is bounded on three sides. Considered are jet Reynolds numbers ranging from 8000 to 50,000, jet-to-target plate distances of 1.5*D*, 3.0*D*, 5.0*D*, and 8.0*D*, and steamwise and spanwise hole spacing of 5*D*, 8*D*, and 12D. Associated Mach numbers are low enough to insure that little or no Mach number dependence is present. The present study is different from many other recent impingement array investigations [1–3,6–9] because a staggered hole array is utilized. Compared to other recent studies, which also employ staggered hole arrays [4,5], the present results are different because a wider range of Z/D values are employed, and because of the inclusion of high-accuracy, spatially-resolved, local Nusselt number distributions (along with line- and spatially-averaged results).

In general, the cumulative accumulations of cross-flows, from sequential rows of jets, result in sequentially decreasing periodic Nusselt number variations with streamwise development. Such behavior is a result of the bending and re-direction of the impingement jets by cross-flow, which also result in reduced coherence of the shear layers which form near and around each jet trajectory. When examined at a particular value of Re_j, streamwise locations of local maximum Nusselt numbers also shift to larger x/D locations as the normalized jet-to-target distance increases. This is a result of larger advection distances between the impingement hole exits and the target plate, which allow crossflows to exert greater influences in shifting the locations of jet impact stagnations points. In general, the observed Nusselt number decreases from cross-flow effects become more pronounced as the Reynolds number increases, and as hole spacing decreases.

However, for some situations, cross-flows can also result in local augmentation of Nusselt numbers. This occurs most often in channels at lower Reynolds numbers, where impingement jet fluid distributions are confined by smaller hole spacing, and smaller jet-to-target plate distance. Such behavior is evident in line-averaged and area-averaged Nusselt number distributions for 5*D* hole spacing, $Re_j = 8{,}000$, and Z/D of 1.5, 3.0, provided $x/D \geq 30$. Line- and area-averaged Nusselt number increases from cross-flow effects are also present at larger x/D locations when Re_j is 20,000, 30,000, and 50,000, and $Z/D = 1.5$. Such Nusselt number augmentations occur as interactions between impingement jets become more vigorous, and local magnitudes of mixing and turbulent transport are increased.

Acknowledgments

The research presented in this paper was sponsored by Solar Turbines Inc., located in San Diego, California.

References

[1] D.M. Kercher, W. Tabakoff, Heat transfer by a square array of round air jets impinging perpendicular to a flat surface including the effect of spent air, ASME Trans. J. Eng. Power 92 (1970) 73–82.
[2] D.E. Metzger, R. Korstad, Effects of crossflow on impingement heat transfer, ASME Trans. J. Eng. Power 94 (1972) 35–41.
[3] J.L. Chance, Experimental investigation of air impingement heat transfer under an array of round jets, TAPPI 57 (6) (1974) 108–112.
[4] D.E. Metzger, L.W. Florschuetz, D.I. Takeuchi, R.D. Behee, R.A. Berry, Heat transfer characteristics for inline and staggered arrays of circular jets with crossflow of spent air, ASME Trans. J. Heat Transfer 101 (1979) 526–531.
[5] L.W. Florschuetz, C.R. Truman, D.E. Metzger, Streamwise flow and heat transfer distributions for jet array impingement with crossflow, ASME Trans. J. Heat Transfer 103 (1981) 337–342.
[6] N.T. Obot, T.A. Trabold, Impingement heat transfer within arrays of circular jets: part 1-effects of minimum, intermediate, and complete crossflow for small and large spacings, ASME Trans. J. Heat Transfer 109 (1987) 872–879.
[7] J.Y. San, Y.M. Tsou, Z.C. Chen, Impingement heat transfer of staggered arrays of air jets confined in a channel, Int. J. Heat Mass Transfer 50 (19–20) (2007) 3718–3727.
[8] J.M. Miao, C.Y. Wu, P.H. Chen, Numerical investigation of confined multiple-jet impingement cooling over a flat plat at different crossflow orientations, Numer. Heat Transfer Part A Int. J. Comput. Methodol. 55 (11) (2009) 1019–1050.
[9] K. Vadiraj, S.V. Prabhu, Influence of spanwise pitch on local heat transfer distribution for in-line arrays of circular jets with spent air flow in two opposite directions, Exp. Therm. Fluid Sci. 33 (2008) 84–95.
[10] J. Park, M. Goodro, P.M. Ligrani, M. Fox, H.-K. Moon, Separate effects of mach number and Reynolds number on jet array impingement heat transfer, ASME Trans. J. Turbomach. 129 (2) (2007) 269–280.
[11] M. Goodro, P.M. Ligrani, M. Fox, H.-K. Moon, Mach number, Reynolds number, jet spacing variations: full array of impinging jets, AIAA J. Thermophys. Heat Transfer 24 (1) (2010) 133–144.
[12] S.J. Kline, F.A. McClintock, Describing uncertainties in single sample experiments, Mech. Eng. 75 (1953) 3–8.
[13] R.J. Moffat, Describing the uncertainties in experimental results, Exp. Therm. Fluid Sci. 1 (1) (1988) 3–17.
[14] J. Lee, Z. Ren, P.M. Ligrani, M.D. Fox, H.K. Moon, Crossflows from jet array impingement cooling: effects of hole array spacing, jet-to-target plate distance, and Reynolds number, Paper Number GT2014-26426, ASME TURBO EXPO 2014 – 59th TURBO EXPO Turbine Technical Conference and Exposition, Dusseldorf, Germany, June 16–20, 2014.
[15] M.D. Fox, M. Kurosaka, L. Hedges, K. Hirano, The influence of vortical structures on the thermal fields of jets, J. Fluid Mech. 255 (1993) 447–472.
[16] C.O. Popiel, O. Trass, Visualization of a free and impinging round jet, Exp. Therm. Fluid Sci. 4 (1992) 106–115.
[17] M. Angioletti, R.M. Di Tommaso, E. Nino, G. Ruocco, Simultaneous visualization of flow field and evaluation of local heat transfer by transitional impinging jets, Int. J. Heat Mass Transfer 46 (2003) 1703–1713.
[18] T.S. O'Donovan, D.B. Murray, Jet impingement heat transfer – part II: a temporal investigation of heat transfer and local fluid velocities, Int. J. Heat Mass Transfer 50 (2007) 3302–3314.

CHAPTER 4

IMPINGEMENT ARRAY HEAT TRANSFER WITH LARGE HOLE SPACING

This chapter is a paper accepted by JP Journal of Heat and Mass Transfer, 2015. Authors are Z. Ren, J. Lee, P. M. Ligrani, D. H. Lee, M. D. Fox, and H.-K. Moon.

JP Journal of Heat and Mass Transfer

http://dx.doi.org/10.17654/
Volume …, Number …, 2015, Pages … **ISSN: 0973-5763**

IMPINGEMENT ARRAY HEAT TRANSFER WITH LARGE HOLE SPACING

Zhong Ren[a], Junsik Lee[b], Phil Ligrani[c*], Dae Hee Leed Michael D. Foxe and Hee-Koo Moone

[a,c]Propulsion Research Center
Department of Mechanical and Aerospace Engineering
College of Engineering
University of Alabama in Huntsville
Technology Boulevard, Olin B. King Technology Hall S236
Huntsville, AL 35899, U. S. A.
e-mail: pml0006@uah.edu

[b]Korea Institute of Energy Research
152, Gajeong-ro, Yuseong-gu, Deajeon, 305-343, Korea

[d]Department of Mechanical and Automotive Engineering
High Safety Vehicle Core Technology Research Center
Inje University
197 Inje-ro, Gimhae, Gyeongnam, 621-749, Korea

[e]Aero/Thermal & Heat Transfer, Solar Turbines, Inc.
2200 Pacific Highway, P. O. Box 85376, Mail Zone C-9
San Diego, California 92186-5376, U. S. A.

Abstract

Data are presented which illustrate surface heat transfer characteristics

Received: September 1, 2015; Accepted: October 15, 2015
Keywords and phrases: Impinging Jet, Impingement Jet Array Cooling, Jet-to-Target Plate Distance, Nusselt Number, Jet Hole Spacing, Heat Transfer Augmentation.
[*]Corresponding author

of an array of impinging jets with large hole spacing on a flat plate. Included is consideration of the effects of jet-to-target plate distance, and jet Reynolds number. Steamwise and spanwise hole spacing is 12*D*. Jet-to-target plate distances *Z* of 1.5*D*, 3.0*D*, 5.0*D*, and 8.0*D* are employed, where D is the impingement hole diameter. Reynolds numbers Re_j range from 8,000 to 50,000, with isentropic jet Mach numbers of approximately 0.1 to 0.2. Experimental results include local, line-averaged, and spatially-averaged Nusselt number distributions. These different types of Nusselt numbers increase strongly with impingement jet Reynolds number for all situations examined. This dependence of spatially-averaged Nusselt number is quantified using a correlation for the two most upstream rows of impingement jets (at the smallest x/D values), where cross flows and jet interactions are minimal. The highest local Nusselt numbers are generally present for $Z/D = 3.0$ for Re_j of 20,000, 30,000, and 50,000, with local Nu number decreases as Z/D increases further. For Re_j of 8,000, the highest Nusselt number values are generally present for $Z/D = 5.0$. In general, using $X/D = Y/D = 12$, the influences of surrounding jets, including cumulative-induced crossflows and interactions of jet-induced vortex structures, are less pronounced, relative to configuration with smaller hole spacing. With the present large hole spacing, both local and line-averaged maximum Nusselt number data trends show only very small variations with increasing x/D. As such, important differences relative to impingement arrays with smaller hole spacing are evident, especially in regard to Nusselt number variations as streamwise location, jet-to-target plate distance, and Reynolds number are changed.

Nomenclature

A_{ht}	heat transfer area on the target plate $[\mathrm{m}^2]$
D	diameter of an individual impingement hole $[\mathrm{m}]$
h_{loss}	loss h heat transfer coefficient to account for convection and radiation loss from back side of target plate $[\mathrm{W/m.k}]$

k ratio of specific heats

M_a impingement air flow Mach number

Nu local Nusselt number

$\overline{Nu}$ line-averaged Nusselt number

$\overline{\overline{Nu}}$ spatially-averaged Nusselt number

Q total power provided to the thermofoil heater $[\mathrm{W}]$

q_{cb} convection heat flux from back side of the target plate $[\mathrm{W/m^2}]$

q_{cf} convection heat flux from front side (or impingement side) of the target plate $[\mathrm{W/m^2}]$

q_{rb} radiation heat flux from back side of the target plate $[\mathrm{W/m^2}]$

q_{rf} radiation heat flux from front side (or impingement side) of the target plate $[\mathrm{W/m^2}]$

Re_j impingement air flow Reynolds number

$T_{ambient}$ ambient static temperature [K]

T_b local temperature on the back surface of the polystyrene target plate [K]

T_j impingement air static temperature [K]

T_{oj} impingement air stagnation temperature [K]

T_W local target surface temperature on the surface of the [K]

heater adjacent impingement air

u_a impingement air velocity $[\mathrm{m/s}]$

x streamwise coordinate [m]

X streamwise distance between centerlines of adjacent

	impingement holes [m]
y	spanwise coordinate [m]
Y	spanwise distance between centerlines of adjacent impingement holes [m]
z	normal coordinate [m]
Z	distance between target plate and impingement hole plate [m]

Greek Symbols

α	air thermal conductivity $[\mathrm{W/m^2 \cdot K}]$
εf	emissivity of the front surface of the target plate
$\varepsilon \inf$	emissivity of a plate located opposite to the target plate
μ	absolute viscosity $[\mathrm{kg/m \cdot s}]$
ρ_a	impingement air static density $[\mathrm{kg/m^3}]$
σ	Boltzman constant

1. Introduction

Considered are surface heat transfer variations for impingement arrays with large hole spacing in the streamwise and spanwise directions. Of particular interest are the influences of streamwise development, jet Reynolds number, and jet-to-target plate distance. Ordinarily, such impingement arrangements are employed for cooling leading edge regions of turbine blades and vanes [1], and for cooling parts of the combustor in gas turbine engines, including combustion chamber liners, transition pieces, and splash plates [2].

Other studies which consider impingement array cooling with large hole spacing with low speed, incompressible flows, include Kercher and Tabakoff [3], who present spatially-averaged surface heat transfer coefficients beneath an array of impinging jets in low-speed flow for Reynolds numbers from

3×10^2 to 3×10^4, X/D and Y/D from 3.1 to 12.5, and Z/D from 1.0 to 4.8. Another investigation by Metzger and Korstad [4] considers target spacing and the influences of cross-flow on a single line of jets, emerging from circular holes, placed on one wall of a channel. They show that target spacing, jet Reynolds number, and the relative strengths of the jet flow and the cross flow influence heat transfer on the target wall. Z/D target distance effects are also addressed by Chance [5], who also investigates low-speed impingement cooling with spent air constrained to flow out only one side of the flow passage. Also addressed in this investigation are data at Reynolds numbers from 6×10^3 to 5×10^4, square, equilateral triangle, and rectangular jet arrays, Z/D values of 2, 3, 4, 6, and 8, and ratios of impingement to surface absolute temperature of 0.77, 1.27, and 1.54.

Two other widely cited investigations are described by Metzger et al. [6] and Florschuetz et al. [7]. In the first of these, Metzger et al. [6] indicate that in-line jet impingement hole patterns provide better heat transfer than staggered arrangements. Investigated are Z/D values of 1, 2, and 3, X/D and Y/D ranging from 6 to 32, and Reynolds numbers from 5×10^3 to 2×10^4. Florschuetz et al. [7] describe an investigation, wherein Reynolds numbers from 2.5×10^3 to 7×10^4, inline and staggered hole patterns, Z/D from 1 to 3, X/D from 5 to 15, and Y/D from 4 to 8 are considered. As for the investigation of Metzger and Korstad [4], impinging air is again constrained to exit in a single direction from the channel formed between the impingement plate and the target plate. Included are data on channel cross flow mass velocity and jet mass velocity (where ratios range from 0 to 0.8), as well as a correlation which gives Nusselt number dependence on these parameters, as well as on jet impingement plate geometry, Prandtl number, and Reynolds number.

Large hole spacing arrangements are also considered by Obot and Trabold [8], who consider different cross-flow schemes on impingement heat transfer in low-speed flows. Impingement jet Reynolds numbers from

1×10^3 to 2.1×10^4, Z/D values from 2 to 16, X/D values of 5 and 10, and Y/D values of 4 and 8 are employed. According to these investigators, for a given cross flow scheme and constant jet diameter *D*, higher heat transfer coefficients are obtained as the number of jets over a fixed target area increases. Jet plate-to-target spacings from 1.25 to 5.5 impingement hole diameters are considered by Bailey and Bunker [9], who spacings of 3, 6, and 9 are considered. Reynolds numbers range from 1.4×10^4 to 6.5×10^4, with Mach numbers that are relatively low. Included are correlations developed from these data which extend the range of applicability of the correlations presented by Florschuetz et al. [7]. They also show that, for sparse impingement arrays, each jet generally behaves independently.

The present study provides new impingement heat transfer data to illustrate the effects of varying jet-to-target plate distance, streamwise development, and Reynolds number, with nondimensional streamwise and spanwise hole spacings X/D and Y/D of 12. The thickness of each impingement plate is 1*D*, and spacings between the hole exit planes and the target plate are 1.5*D*, 3.0*D*, 5.0*D*, and 8.0*D*. Included are local, line-averaged, and spatially-averaged Nusselt numbers. Impingement jet Reynolds numbers range from 8,000 to 50,000, with Mach numbers of approximately 0.1 to 0.2. As such, the results from the present investigation are unique and different from data given in other recent studies because the flow conditions and configurations employed are new. The present study is also different from many other impingement array investigations [3-5, 8-12] because a staggered hole array is utilized with large hole spacing. Compared to other studies, which also employ staggered hole arrays [6,7], the present results are different because a wider range of Z/D values are employed, and because of the inclusion of high-accuracy, spatially-resolved, local Nusselt number distributions (along with line- and spatially-averaged results).

2. Experimental Apparatus and Procedures

2.1. Impingement plate, and impingement flow facility

Figure 1 shows a schematic diagram of the impingement flow facility. Figure 2 shows that individual plates with holes are located at the bottom of the lower plenum, which are used to produce the impingement jets. Different impingement plates can be installed at this location. Each impingement plate consists of 7 rows of holes in the streamwise direction, arranged so that holes in adjacent rows are staggered with respect to each other, as shown in Figure 3. With this arrangement, either 4 or 5 holes are located in each streamwise row. The thickness of each impingement plate is 1D. The spacing between holes in the streamwise direction X is 12D, and the spacing between holes in the spanwise direction Y is 12D. Z/D is the spacing between the hole exit planes and the target plate, with values employed in the present investigation of 1.5, 3.0, 5.0, and 8.0. Figure 3 also shows the coordinate systems employed. Channel formed by the target surface and the impingement jet plate contains the impingement cooling flow. Within the channel, the impingement cooling flow is constrained to exit in a single direction, which here, is denoted as the x-direction. This channel is called the impingement plenum or lower plenum. The impingement plenum consists of a volume of air between the target and jet impingement plate. In the present study, impingement jet Reynolds numbers of approximately 8,000, 20,000, 30,000, and 50,000 are employed. Impingement jet Mach numbers are approximately 0.1 to 0.2, and are selected because previous investigations show that Nusselt numbers generally show no dependence on Mach number, when values are less than approximately 0.25.

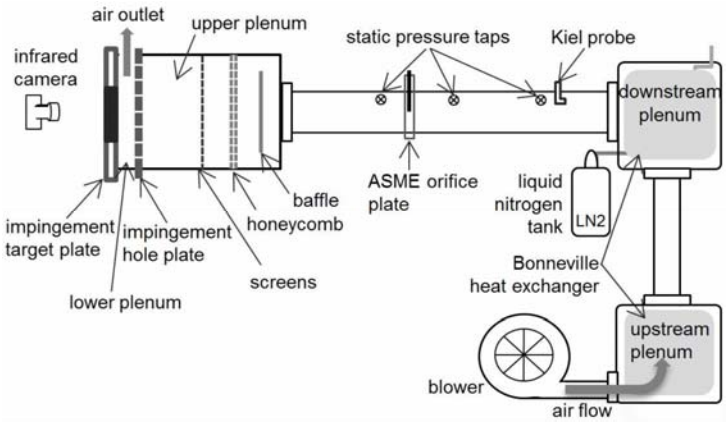

Figure 1. Impingement flow facility.

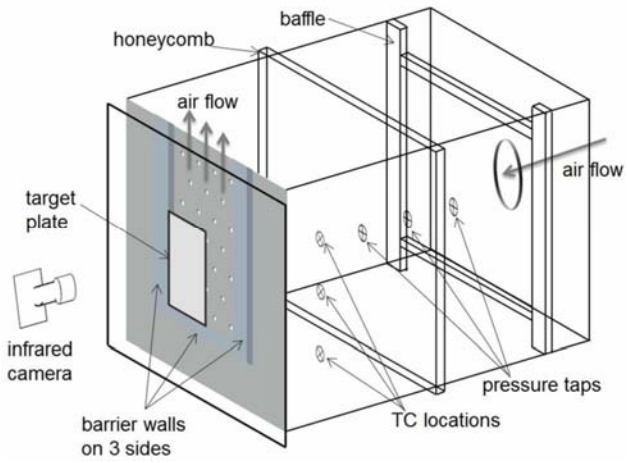

Figure 2. Impingement flow facility test section, including impingement plenum, and impingement channel.

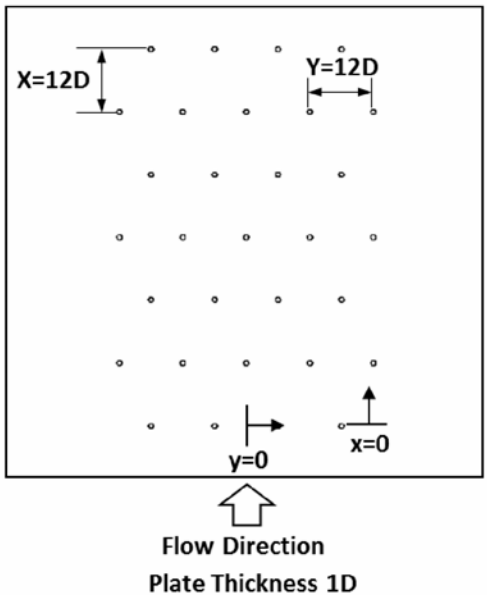

Figure 3. Impingement test plate configuration for $X/D = Y/D = 12$.

The laboratory facility used for heat transfer measurements, shown in Figure 1, is constructed of A53 Grade *B* ARW steel piping, and 6.1 mm thick ASTM A38 steel plates. The two plenums which are arranged in series are located downstream of the blower. The upstream plenum is 0.63 *m* in length along each side. The downstream plenum dimensions are 0.63 *m* long, 0.77 *m* tall and 0.77 *m* wide. Within each plenum, a Bonneville cross-flow heat exchanger is employed. As the air exits the heat exchanger, and the second plenum, the air passes into a pipe with 0.22 m outer diameter. The ASME Standard orifice plate is located within the pipe to measure the air mass flow rate. This pipe then connects to a third plenum, with side dimensions of 0.635 m and 0.635 *m*. Honeycomb and other flow straightening devices are employed for the air which enters this plenum. The upper impingement plenum (or upper plenum) is located below the honeycomb and flow straightening devices, as shown in Figure 2. The dimensions of the upper impingement plenum are 0.635 *m* and 0.635 *m*, with a height of 0.40 *m*.

The air stream through the plenums and channel is drawn from the

laboratory atmosphere. A New York Blower Co. 7.5 HP, size 1808 pressure blower is employed to induce flow within the facility. An ASME standard orifice plate, flow-mounted calibrated copperconstantan thermocouples, and pressure transducers are used for measuring the air mass flow rate provided to the impingement hole array. Pressure transducers are Validyne DP15-22 and DP15-32 (with diaphragms rated either at 1.40 or 14.0 kPa), and are connected to Validyne Model CD15 Carrier Demodulators. Gas static temperature is determined from thermocouple measurement of gas recovery temperature, and local velocity magnitude, which is determined from local values of static pressure and stagnation pressure.

2.2. Target plate test surfaces for measurements of surface Nusselt numbers.

Local surface Nusselt number are measured on a heated polystyrene target plate, with a size of 126 mm by 254 mm by 1.31 mm. Polystyrene is chosen for the target plate because of its strength, and because it does not deform in shape at temperatures as high as 8 °C. It is also suitable because of its relatively low thermal conductivity (0.09 W/mK at 2 °C), which results in minimal streamwise and spanwise conduction along the test surface. The target plate is mounted on the bottom surface of the impingement plenum (or lower plenum). This is accomplished using gray cloth tape with PVC cement, a solvent containing acetone, tetrahydrofuran, and methyl-ethyl-ketone to seal the edges so that no leaks are present along the flow passage. A mounting frame is also employed to hold the polystyrene target plate in place, to keep it smooth (without wrinkles or bending), and normal to the impingement jets, as testing is underway. Within the polystyrene target plate, eight calibrated type-*T* copperconstantan thermocouples are placed at different streamwise and spanwise locations so that each senses a different temperature as data are acquired. These thermocouples are mounted approximately 0.016 cm below the surface adjacent to the air containing the impingement fluid. Local surface temperatures are determined, after correction for thermal contact resistance and temperature drop through the 0.016 cm thickness of polystyrene. Thermocouple lead wires are placed in

grooves along the polystyrene, and bonded into place with epoxy, which has approximately the same thermal conductivity as polystyrene, to minimize thermal disturbances resulting from their presence. Each one of these thermocouple wires is then located between the polystyrene portion of the target plate and the thermofoil heater.

Spatially-resolved distributions of surface Nusselt number and heat transfer coefficients are measured on the polystyrene target plates with thermocouples and heater attached. Each custom-made HK5184R26 thermofoil heater has a maximum temperature rating of 100 °C, and is manufactured by Minco Products Inc. The etched-foil heating element within this device is encased between two layers of DuPont Kapton polyimide film, and is used to provide a constant surface heat flux boundary condition. This heater is located adjacent to the air stream with the impinging air. Its thermal conductivity is approximately 0.2 W/mK at 20°C. Spatially-resolved measurements of surface temperature are obtained by the infrared camera viewing the back side of polystyrene target plate. The total target plate thickness is 1.60 mm (each heater is approximately 0.3 mm thick and each polystyrene target plate is 1.3 mm thick). These target plate are replaced with all new components after each 3 or 4 test sequences because of the wear and degradation which results from exposure to different temperature levels as tests are conducted.

2.3. Local impingement air pressure and temperature measurements.

As shown in Figure 2, two wall pressure taps are located on the surface of the lower plenum, and three wall static pressure taps are also located on the surface of the upper plenum to measure local static pressures. As tests are conducted, calibrated Validyne Model DP15-22 and DP15-32 pressure transducers driven by Validyne Model CD15 Carrier Demodulators are used to sense pressures from these static pressure taps. Local airflow recovery temperatures are measured using a total of five calibrated Omega *T*-type copper-constantan thermocouples. Two of these are located in the central part of the lower plenum, and the other three are located in the central part of the upper plenum. These thermocouples are calibrated using a Omega Model

HCTB-3020 constant temperature water bath, a Fluke Hart 1523 Thermometer and stainless steel sheathed thermistor (which is accurate within ± 0.01 °C). In each test case, average temperature and pressure values for a given plenum are obtained using readings from either multiple thermocouples or multiple pressure taps. Voltages from all the thermocouples and the Carrier Demodulators are read sequentially using National Instruments NI-USB 9162 and NI-USB 6210 Data Acquisition terminals, respectively. A Dell Precision T3500 computer is used to relay information from these terminals. Thermocouple compensation is provided electronically by this system, such that voltages for copper-constantan thermocouples are given relative to 0°C. The voltage outputs from this unit are acquired by the computer through its USB port, using LABVIEW 10.0 software.

The Mach number and velocity of the air in the plenum are both near zero, because the cross-sectional area of the upper plenum is very large compared to the area of the impingement holes. As a result, the stagnation pressure is the same as the static pressure measured at the wall static pressure taps. The resulting value is denoted P_{oj}, the impingement air stagnation pressure. The measured air recovery temperature in the upper plenum is then the same as the upper plenum stagnation temperature and upper plenum static temperature. and is denote T_{oj}, the impingement stagnation temperature. The impingement air mass flux is determined using $\rho_a u_a = \dot{m}/A$, after measurement of the impingement air mass flow rate at the pipe orifice plate.

The impingement flow Mach number M_a, and the impingement static temperature T_j are both determined by using an iterative procedure. Firstly, the local recovery temperature, which is measured in the lower plenum, is used for this estimation of the value of T_j. The spatially-averaged impingement jet velocity and impingement static density are then determined using $u_a = \dot{m}/\rho_a A$, and $\rho_a = P_a/RT_j$, respectively. Next, the local atmospheric pressure is used for P_a, because the impingement flow vents to the laboratory. Measurements of lower plenum static pressures using wall

pressure taps confirm this approach. In addition, Mach number and the impingement air sonic velocity are given by $M_a = u_a/c_a$, and $c_a = (kRT_j)^{1/2}$, respectively. Iterations using these analysis steps are then continued until impingement Mach number and the impingement static temperature are consistent with the isentropic equation given by

$$T_j = T_{oj}/[1 + M_a^2\,(k-1)/2]. \tag{1}$$

With impingement flow Mach number M_a, impingement static temperature T_j, and other parameters known, the impingement Reynolds number is subsequently given by an equation of the form

$$\mathrm{Re}_j = \rho_a u_a D/\mu. \tag{2}$$

A Kiel-type stagnation pressure probe is used to measure the total pressure. The probe in the pipe is located upstream of the orifice plate employed to measure mass flow rate. A calibrated copper-constantan thermocouple, and a wall pressure tap located on the surface of the pipe within the air stream are used to sense flow recovery temperature and static pressure, respectively, at the same streamwise location. Temperatures and pressures measured using the thermocouple, probe, and tap are sensed and processed using the same types of instrumentation mentioned earlier. The ASME standard orifice plate is employed for measurement of pipe average velocity, deduced from mass flow rate, and is used to provide a cross-check on the velocities deduced from this arrangement.

2.4. Local Nusselt number measurement.

A Price-Rutzebeck POW-R-PAC 160V transformer power supply is employed to power the thermofoil heater with a direct current supply. The power supply is directed using a covered switchboard where amperage is read by both a Simpson 260 Series 8P Ammeter and an Agilent 34401A Digit Benchtop Multimeter. The voltage is measured using a Fluke 8846A 6.5 Digit Precision Multimeter. For a particular test, energy balances, and analysis to determine temperature values on the two surfaces of the target

plate, then allow determination of the magnitude of the total convective power (due to impingement cooling). To determine the surface heat flux (used to local Nusselt numbers and calculate heat transfer coefficients), the total convective power level, provided by a thermofoil heater, is divided by the single surface area of this heater, denoted A_{ht}.

To determine T_b, the local temperature on the back surface of the polystyrene target plate, adjacent to the surrounding ambient air environment, one-dimensional conduction analysis is utilized. This analysis is applied to a control volume located between the ambient air environment behind the target plate and the surface within the target plate (where the thermocouples are located between the heater and the polystyrene target plate). The local temperature within the target plate between the polystyrene plate the thermofoil heater, measured by each of these thermocouples, is then T_{tc}. Associated temperatures are required to determine radiation losses, and heat flux from the back side of the target plate, q_{cb} and q_{rb}, respectively. Utilized for this purpose is an equation of the form

$$q_{rb} + q_{cb} = h_{loss}(T_b - T_{ambi}\varepsilon), \tag{3}$$

where h_{loss} is assumed to be equal to 15 W/m^2K [13]. The radiation heat flux q_{rf} on the front (or impingement side) of the target plate is determined using

$$q_{rf} = \sigma(1/\varepsilon_{\inf} - 1/\varepsilon_f - 1)^{-1}(T_W^4 - T_{ambie}^4). \tag{4}$$

With this approach, the radiation heat flux is determined for an arrangement with multireflection between two infinite plates where each has a uniform temperature. For all conditions investigated, ε_f and $\varepsilon\inf$ are assumed to be equal to 0.9. Because $q_{rf}A_{ht}$ is generally only 3-6 percent of Q, the total amount of power provided to the thermofoil heater, this approximate approach is appropriate.

To determine q_{rf}, T_W, the local target surface temperature on the

surface of the heater adjacent impingement air, is required. An iterative procedure is utilized because of the interdependence of T_W, q_{rf}, and q_{cf}. Here, q_{cf} is the convection heat flux from the front side or impingement side of the target plate. A one-dimensional conduction model is also used for the heater, which includes source generation of thermal energy, to provide a relation between T_W, T_{tc}, and q_{cf}. Included within this analysis is thermal contact resistance between the adjacent heater and the internal thermocouples. This one-dimensional conduction approach is employed since magnitudes of lateral conduction within the target plate are very small and mostly insignificant (from three-dimensional analyses), relative to impingement convective heat flux levels.

The convection heat flux from the front side (or impingement side) of the target plate is then given by

$$q_{cf} = Q/A_{ht} - q_{rf} - q_{rb} - q_{cb}. \tag{5}$$

The local Nusselt number is then given as

$$Nu = q_{cf}D/((T_W - T_{0j})\alpha). \tag{6}$$

Spatially-resolved distributions of the target test surface temperature T_W are determined as impingement heat transfer measurements are made. This procedure is achieved by using infrared imaging in conjunction with thermocouples, energy balances, digital image processing, and in situ calibration procedures. Spatially-resolved surface Nusselt numbers are then determined.

To accomplish this, an ImagIR InSB Digital 320×256 infrared camera is employed to capture the infrared radiation emitted by the heated interior surface of the channel. This camera operator at infrared wavelengths from 5.2 μm to 9.1 μm. The calibrated, copper-constantan thermocouples, which are distributed within the test surface, are used to perform the in situ calibrations simultaneously as the radiation contours from surface temperature variations are recorded. As shown in Figure 2, this is

accomplished as the camera views the test surface from behind. In general, all eight thermocouple junction locations are present in the infrared field viewed by the camera. Prior to measurements, calibration maps are used to provide a relationship between the exact pixel locations, the spatial locations of thermocouple junctions, and the coordinates associated with each infrared image. During this procedure, the camera is rigidly mounted, and focused and oriented relative to the test surface in the same way as when radiation contours are recorded. Such calibration data depend strongly on camera adjustment. The same contrast, brightness and aperture camera settings are used to obtain the experimental data. The in situ calibration approach accurately and rigorously accounts for these variations.

Images from the infrared camera are recorded as 8-bit gray scale. These images are directly into the memory of a Dell Precision T3500 computer using the infrared camera interface program, WINIR, and a Matrox Frame grabber video card. One set of 50 frames is taken in ten frames sets at five random intervals. The final gray scale data image is then obtained by averaging all of the resulting images. MATLAB software is employed to convert each of 256 possible gray scale values to local Nusselt number at each pixel location using calibration data. Each individual infrared image covers a 256 pixel by 320 pixel area.

2.5. Experimental uncertainty estimates.

Uncertainty estimates are based on 95 percent confidence levels and are determined using methods described by Kline and McClintock [14] and Moffat [15]. Uncertainty of temperatures for measurement of thermocouples is ± 0.15 °C. Spatial and temperature resolutions achieved with infrared imaging are about 0.1 mm to 0.2 mm, and 0.4 °C, respectively. This magnitude of temperature resolution is a result of uncertainty in determining the exact locations of thermocouples with respect to pixel values used for the in situ calibrations. Among the different quantities considered, the uncertainty associated with temperature makes the largest contribution to overall Nusselt number uncertainty. Possible lateral conduction within the test plates is also considered to the overall Nusselt number uncertainty. In

general, magnitudes of lateral conduction (in the x and y directions) are generally insignificant relative to overall convective heat flux levels from impingement. Table 1 shows that the total local Nusselt number uncertainty is approximately ± 6.0 percent. This uncertainty magnitude represents the maximum value which is encountered for all test conditions within the present investigation.

Table 1. Experimental uncertainty percentage magnitudes for the local Nusselt number, and quantities employed to determine the local Nusselt number.

Quantity	Experimental Uncertainty (Percent)
A_{ht}	1.394
D	4.919
T_w	2.706
T_{oj}	0.722
α	0.541
Nu	6.043

3. Experimental Results

The impingement test plate configurations and the experimental test conditions of the present investigation are presented in Table 2.

Table 2. Impingement test plate configurations and experimental test conditions for $X/D = Y/D = 12$.

Re_j	Ma	Z/D	Hole Diameter (mm)	Plate Thickness (mm)	Hole Spacing (mm)
8,000	0.14	1.5	3.5	3.5	42

8,000	0.13	3.0	3.5	3.5	42
8,000	0.13	5.0	3.5	3.5	42
8,000	0.13	8.0	3.5	3.5	42
20,000	0.13	1.5	8.0	8.0	96
20,000	0.14	3.0	8.0	8.0	96
20,000	0.14	5.0	8.0	8.0	96
20,000	0.13	8.0	8.0	8.0	96
30,000	0.21	1.5	8.0	8.0	96
30,000	0.21	3.0	8.0	8.0	96
30,000	0.21	5.0	8.0	8.0	96
30,000	0.21	8.0	8.0	8.0	96
50,000	0.21	1.5	15.0	15.0	180
50,000	0.20	3.0	15.0	15.0	180
50,000	0.20	5.0	15.0	15.0	180
50,000	0.20	8.0	15.0	15.0	180

3.1. Spatially resolved local Nusselt numbers.

Spatially resolved surface Nusselt number distributions are presented in Figure 4 for the jet hole spacing of 12*D*. These data are provided for an impingement jet Reynolds number *Rej* of approximately 30,000. According to Table 2, associated Mach numbers Ma are approximately between 0.140 and 0.20. Since these values are less than 0.25, little or no Mach number dependence is expected [16]. The different views of the test surface in Figure 4 are due to different infrared camera views of the target plate, as the same impingement plate with different jet-to-target plate distance are employed. Note that, regardless of Reynolds number and Mach number, that the qualitative distributions of local Nusselt numbers produced by each impingement jet are similar, with good periodic repeatability in the spanwise

direction for each streamwise row of impact locations. Local maximum *Nu* values are spaced approximately 12D apart in the streamwise direction, as a result of the impacts of different impingement jets onto the target surface. However, regardless of the value of Z/D, magnitudes of successive local peak Nusselt numbers, at successive jet stagnation point impact locations, are approximately invariant with increasing x/D. Note that the highest local Nusselt numbers in Figure 4 for $X/D = Y/D = 12$ appear to be associated with $Z/D = 5.0$ and $Z/D = 3.0$. Local Nusselt number decreases with increasing Z/D are due to jet flow turning as cross flows accumulate with additional streamwise development. This leads to diminished jet coherence, as well as diminished coherence of associated Kelvin-Helmholtz generated vortices, which occur as jet advection distances become larger. Such variations are connected to the intensity of the cross-flows which develop within the impingement passage. Such cross flows generally decrease as the hole spacing becomes larger and the hole spacing arrangements are less dense.

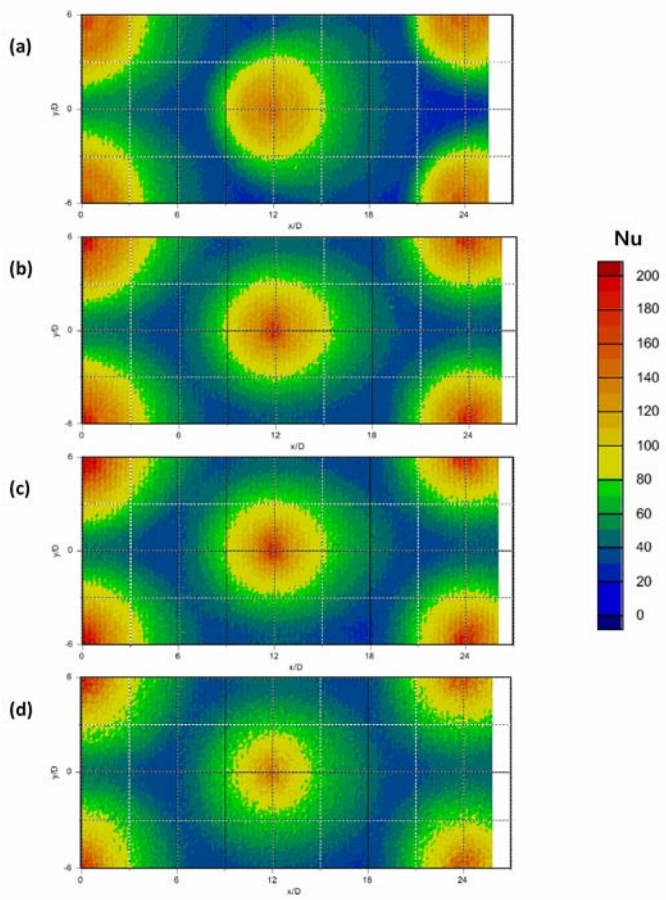

Figure 4. Local Nusselt number variations for $\mathrm{Re}_j \approx 30,000$ for different Z/D values and $X/D = Y/D = 12$. (a) $Z/D = 1.5$. (b) $Z/D = 3.0$. (c) $Z/D = 5.0$. (d) $Z/D = 8.0$.

Figures 5, 6, and 7 present local Nusselt number distributions for hole spacing $X/D = Y/D$ of 12D, for impingement Reynolds numbers of approximately 8,000, 30,000, and 50,000, respectively. These results are given for normalized jet-to-target plate distances Z/D of 1.5, 3.0, 5.0, and 8.0. Each set of local Nusselt number data are presented as dependent upon y/D for particular values of x/D, and as dependent upon x/D for particular values of y/D.

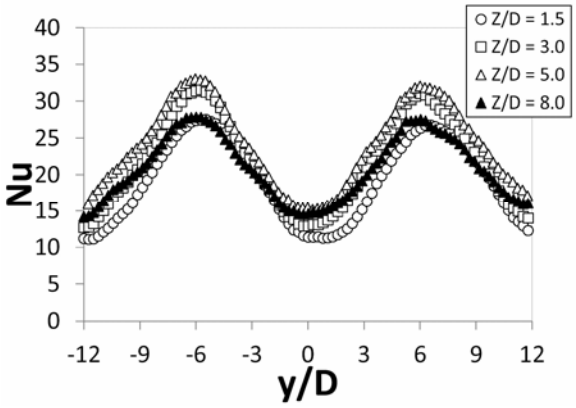

(a)

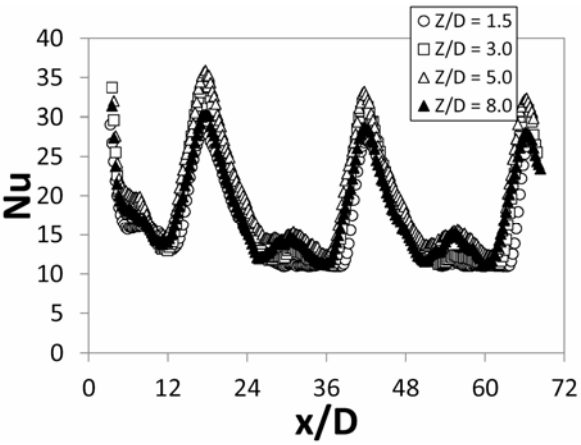

(b)

Figure 5. Local Nusselt number variations for $\mathrm{Re}_j \approx 8,000$ for different Z/D values and $X/D = Y/D = 12$. (a) Variations with y/D at $x/D = 30$ (b) Variations with x/D at $y/D = 0$

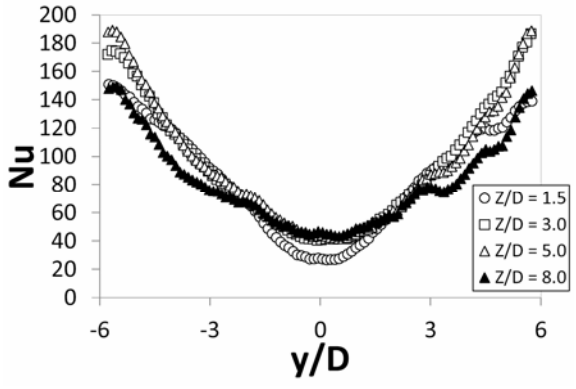

(a)

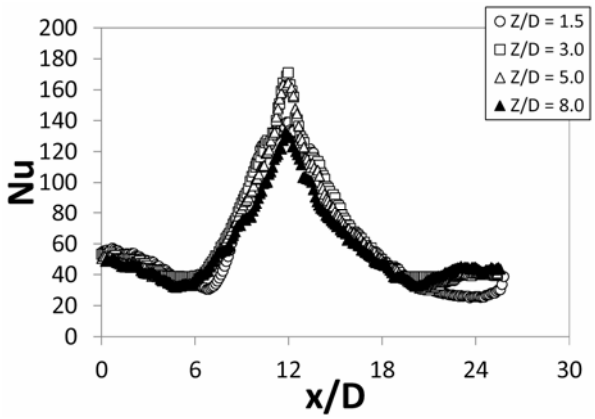

(b)

Figure 6. Local Nusselt number variations for $\mathrm{Re}_j \approx 30,000$ for different Z/D values and $X/D = Y/D = 12$. (a) Variations with y/D at $x/D = 24$ (b) Variations with x/D at $y/D = 0$

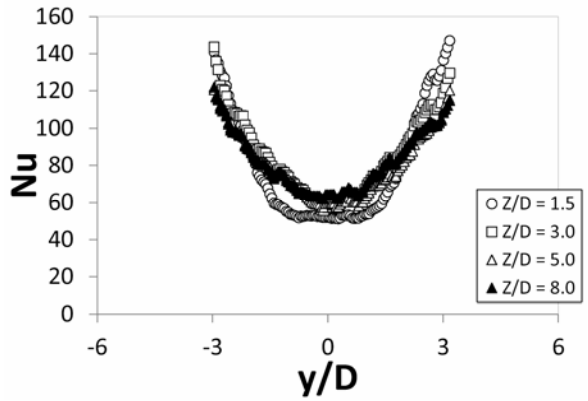

(a)

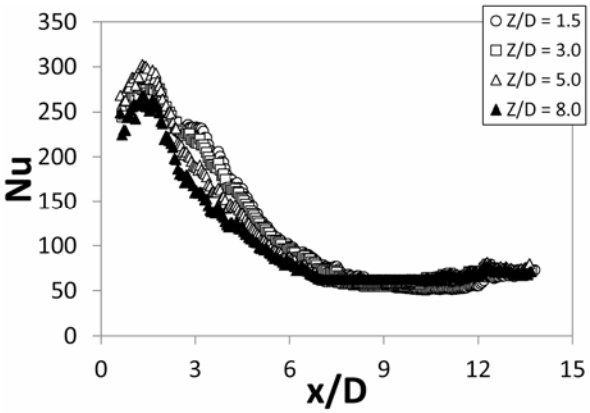

(b)

Figure 7. Local Nusselt number variations for $\mathrm{Re}_j \approx 50,000$ for different Z/D values and $X/D = Y/D = 12$. (a) Variations with y/D at $x/D = 10$ (b) Variations with x/D at $y/D = 0$

Figure 5a, 6a, 7a show local Nusselt number variations with y/D for $x/D = 30$, $x/D = 24$, $x/D = 10$, respectively. Here, local peak values are located near $y/D = -6$ and $y/D = +6$ underneath impinging jet impact locations. Figure 5b, 6b, 7b shows local Nusselt number variations with x/D for $y/D = 0$. Here, local maximum values are apparent, which are due to the

impact of impingement jets from each different streamwise row of hole. Figures 5, 6, and 7 additionally present that the highest local maximum Nusselt numbers are generally associated with Z/D of 5.0 (when $\mathrm{Re}\, j \approx 30,000$ and $\mathrm{Re}\, j \approx 50,000$). For all conditions examined, lower local values are generally occur both at and between jet impact locations as Z/D approaches 8.0, when compared at the same $\mathrm{Re}\, j$, x/D, and y/D. Associated overall local Nusselt number increases with decreasing Z/D (for large Z/D values) are generally believed to be due to enlarged jet coherence, as well as increased coherence of associated Kelvin-Helmholtz vortices.

Other recent investigations of Kelvin-Helmholtz vortex structures from impingement jets are described by Awasthi [18], Moatimid and Hassan [19], and Yang et al. [20]. Awasthi Error! Reference source not found. considers effects of heat and mass transfer on the Kelvin-Helmholtz instability along the interfaces which exist between liquid and vapor phases. He observes that heat and mass transfer has a destabilizing effect on the stability of the system, while vapor fraction has stabilizing effect. Moatimid and Hassan [19] also describe heat and mass transfer associated with three-dimensional Kelvin Helmholtz instabilities which exist between liquid and vapor phases. According to these investigators, a decrease of relative streaming velocity produces a stabilizing effect. Yang et al. [20] consider a cylinder channel with a single row of 10 aligned impinging jets, with exit flow in the axial direction at one end of the channel. According to these investigators, Kelvin-Helmholtz vortex development is related to local, instantaneous variations of *Y*-component of vorticity, three-dimensional streamlines, a shear layer parameter, and local static pressure. Of particular importance are the cumulative influences of cross flows, which result in locally increased shear stress magnitudes, enhanced Kelvin-Helmholtz vortex generation instabilities, and increased magnitudes and frequencies of local flow unsteadiness, as subsequent jets are encountered with streamwise development.

Within the present investigation, magnitudes of successive local peak

Nusselt numbers, at successive jet stagnation point impact locations, generally slightly decrease, or are approximately invariant with x/D for all values of Z/D and impingement Reynolds number which are considered. Large hole spacing, which reduces flow mixing and local turbulent transport levels, results in decreased interactions between adjacent jet fluid concentrations, and between the impingement jet fluid and surrounding cross-flows. When examined at a particular value of Rej, streamwise locations of local maximum Nusselt numbers shift to larger x/D locations by only slight amounts, as the normalized jet-to-target distance increases. This is a result of each impingement jet approximates that of a single jet. For this situation, the influences of surrounding jets, including the cumulative-induced crossflows and interactions of jet-induced vortex structures become less pronounced.

Note that x/D and y/D ranges of values, and the numbers of impingement jet events are different in Figures 5-7, as well as in many figures which follow. This is because the dimensional field of view of the camera is approximately invariant, and because impingement holes with different diameters (with associated configuration parameters scaled accordingly) are utilized (as listed in Table 2).

3.2. Line-averaged Nusselt numbers.

Figures 8 and 9 present Nusselt numbers which are line-averaged over y/D from $-$ 6.0 to +6.0 for a hole spacing of 12*D*. Consideration of these results at values of $\mathrm{Re}_j = 8,000$ in Figure 8 shows that data generally increases as Z/D approaches 5.0 near jet impact locations. When $\mathrm{Re}\,j = 30,000,$ line-averaged Nusselt numbers are generally maximum as Z/D approaches 3.0. As such, different Nusselt number dependence upon jet-to target plate distance is present for different Re_j values.

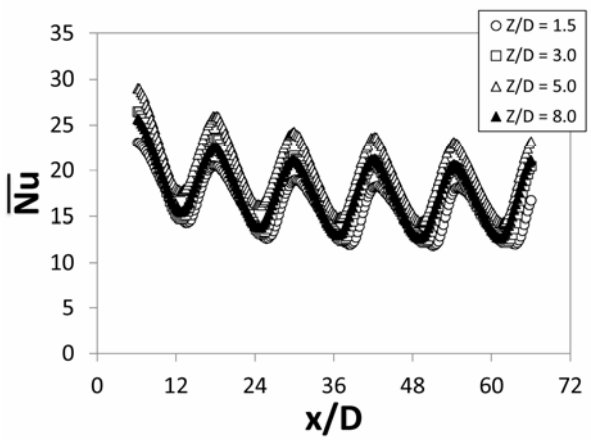

Figure 8. Line-averaged Nusselt numbers as dependent upon x/D for different Z/D values, $\mathrm{Re}_j \approx 8,000$, and $X/D = Y/D = 12$.

Figure 8 also shows that periodic line-averaged Nusselt numbers decrease somewhat at the successive x/D locations, such that successive maximum and minimum values become lower and lower as the impingement flows advect downstream. Such variations are mostly due to cross-flow effects. In general, the cumulative accumulations of cross-flows, from sequential rows of jets, result in sequentially decreasing periodic Nusselt number variations with streamwise development. Local maximum values for Rej of 30,000 also decrease with x/D, but by relatively smaller amounts compared to results in Figure 8. Within Figure 9, this is partially because large hole spacing causes the behavior of each impingement jet to approximate that of a single jet, so that cumulative cross-flow velocities are smaller. As a result, local magnitudes of mixing and turbulent transport are decreased. Interactions between accumulated cross-flow and impingement jet fluid from different rows of holes are diminished. Kelvin-Helmholtz instability generated vortices, which are present along the interface between each jet and the surrounding air, prior to their impingement upon the target plate, also affect this process.

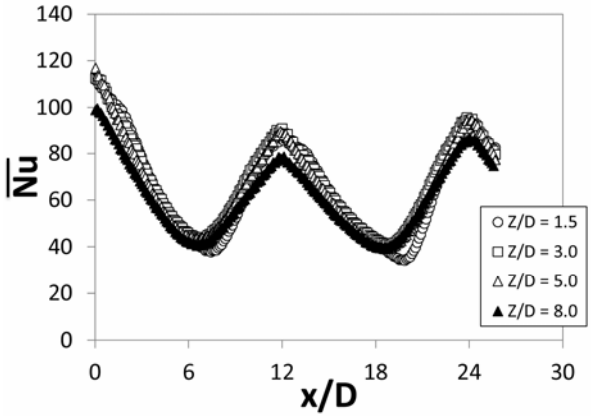

Figure 9. Line-averaged Nusselt numbers as dependent upon x/D for different Z/D values, $\mathrm{Re}_j \approx 30,000$, and $X/D = Y/D = 12$.

3.3. Spatially-averaged Nusselt number variations with Reynolds number.

Spatiallyaveraged Nusselt numbers for Z/D values of 1.5, 3.0, 5.0, and 8.0 are presented in Figures 10 and 11 for $x/D = 6.0$ and $x/D = 18.0$, respectively. These data are given as they vary with Reynolds number Re_j. Each spatially-averaged value is determined over an area which extends over an x/D range from –6.0 to +6.0 relative to each streamwise row location, and over a y/D range of –6.0 to +6.0. As such, each value is also averaged over a range of locations comprised of one complete period of local Nusselt number variation, relative to each streamwise row of holes.

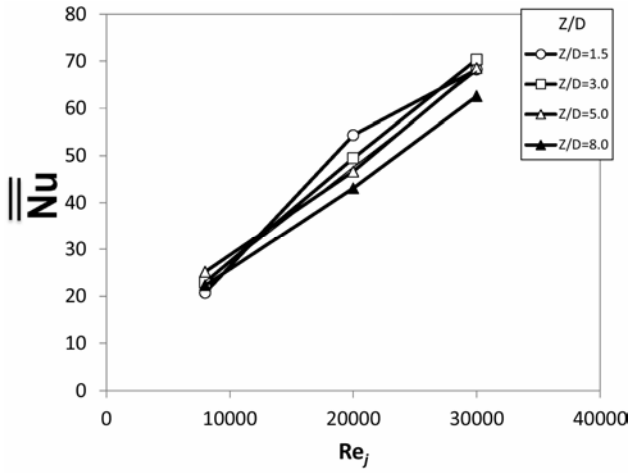

Figure 10. Spatially-averaged Nusselt numbers as dependent upon Re_j for different Z/D values, $x/D = 6.0$

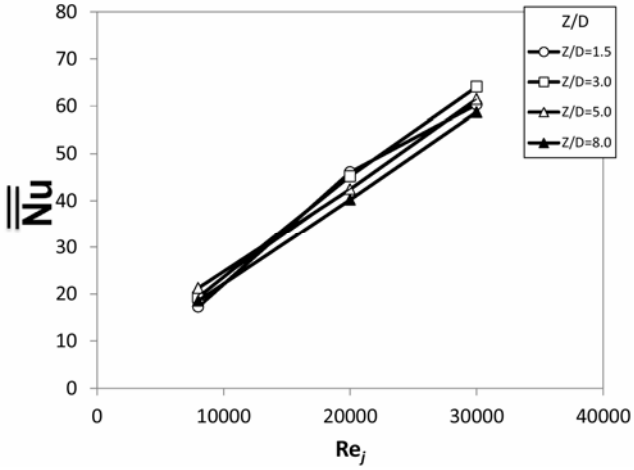

Figure 11. Spatially-averaged Nusselt numbers as dependent upon Re_j for different Z/D values, $x/D = 18.0$

The spatially-averaged Nusselt number data in Figures 10 and 11 are presented to show the dependence upon Reynolds number for $x/D = 6.0$ and 18.0, respectively. Z/D values for the data are 1.5, 3.0, 5.0, and 8.0. In general, spatially-averaged Nusselt numbers are often higher as Reynolds

numbers Re_j increase because of higher advection speeds. These particular data are given for the two most upstream rows of holes, at the smallest x/D values, to illustrate Nusselt number behavior for jets with minimal cross flow, which are generally not influenced by surrounding jets. As such, cross flow influences, which generally vary significantly as Z/D varies, are present only in a minimal manner. Consequently, the data in Figures 10 and 11 show similar dependence on Reynolds number Re_j, regardless of the values of x/D and Z/D, following the same trend with Reynolds number Re_j, within the range of experimental uncertainty magnitudes. This behavior is thus due to the weak accumulation of cross-flows, and less mixing caused by the absence of coolant interactions. Spatially-averaged Nusselt numbers for $Z/D = 5.0$ are significantly higher than for other Z/D values for Re_j of 8000. The highest spatially-averaged Nusselt numbers are present for $Z/D = 3.0$ for Re_j of 30,000. Also important for these variations are the competing influences of two different phenomena. The first one is coherence of individual jets and the strength of adjacent shear layers. The second is the development and advection of vortices generated by Kelvin-Helmholtz instabilities. The coherence of individual jets and the intensity of the adjacent shear layers become stronger at locations closer the point where each jet emerges from an impingement plate hole. In contrast, Kelvin-Helmholtz vortices require some distance from this location to become fully developed.

Figure 12 shows spatially-averaged Nusselt numbers as dependent upon Re_j for different Z/D values, for particular x/D locations $(x/D = 6.0 \text{ and } x/D = 18.0)$. Here, variations of Nusselt number are correlated with respect to the Reynolds number Re_j using the equation given by

$$\overline{\overline{Nu}} = 0.00200 * \mathrm{Re}\, j + 5.56. \quad (7)$$

As such, this correlation equation is valid for $8,000 \le \mathrm{Re}_j \le 30,000$, $X/D = 12$, $Y/D = 12$, $1.5 \le Z/D \le 8.0$, and $6.0 \le x/D \le 18.0$.

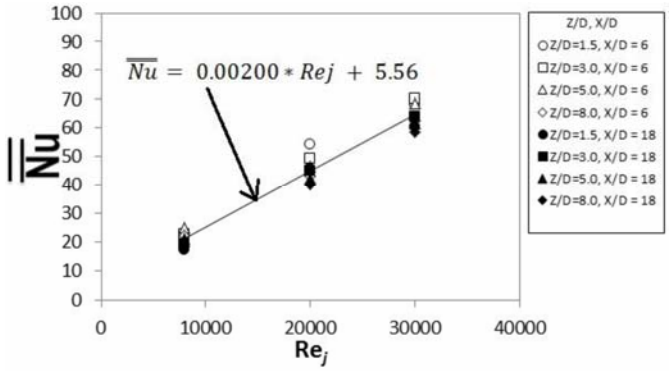

Figure 12. Spatially-averaged Nusselt numbers as dependent upon Re_j for different Z/D values for $x/D = 6.0$ and $x/D = 18.0$, including comparison with correlation equation (7).

3.4. Spatially-averaged Nusselt number variations with Z/D.

Figures 13 and 14 present spatially-averaged Nusselt numbers as dependent upon Z/D for different x/D locations and for Reynolds numbers Re_j of 8,000, and 30,000, respectively. All of these data are provided for a constant a constant jet hole spacing of 12*D*. Figures 13 shows that the highest spatiallyaveraged Nusselt numbers for Reynolds number Re_j of 8,000 are generally present for $Z/D = 5.0$. Figure 14 for Reynolds number Re_j of 30,000 shows that spatially-averaged Nusselt numbers are highest for $Z/D = 3.0$. The relative influences of the jet/shear layer coherence and Kelvin-Helmholtz generated vortices are reflected in the Z/D values associated with the highest Nusselt numbers. For higher jet Reynolds numbers Re_j, jet/shear layer coherence seems to be more important. For lower Reynolds numbers, the Kelvin-Helmholtz vortices are expected to have greater influences.

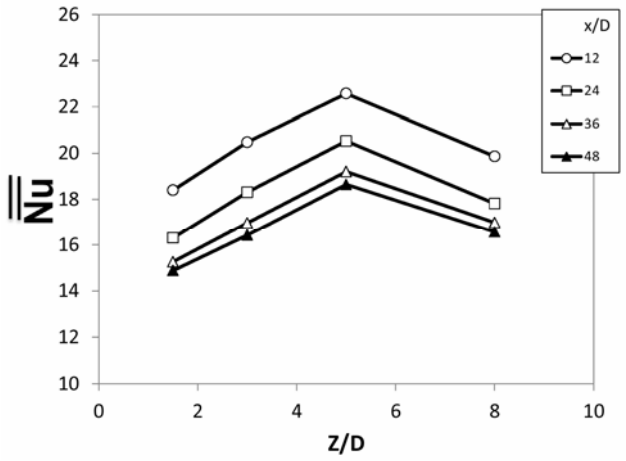

Figure 13. Spatially-averaged Nusselt numbers as dependent upon Z/D for different x/D values, $\mathrm{Re}_j \approx 8,000$

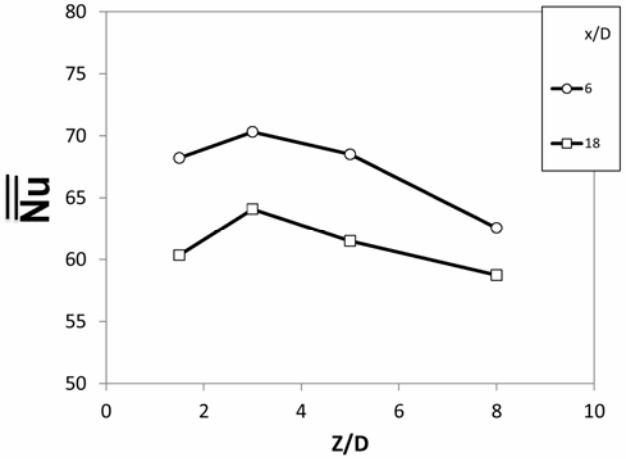

Figure 14. Spatially-averaged Nusselt numbers as dependent upon Z/D for different x/D values, $\mathrm{Re}_j \approx 30,000$

3.5. Comparisons with other investigations.

Spatially-averaged Nusselt numbers for $12D$ hole spacing and $Z/D = 3.0$ are compared to results from Goodro et al. [17] in Figure 15. The present data are given for Reynolds numbers of 8,000, 20,000, and 30,000. In

general, spatially-averaged data from the present study are in good agreement with results from Goodro et al. for all experimental conditions which are examined, which validates the approaches and procedures employed. Note that this comparison is only made for a Z/D value of 3.0.

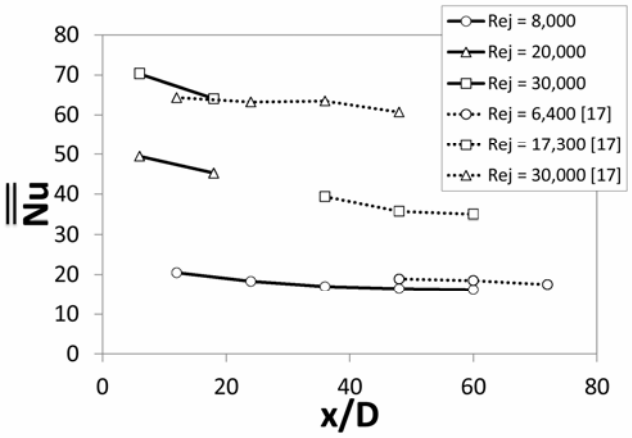

Figure 15. Spatially-averaged Nusselt numbers as dependent upon x/D for different values of Re_j, $Z/D = 3.0,$ including comparisons with Goodro et al. [17].

4. Summary and Conclusions

Experimental results are presented which illustrate the effects of jet-to-target plate distance and Reynolds number on heat transfer distributions for an array of jets impinging on a flat plate with large hole spacing. The array of impinging jets is directed to one flat surface of a channel which is bounded on three sides. Considered are jet Reynolds numbers ranging from 8,000 to 50,000, jet-to-target plate distances of 1.5*D*, 3.0*D*, 5.0*D*, and 8.0*D*, and steamwise and spanwise hole spacing of 12*D*. Associated Mach numbers are low enough to insure that little or no Mach number dependence is present. The thickness of each impingement plate is 1.0*D*. Hole array investigated is arranged with a staggered arrangement from each streamwise row to the next.

In general, the detriment of cross-flows which accumulate in the

impingement passage is reduced for large hole spacing. The accumulated cross-flow does not cause each impingement jet concentration to deflect and bend in the downstream direction by large amounts, compared to arrangements with smaller hole spacing. Local maximum Nusselt number values for 12D jet spacing show only small amount of variation with x/D. This is because each jet produced using $X/D = Y/D = 12$ approximates the behavior of an individual jet. Local, line-averaged, and spatially-averaged Nusselt numbers show strong dependence on the impingement jet Reynolds number for all situations examined. Local Nusselt numbers at each x/D and y/D location generally increase continually as the impingement jet Reynolds number increases. This dependence of spatially-averaged Nusselt number is quantified using a correlation for the two most upstream rows of impingement jets (at the smallest x/D values), where cross flows and jet interactions are minimal.

Experimental results also illustrate important variations of local, line-averaged, and area-averaged Nusselt numbers with normalized jet-to-target plate distance. As such, the highest Nusselt numbers are present for $Z/D = 3.0$ for Re_j of 30,000. When $\mathrm{Re}_j = 8,000$, the highest Nusselt numbers are also present for $Z/D = 0.5$. This is a result of the competing influence of: (i) the coherence of individual jets and the strength of adjacent shear layers, and (ii) the development and advection of vortices generated by Kelvin-Helmholtz instabilities.

Acknowledgements

The research presented in this paper was sponsored by Solar Turbines Inc., located in San Diego, California.

References

[1] H. Martin, Heat and Mass Transfer Between Impinging Gas Jets and Solid Surfaces, Advances in Heat Transfer, Academic Press 13 (1977), 1-60.

[2] A. Schulz, Combustor Liner Cooling Technology In Scope of Reduced Pollutant Formation and Rising Thermal Efficiencies, Heat Transfer in Gas Turbine Systems, Annals of the New York Academy of Sciences 934 (2001), 135-146.

[3] D. M. Kercher and W. Tabakoff, Heat Transfer By a Square Array of Round Air Jets Impinging Perpendicular to a Flat Surface Including the Effect of Spent Air, ASME Transactions-Journal of Engineering for Power 92 (1970), 73-82.

[4] D. E. Metzger and R. Korstad, Effects of Crossflow On Impingement Heat Transfer, ASME Transactions-Journal of Engineering for Power 94 (1972), 35-41.

[5] J. L. Chance, Experimental Investigation of Air Impingement Heat Transfer Under an Array of Round Jets, TAPPI 57(6) (1974), 108-112.

[6] D. E. Metzger, L. W. Florschuetz, D. I. Takeuchi, R. D. Behee and R. A. Berry, Heat Transfer Characteristics for Inline and Staggered Arrays of Circular Jets With Crossflow of Spent Air, ASME Transactions-Journal of Heat Transfer 101 (1979), 526-531.

[7] L. W. Florschuetz, C. R. Truman and D. E. Metzger, Streamwise Flow and Heat Transfer Distributions for Jet Array Impingement With Crossflow, ASME Transactions-Journal of Heat Transfer 103 (1981), 337-342.

[8] N. T. Obot and T. A. Trabold, Impingement Heat Transfer Within Arrays of Circular Jets: Part 1-Effects of Minimum, Intermediate, and Complete Crossflow for Small and Large Spacings, ASME Transactions-Journal of Heat Transfer 109 (1987), 872-879.

[9] J. C. Bailey and R. S. Bunker, Local Heat Transfer and Flow Distributions For Impinging Jet Arrays of Dense and Sparse Extent, ASME Paper No. ASME GT-(2002), 2002-30473.

[10] J. Y. San, Y. M. Tsou and Z. C. Chen, Impingement Heat Transfer of Staggered Arrays of Air Jets Confined in a Channel, International Journal of Heat and Mass Transfer 50(19-20) (2007), 3718-3727.

[11] J. M. Miao, C. Y. Wu and P. H. Chen, Numerical Investigation of Confined Multiple-Jet Impingement Cooling over a Flat Plat at Different Crossflow Orientations, Numerical Heat Transfer, Part A: Applications: An International Journal of Computation and Methodology 55(11) (2009), 1019-1050.

[12] K. Vadiraj and S. V. Prabhu, Influence of Spanwise Pitch on Local Heat Transfer Distribution for In-Line Arrays of Circular Jets with Spent Air Flow in Two Opposite Directions, Experimental Thermal and Fluid Science 33 (2008), 84-95.

[13] P. Brevet, C. Dejeu, E. Dorignac, M. Jolly and J. J. Vullierme, Heat Transfer to a

Row of Impinging Jets In Consideration of Optimization, International Journal of Heat and Mass Transfer 45 (2002), 4191-4200.

[14] S. J. Kline and F. A. McClintock, Describing Uncertainties in Single Sample Experiments, Mechanical Engineering 75 (1953), 3-8.

[15] R. J. Moffat, Describing the Uncertainties in Experimental Results," Experimental Thermal and Fluid Science 1(1) (1988), 3-17.

[16] J. Park, M. Goodro, P. M. Ligrani, M. Fox and H.-K. Moon, Separate Effects of Mach Number and Reynolds Number on Jet Array Impingement Heat Transfer, ASME Transactions-Journal of Turbomachinery 129(2) (2007), 269-280.

[17] M. Goodro, P. M. Ligrani, M. Fox, and H.-K. Moon, Mach Number, Reynolds Number, Jet Spacing Variations: Full Array of Impinging Jets, AL & A Journal of Thermophysics and Heat Transfer 24(1) (2010), 133-144.

[18] M. K. Awasthi, Study on Kelvin-Helmholtz Instability With Heat and Mass Transfer, ASME Transactions-Journal of Fluids Engineering 136(12) (2014), 121202-1 to 121202-9.

[19] G. M. Moatimid and M. A. Hassan, Three-Dimensional Viscous Potential Electrohydrodynamic Kelvin-Helmholtz Instability through Vertical Cylindrical Porous Inclusions with Permeable Boundaries, ASME Transactions-Journal of Fluids Engineering 136(2) (2013), 021203-1 to 021203-10.

[20] L. Yang, P. M. Ligrani, J. Ren and H. Jiang, Unsteady Structure and Development of a Row of Impingement Jets, Including Kelvin-Helmholtz Vortex Development, ASME Transactions-Journal of Fluids Engineering 137(5) (2015), 051201-1 to 051201-12.

CHAPTER 5

SUMMARY AND CONCLUSIONS

In conclusion, the present study provides information which can be used to optimize and design impingement array configurations to satisfy high demand of surface heat transfer augmentation levels. These levels are characterized by use of local, line-averaged, and spatially-averaged distributions of the Nusselt number. In present study, to complete the investigation, data is obtained to show the effects of jet-to-target distance and jet hole spacing on cross-flows at constant Reynolds number. Next, considered are the combined and separate effects of hole array spacing, jet-to-target plate distance, and Reynolds number on cross-flows. In addition, the present investigation also shows the effects of large hole spacing. Included are the effects of jet-to-target plate distance, and jet Reynolds number.

For the first set of experiments, new impingement heat transfer data are presented for experimental conditions and configurations employed have not been previously examined. These data illustrate the effects of impingement cross-flows on local, line-averaged, and spatially-averaged Nusselt numbers, as both jet-to-target distance and jet hole spacing are altered. With this arrangement, the impingement jets are directed to one flat surface of a channel which is bounded on three sides. Data are given for a constant impingement jet Reynolds number of 8,000. In general, the impingement passage cross-flows which accumulate are detrimental to local Nusselt number performance, especially for denser hole arrays with 5D and 8D hole spacing, where D is impingement hole diameter. This is illustrated by periodic variations of surface Nusselt numbers, which

generally decrease with streamwise development, and by local Nusselt number *peak values* for hole spacings of 5*D*, 8*D*, and 12*D* which generally become smaller at successive *x/D* locations for each value of *Z/D*. Also considered are unique situations where significant accumulation of cross-flow fluid results in an opposite trend, with increasing local Nusselt numbers with streamwise development for dense hole spacing of 5*D*, and smaller jet-to-target plate distances of 1.5*D* and 3.0*D*.

For the second set of experiments, data are presented which illustrate the combined and separate effects of hole array spacing, jet-to-target plate distance, and Reynolds number on cross-flows, and the resulting heat transfer, for an impingement jet array. The array of impinging jets is again directed to one flat surface of a channel which is bounded on three sides. Considered are Reynolds numbers ranging from 8,000 to 50,000, jet-to-target plate distances of 1.5*D*, 3.0*D*, 5.0*D*, and 8.0*D*, and steamwise and spanwise hole spacing of 5*D*, 8*D*, and 12*D*, where *D* is the impingement hole diameter. In general, the cumulative accumulations of cross-flows, from sequential rows of jets, reduce the effectiveness of each individual jet (especially for jets at larger streamwise locations). In other situations, the impingement cross-flow results in locally augmented Nusselt numbers. Such variations most often occur at larger downstream locations, as jet interactions are more vigorous, and local magnitudes of mixing and turbulent transport are augmented. This occurs in channels at lower Reynolds numbers, where impingement jets are confined by smaller hole spacing, and smaller jet-to-target plate distance. The overall result is complex dependence of local, line-averaged, and spatially-averaged Nusselt numbers on hole array spacing, jet-to-target plate distance, and impingement jet Reynolds number.

For the third set of experiments, data are presented which illustrate surface heat transfer characteristics of an array of impinging jets with large hole spacing on the same flat plate and impingement passage arrangement mentioned previously. Included are the effects of jet-to-target plate distance, and jet Reynolds number. Steamwise and spanwise hole spacing is 12*D*. Jet-to-target plate distances *Z* of 1.5*D*, 3.0*D*, 5.0*D*, and 8.0*D* are employed, where *D* is the impingement hole diameter. Reynolds numbers Re_j range from 8,000 to 50,000, with isentropic jet Mach numbers of approximately 0.1 to 0.2. Experimental results include local, line-averaged, and spatially-averaged Nusselt number distributions. All of these different types of Nusselt numbers show strong dependence on the impingement jet Reynolds number for all situations examined. This dependence of spatially-averaged Nusselt number is quantified using a correlation for the two most upstream rows of impingement jets (at the smallest *x/D* values), where crossflows and jet interactions are almost completely non-existent. Overall, the highest local Nusselt numbers are present for *Z/D* = 3.0 for Re_j of 20,000, 30,000, and 50,000, with local Nu number decreases as *Z/D* increases further. For Re_j of 8,000, the highest Nusselt number values are present for *Z/D* = 5.0. In general, using *X/D* = *Y/D* = 12, the influences of surrounding jets, including cumulative-induced crossflows and interactions of jet-induced vortex structures are less pronounced, relative to configurations with smaller hole spacing. For large hole spacing, both local and line-averaged maximum Nusselt number data trends show only very small variations with increasing *x/D*. As such, important differences relative to impingement arrays with smaller hole spacing are evident, especially in regard to Nusselt number variations as streamwise location, jet-to-target plate distance, and Reynolds number are changed.

APPENDIX A

UNCERTAINTY ANALYSIS

Uncertainty estimates are based on 95 percent confidence levels and are determined using methods described by Kline and McClintock [14] and Moffat [15]. Experimental Uncertainty which shows below is from Chapter 2.

Table A.1. Uncertainty Analysis

Nomenclature	**Unit**	**Measurement Device**	**Error**
I	A	Simpson 260 Volt-Ohm-Milliammeters	2 %
V	V	Fluke 8846A Digit Multimeter	0.0017
A_{ht}	m^2	Dial Caliper Mitutoyo 505-671	0.0003 × 2
D	m	Dial Caliper Mitutoyo 505-671	0.0003
T_w	℃	IR camera calibrated T-T/C	0.758 ~ 1.5
T_{0j}	℃	Omega T-type(TT-T-40-72")	0.15
α	*W/(m*K)*	-	0.0138 %

Quantity	*Experimental Uncertainty (percent)*
A_{ht}	1.394
D	4.919
T_w	2.706
T_{oj}	0.722
α	0.541
Nu	6.043

APPENDIX B

DATA FILE DIRECTORY

Appendix B presents a listing of data files by filename. These data files include both the raw and reduced data files for the results presented in this thesis defense.

1. Listing of experimental data files for cross-flow effects on impingement array heat transfer with varying jet-to-target plate distance and hole spacing

Folder name	Rej	Hole Spacing (X/D=Y/D)	Z/D	D (mm)	Data file name	Description
exp1	8000	5.0	1.5	4.5	d_nu1.txt	Raw Nusselt number in text data file
					total.bmp	Average IR camera bitmap image for camera calibration
					A.xls	Excel file with grayscale values to temperature camera calibration
					Summary Output data.docx	Word file with test conditions
					Contour plot.dg6	Delta graph with nusselt number contour plot
					Local Nu.xls	Excel file contains local nusselt number
					Line area avg Nu.xls	Excel file contains line and area averaged nusselt number
exp2	8000	5.0	3.0	4.5	d_nu1.txt	Raw Nusselt number in text data file
					total.bmp	Average IR camera bitmap image for camera calibration
					A.xls	Excel file with grayscale values to temperature camera calibration
					Summary Output data.docx	Word file with test conditions
					Contour plot.dg6	Delta graph with nusselt number contour plot
					Local Nu.xls	Excel file contains local nusselt number
					Line area avg Nu.xls	Excel file contains line and area averaged nusselt number
exp3	8000	5.0	5.0	4.5	d_nu1.txt	Raw Nusselt number in text data file
					total.bmp	Average IR camera bitmap image for camera calibration

					A.xls	Excel file with grayscale values to temperature camera calibration
					Summary Output data.docx	Word file with test conditions
					Contour plot.dg6	Delta graph with nusselt number contour plot
					Local Nu.xls	Excel file contains local nusselt number
					Line area avg Nu.xls	Excel file contains line and area averaged nusselt number
exp4	8000	5.0	8.0	4.5	d_nu1.txt	Raw Nusselt number in text data file
					total.bmp	Average IR camera bitmap image for camera calibration
					A.xls	Excel file with grayscale values to temperature camera calibration
					Summary Output data.docx	Word file with test conditions
					Contour plot.dg6	Delta graph with nusselt number contour plot
					Local Nu.xls	Excel file contains local nusselt number
					Line area avg Nu.xls	Excel file contains line and area averaged nusselt number
exp5	8000	8.0	1.5	4.5	d_nu1.txt	Raw Nusselt number in text data file
					total.bmp	Average IR camera bitmap image for camera calibration
					A.xls	Excel file with grayscale values to temperature camera calibration
					Summary Output data.docx	Word file with test conditions
					Contour plot.dg6	Delta graph with nusselt number contour plot
					Local Nu.xls	Excel file contains local nusselt number

					Line area avg Nu.xls	Excel file contains line and area averaged nusselt number
exp6	8000	8.0	3.0	4.5	d_nu1.txt	Raw Nusselt number in text data file
					total.bmp	Average IR camera bitmap image for camera calibration
					A.xls	Excel file with grayscale values to temperature camera calibration
					Summary Output data.docx	Word file with test conditions
					Contour plot.dg6	Delta graph with nusselt number contour plot
					Local Nu.xls	Excel file contains local nusselt number
					Line area avg Nu.xls	Excel file contains line and area averaged nusselt number
exp7	8000	8.0	5.0	4.5	d_nu1.txt	Raw Nusselt number in text data file
					total.bmp	Average IR camera bitmap image for camera calibration
					A.xls	Excel file with grayscale values to temperature camera calibration
					Summary Output data.docx	Word file with test conditions
					Contour plot.dg6	Delta graph with nusselt number contour plot
					Local Nu.xls	Excel file contains local nusselt number
					Line area avg Nu.xls	Excel file contains line and area averaged nusselt number
exp8	8000	8.0	8.0	4.5	d_nu1.txt	Raw Nusselt number in text data file
					total.bmp	Average IR camera bitmap image for camera calibration
					A.xls	Excel file with grayscale values to temperature camera calibration

					Summary Output data.docx	Word file with test conditions
					Contour plot.dg6	Delta graph with nusselt number contour plot
					Local Nu.xls	Excel file contains local nusselt number
					Line area avg Nu.xls	Excel file contains line and area averaged nusselt number
exp9	8000	12.0	1.5	3.5	d_nu1.txt	Raw Nusselt number in text data file
					total.bmp	Average IR camera bitmap image for camera calibration
					A.xls	Excel file with grayscale values to temperature camera calibration
					Summary Output data.docx	Word file with test conditions
					Contour plot.dg6	Delta graph with nusselt number contour plot
					Local Nu.xls	Excel file contains local nusselt number
					Line area avg Nu.xls	Excel file contains line and area averaged nusselt number
exp10	8000	12.0	3.0	3.5	d_nu1.txt	Raw Nusselt number in text data file
					total.bmp	Average IR camera bitmap image for camera calibration
					A.xls	Excel file with grayscale values to temperature camera calibration
					Summary Output data.docx	Word file with test conditions
					Contour plot.dg6	Delta graph with nusselt number contour plot
					Local Nu.xls	Excel file contains local nusselt number
					Line area avg Nu.xls	Excel file contains line and area averaged nusselt number
exp11	8000	12.0	5.0	3.5	d_nu1.txt	Raw Nusselt number in text data file

					total.bmp	Average IR camera bitmap image for camera calibration
					A.xls	Excel file with grayscale values to temperature camera calibration
					Summary Output data.docx	Word file with test conditions
					Contour plot.dg6	Delta graph with nusselt number contour plot
					Local Nu.xls	Excel file contains local nusselt number
					Line area avg Nu.xls	Excel file contains line and area averaged nusselt number
exp12	8000	12.0	8.0	3.5	d_nu1.txt	Raw Nusselt number in text data file
					total.bmp	Average IR camera bitmap image for camera calibration
					A.xls	Excel file with grayscale values to temperature camera calibration
					Summary Output data.docx	Word file with test conditions
					Contour plot.dg6	Delta graph with nusselt number contour plot
					Local Nu.xls	Excel file contains local nusselt number
					Line area avg Nu.xls	Excel file contains line and area averaged nusselt number

2. Listing of experimental data files for crossflows from jet array impingement cooling hole spacing, target plate distance, Reynolds number

Folder name	Rej	Hole Spacing (X/D=Y/D)	Z/D	D (mm)	Data file name	Description
exp13	8000	5.0	1.5	4.5	d_nu1.txt	Raw Nusselt number in text data file
					total.bmp	Average IR camera bitmap image for camera calibration
					A.xls	Excel file with grayscale values to temperature camera calibration
					Summary Output data.docx	Word file with test conditions
					Contour plot.dg6	Delta graph with nusselt number contour plot
					Local Nu.xls	Excel file contains local nusselt number
					Line area avg Nu.xls	Excel file contains line and area averaged nusselt number
exp14	8000	5.0	3.0	4.5	d_nu1.txt	Raw Nusselt number in text data file
					total.bmp	Average IR camera bitmap image for camera calibration
					A.xls	Excel file with grayscale values to temperature camera calibration
					Summary Output data.docx	Word file with test conditions
					Contour plot.dg6	Delta graph with nusselt number contour plot
					Local Nu.xls	Excel file contains local nusselt number
					Line area avg Nu.xls	Excel file contains line and area averaged nusselt number
exp15	8000	5.0	5.0	4.5	d_nu1.txt	Raw Nusselt number in text data file
					total.bmp	Average IR camera bitmap image for camera calibration

					A.xls	Excel file with grayscale values to temperature camera calibration
					Summary Output data.docx	Word file with test conditions
					Contour plot.dg6	Delta graph with nusselt number contour plot
					Local Nu.xls	Excel file contains local nusselt number
					Line area avg Nu.xls	Excel file contains line and area averaged nusselt number
exp16	8000	5.0	8.0	4.5	d_nu1.txt	Raw Nusselt number in text data file
					total.bmp	Average IR camera bitmap image for camera calibration
					A.xls	Excel file with grayscale values to temperature camera calibration
					Summary Output data.docx	Word file with test conditions
					Contour plot.dg6	Delta graph with nusselt number contour plot
					Local Nu.xls	Excel file contains local nusselt number
					Line area avg Nu.xls	Excel file contains line and area averaged nusselt number
exp17	20000	5.0	1.5	4.5	d_nu1.txt	Raw Nusselt number in text data file
					total.bmp	Average IR camera bitmap image for camera calibration
					A.xls	Excel file with grayscale values to temperature camera calibration
					Summary Output data.docx	Word file with test conditions
					Contour plot.dg6	Delta graph with nusselt number contour plot
					Local Nu.xls	Excel file contains local nusselt number

					Line area avg Nu.xls	Excel file contains line and area averaged nusselt number
exp18	20000	5.0	3.0	4.5	d_nu1.txt	Raw Nusselt number in text data file
					total.bmp	Average IR camera bitmap image for camera calibration
					A.xls	Excel file with grayscale values to temperature camera calibration
					Summary Output data.docx	Word file with test conditions
					Contour plot.dg6	Delta graph with nusselt number contour plot
					Local Nu.xls	Excel file contains local nusselt number
					Line area avg Nu.xls	Excel file contains line and area averaged nusselt number
exp19	20000	5.0	5.0	4.5	d_nu1.txt	Raw Nusselt number in text data file
					total.bmp	Average IR camera bitmap image for camera calibration
					A.xls	Excel file with grayscale values to temperature camera calibration
					Summary Output data.docx	Word file with test conditions
					Contour plot.dg6	Delta graph with nusselt number contour plot
					Local Nu.xls	Excel file contains local nusselt number
					Line area avg Nu.xls	Excel file contains line and area averaged nusselt number
exp20	20000	5.0	8.0	4.5	d_nu1.txt	Raw Nusselt number in text data file
					total.bmp	Average IR camera bitmap image for camera calibration
					A.xls	Excel file with grayscale values to temperature camera calibration

					Summary Output data.docx	Word file with test conditions
					Contour plot.dg6	Delta graph with nusselt number contour plot
					Local Nu.xls	Excel file contains local nusselt number
					Line area avg Nu.xls	Excel file contains line and area averaged nusselt number
exp21	30000	5.0	1.5	4.5	d_nu1.txt	Raw Nusselt number in text data file
					total.bmp	Average IR camera bitmap image for camera calibration
					A.xls	Excel file with grayscale values to temperature camera calibration
					Summary Output data.docx	Word file with test conditions
					Contour plot.dg6	Delta graph with nusselt number contour plot
					Local Nu.xls	Excel file contains local nusselt number
					Line area avg Nu.xls	Excel file contains line and area averaged nusselt number
exp22	30000	5.0	3.0	4.5	d_nu1.txt	Raw Nusselt number in text data file
					total.bmp	Average IR camera bitmap image for camera calibration
					A.xls	Excel file with grayscale values to temperature camera calibration
					Summary Output data.docx	Word file with test conditions
					Contour plot.dg6	Delta graph with nusselt number contour plot
					Local Nu.xls	Excel file contains local nusselt number
					Line area avg Nu.xls	Excel file contains line and area averaged nusselt number
exp23	30000	5.0	5.0	4.5	d_nu1.txt	Raw Nusselt number in text data file

					total.bmp	Average IR camera bitmap image for camera calibration
					A.xls	Excel file with grayscale values to temperature camera calibration
					Summary Output data.docx	Word file with test conditions
					Contour plot.dg6	Delta graph with nusselt number contour plot
					Local Nu.xls	Excel file contains local nusselt number
					Line area avg Nu.xls	Excel file contains line and area averaged nusselt number
exp24	30000	5.0	8.0	4.5	d_nu1.txt	Raw Nusselt number in text data file
					total.bmp	Average IR camera bitmap image for camera calibration
					A.xls	Excel file with grayscale values to temperature camera calibration
					Summary Output data.docx	Word file with test conditions
					Contour plot.dg6	Delta graph with nusselt number contour plot
					Local Nu.xls	Excel file contains local nusselt number
					Line area avg Nu.xls	Excel file contains line and area averaged nusselt number
exp25	50000	5.0	1.5	4.5	d_nu1.txt	Raw Nusselt number in text data file
					total.bmp	Average IR camera bitmap image for camera calibration
					A.xls	Excel file with grayscale values to temperature camera calibration
					Summary Output data.docx	Word file with test conditions
					Contour plot.dg6	Delta graph with nusselt number contour plot

					Local Nu.xls	Excel file contains local nusselt number
					Line area avg Nu.xls	Excel file contains line and area averaged nusselt number
exp26	50000	5.0	3.0	4.5	d_nu1.txt	Raw Nusselt number in text data file
					total.bmp	Average IR camera bitmap image for camera calibration
					A.xls	Excel file with grayscale values to temperature camera calibration
					Summary Output data.docx	Word file with test conditions
					Contour plot.dg6	Delta graph with nusselt number contour plot
					Local Nu.xls	Excel file contains local nusselt number
					Line area avg Nu.xls	Excel file contains line and area averaged nusselt number
exp27	50000	5.0	5.0	4.5	d_nu1.txt	Raw Nusselt number in text data file
					total.bmp	Average IR camera bitmap image for camera calibration
					A.xls	Excel file with grayscale values to temperature camera calibration
					Summary Output data.docx	Word file with test conditions
					Contour plot.dg6	Delta graph with nusselt number contour plot
					Local Nu.xls	Excel file contains local nusselt number
					Line area avg Nu.xls	Excel file contains line and area averaged nusselt number

exp28	50000	5.0	8.0	4.5	d_nu1.txt	Raw Nusselt number in text data file
					total.bmp	Average IR camera bitmap image for camera calibration
					A.xls	Excel file with grayscale values to temperature camera calibration
					Summary Output data.docx	Word file with test conditions
					Contour plot.dg6	Delta graph with nusselt number contour plot
					Local Nu.xls	Excel file contains local nusselt number
					Line area avg Nu.xls	Excel file contains line and area averaged nusselt number
exp29	8000	8.0	1.5	4.5	d_nu1.txt	Raw Nusselt number in text data file
					total.bmp	Average IR camera bitmap image for camera calibration
					A.xls	Excel file with grayscale values to temperature camera calibration
					Summary Output data.docx	Word file with test conditions
					Contour plot.dg6	Delta graph with nusselt number contour plot
					Local Nu.xls	Excel file contains local nusselt number
					Line area avg Nu.xls	Excel file contains line and area averaged nusselt number
exp30	8000	8.0	3.0	4.5	d_nu1.txt	Raw Nusselt number in text data file
					total.bmp	Average IR camera bitmap image for camera calibration
					A.xls	Excel file with grayscale values to temperature camera calibration
					Summary Output data.docx	Word file with test conditions

					Contour plot.dg6	Delta graph with nusselt number contour plot
					Local Nu.xls	Excel file contains local nusselt number
					Line area avg Nu.xls	Excel file contains line and area averaged nusselt number
exp31	8000	8.0	5.0	4.5	d_nu1.txt	Raw Nusselt number in text data file
					total.bmp	Average IR camera bitmap image for camera calibration
					A.xls	Excel file with grayscale values to temperature camera calibration
					Summary Output data.docx	Word file with test conditions
					Contour plot.dg6	Delta graph with nusselt number contour plot
					Local Nu.xls	Excel file contains local nusselt number
					Line area avg Nu.xls	Excel file contains line and area averaged nusselt number
exp32	8000	8.0	8.0	4.5	d_nu1.txt	Raw Nusselt number in text data file
					total.bmp	Average IR camera bitmap image for camera calibration
					A.xls	Excel file with grayscale values to temperature camera calibration
					Summary Output data.docx	Word file with test conditions
					Contour plot.dg6	Delta graph with nusselt number contour plot
					Local Nu.xls	Excel file contains local nusselt number
					Line area avg Nu.xls	Excel file contains line and area averaged nusselt number
exp33	20000	8.0	1.5	4.5	d_nu1.txt	Raw Nusselt number in text data file

					total.bmp	Average IR camera bitmap image for camera calibration
					A.xls	Excel file with grayscale values to temperature camera calibration
					Summary Output data.docx	Word file with test conditions
					Contour plot.dg6	Delta graph with nusselt number contour plot
					Local Nu.xls	Excel file contains local nusselt number
					Line area avg Nu.xls	Excel file contains line and area averaged nusselt number
exp34	20000	8.0	3.0	4.5	d_nu1.txt	Raw Nusselt number in text data file
					total.bmp	Average IR camera bitmap image for camera calibration
					A.xls	Excel file with grayscale values to temperature camera calibration
					Summary Output data.docx	Word file with test conditions
					Contour plot.dg6	Delta graph with nusselt number contour plot
					Local Nu.xls	Excel file contains local nusselt number
					Line area avg Nu.xls	Excel file contains line and area averaged nusselt number
exp35	20000	8.0	5.0	4.5	d_nu1.txt	Raw Nusselt number in text data file
					total.bmp	Average IR camera bitmap image for camera calibration
					A.xls	Excel file with grayscale values to temperature camera calibration
					Summary Output data.docx	Word file with test conditions
					Contour plot.dg6	Delta graph with nusselt number contour plot

					Local Nu.xls	Excel file contains local nusselt number
					Line area avg Nu.xls	Excel file contains line and area averaged nusselt number
exp36	20000	8.0	8.0	4.5	d_nu1.txt	Raw Nusselt number in text data file
					total.bmp	Average IR camera bitmap image for camera calibration
					A.xls	Excel file with grayscale values to temperature camera calibration
					Summary Output data.docx	Word file with test conditions
					Contour plot.dg6	Delta graph with nusselt number contour plot
					Local Nu.xls	Excel file contains local nusselt number
					Line area avg Nu.xls	Excel file contains line and area averaged nusselt number
exp37	30000	8.0	1.5	4.5	d_nu1.txt	Raw Nusselt number in text data file
					total.bmp	Average IR camera bitmap image for camera calibration
					A.xls	Excel file with grayscale values to temperature camera calibration
					Summary Output data.docx	Word file with test conditions
					Contour plot.dg6	Delta graph with nusselt number contour plot
					Local Nu.xls	Excel file contains local nusselt number
					Line area avg Nu.xls	Excel file contains line and area averaged nusselt number
exp38	30000	8.0	3.0	4.5	d_nu1.txt	Raw Nusselt number in text data file
					total.bmp	Average IR camera bitmap image for camera calibration

					A.xls	Excel file with grayscale values to temperature camera calibration
					Summary Output data.docx	Word file with test conditions
					Contour plot.dg6	Delta graph with nusselt number contour plot
					Local Nu.xls	Excel file contains local nusselt number
					Line area avg Nu.xls	Excel file contains line and area averaged nusselt number
exp39	30000	8.0	5.0	4.5	d_nu1.txt	Raw Nusselt number in text data file
					total.bmp	Average IR camera bitmap image for camera calibration
					A.xls	Excel file with grayscale values to temperature camera calibration
					Summary Output data.docx	Word file with test conditions
					Contour plot.dg6	Delta graph with nusselt number contour plot
					Local Nu.xls	Excel file contains local nusselt number
					Line area avg Nu.xls	Excel file contains line and area averaged nusselt number
exp40	30000	8.0	8.0	4.5	d_nu1.txt	Raw Nusselt number in text data file
					total.bmp	Average IR camera bitmap image for camera calibration
					A.xls	Excel file with grayscale values to temperature camera calibration
					Summary Output data.docx	Word file with test conditions
					Contour plot.dg6	Delta graph with nusselt number contour plot
					Local Nu.xls	Excel file contains local nusselt number

					Line area avg Nu.xls	Excel file contains line and area averaged nusselt number
exp41	50000	8.0	1.5	4.5	d_nu1.txt	Raw Nusselt number in text data file
					total.bmp	Average IR camera bitmap image for camera calibration
					A.xls	Excel file with grayscale values to temperature camera calibration
					Summary Output data.docx	Word file with test conditions
					Contour plot.dg6	Delta graph with nusselt number contour plot
					Local Nu.xls	Excel file contains local nusselt number
					Line area avg Nu.xls	Excel file contains line and area averaged nusselt number
exp42	50000	8.0	3.0	4.5	d_nu1.txt	Raw Nusselt number in text data file
					total.bmp	Average IR camera bitmap image for camera calibration
					A.xls	Excel file with grayscale values to temperature camera calibration
					Summary Output data.docx	Word file with test conditions
					Contour plot.dg6	Delta graph with nusselt number contour plot
					Local Nu.xls	Excel file contains local nusselt number
					Line area avg Nu.xls	Excel file contains line and area averaged nusselt number
exp43	50000	8.0	5.0	4.5	d_nu1.txt	Raw Nusselt number in text data file
					total.bmp	Average IR camera bitmap image for camera calibration
					A.xls	Excel file with grayscale values to temperature camera calibration

					Summary Output data.docx	Word file with test conditions
					Contour plot.dg6	Delta graph with nusselt number contour plot
					Local Nu.xls	Excel file contains local nusselt number
					Line area avg Nu.xls	Excel file contains line and area averaged nusselt number
exp44	50000	8.0	8.0	4.5	d_nu1.txt	Raw Nusselt number in text data file
					total.bmp	Average IR camera bitmap image for camera calibration
					A.xls	Excel file with grayscale values to temperature camera calibration
					Summary Output data.docx	Word file with test conditions
					Contour plot.dg6	Delta graph with nusselt number contour plot
					Local Nu.xls	Excel file contains local nusselt number
					Line area avg Nu.xls	Excel file contains line and area averaged nusselt number
exp45	8000	12.0	1.5	3.5	d_nu1.txt	Raw Nusselt number in text data file
					total.bmp	Average IR camera bitmap image for camera calibration
					A.xls	Excel file with grayscale values to temperature camera calibration
					Summary Output data.docx	Word file with test conditions
					Contour plot.dg6	Delta graph with nusselt number contour plot
					Local Nu.xls	Excel file contains local nusselt number
					Line area avg Nu.xls	Excel file contains line and area averaged nusselt number
exp46	8000	12.0	3.0	3.5	d_nu1.txt	Raw Nusselt number in text data file

					total.bmp	Average IR camera bitmap image for camera calibration
					A.xls	Excel file with grayscale values to temperature camera calibration
					Summary Output data.docx	Word file with test conditions
					Contour plot.dg6	Delta graph with nusselt number contour plot
					Local Nu.xls	Excel file contains local nusselt number
					Line area avg Nu.xls	Excel file contains line and area averaged nusselt number
exp47	8000	12.0	5.0	3.5	d_nu1.txt	Raw Nusselt number in text data file
					total.bmp	Average IR camera bitmap image for camera calibration
					A.xls	Excel file with grayscale values to temperature camera calibration
					Summary Output data.docx	Word file with test conditions
					Contour plot.dg6	Delta graph with nusselt number contour plot
					Local Nu.xls	Excel file contains local nusselt number
					Line area avg Nu.xls	Excel file contains line and area averaged nusselt number
exp48	8000	12.0	8.0	3.5	d_nu1.txt	Raw Nusselt number in text data file
					total.bmp	Average IR camera bitmap image for camera calibration
					A.xls	Excel file with grayscale values to temperature camera calibration
					Summary Output data.docx	Word file with test conditions
					Contour plot.dg6	Delta graph with nusselt number contour plot

					Local Nu.xls	Excel file contains local nusselt number
					Line area avg Nu.xls	Excel file contains line and area averaged nusselt number
exp49	20000	12.0	1.5	3.5	d_nu1.txt	Raw Nusselt number in text data file
					total.bmp	Average IR camera bitmap image for camera calibration
					A.xls	Excel file with grayscale values to temperature camera calibration
					Summary Output data.docx	Word file with test conditions
					Contour plot.dg6	Delta graph with nusselt number contour plot
					Local Nu.xls	Excel file contains local nusselt number
					Line area avg Nu.xls	Excel file contains line and area averaged nusselt number
exp50	20000	12.0	3.0	3.5	d_nu1.txt	Raw Nusselt number in text data file
					total.bmp	Average IR camera bitmap image for camera calibration
					A.xls	Excel file with grayscale values to temperature camera calibration
					Summary Output data.docx	Word file with test conditions
					Contour plot.dg6	Delta graph with nusselt number contour plot
					Local Nu.xls	Excel file contains local nusselt number
					Line area avg Nu.xls	Excel file contains line and area averaged nusselt number
exp51	20000	12.0	5.0	3.5	d_nu1.txt	Raw Nusselt number in text data file
					total.bmp	Average IR camera bitmap image for camera calibration

					A.xls	Excel file with grayscale values to temperature camera calibration
					Summary Output data.docx	Word file with test conditions
					Contour plot.dg6	Delta graph with nusselt number contour plot
					Local Nu.xls	Excel file contains local nusselt number
					Line area avg Nu.xls	Excel file contains line and area averaged nusselt number
exp52	20000	12.0	8.0	3.5	d_nu1.txt	Raw Nusselt number in text data file
					total.bmp	Average IR camera bitmap image for camera calibration
					A.xls	Excel file with grayscale values to temperature camera calibration
					Summary Output data.docx	Word file with test conditions
					Contour plot.dg6	Delta graph with nusselt number contour plot
					Local Nu.xls	Excel file contains local nusselt number
					Line area avg Nu.xls	Excel file contains line and area averaged nusselt number
exp53	30000	12.0	1.5	3.5	d_nu1.txt	Raw Nusselt number in text data file
					total.bmp	Average IR camera bitmap image for camera calibration
					A.xls	Excel file with grayscale values to temperature camera calibration
					Summary Output data.docx	Word file with test conditions
					Contour plot.dg6	Delta graph with nusselt number contour plot
					Local Nu.xls	Excel file contains local nusselt number

					Line area avg Nu.xls	Excel file contains line and area averaged nusselt number
exp54	30000	12.0	3.0	3.5	d_nu1.txt	Raw Nusselt number in text data file
					total.bmp	Average IR camera bitmap image for camera calibration
					A.xls	Excel file with grayscale values to temperature camera calibration
					Summary Output data.docx	Word file with test conditions
					Contour plot.dg6	Delta graph with nusselt number contour plot
					Local Nu.xls	Excel file contains local nusselt number
					Line area avg Nu.xls	Excel file contains line and area averaged nusselt number
exp55	30000	12.0	5.0	3.5	d_nu1.txt	Raw Nusselt number in text data file
					total.bmp	Average IR camera bitmap image for camera calibration
					A.xls	Excel file with grayscale values to temperature camera calibration
					Summary Output data.docx	Word file with test conditions
					Contour plot.dg6	Delta graph with nusselt number contour plot
					Local Nu.xls	Excel file contains local nusselt number
					Line area avg Nu.xls	Excel file contains line and area averaged nusselt number
exp56	30000	12.0	8.0	3.5	d_nu1.txt	Raw Nusselt number in text data file
					total.bmp	Average IR camera bitmap image for camera calibration
					A.xls	Excel file with grayscale values to temperature camera calibration

					Summary Output data.docx	Word file with test conditions
					Contour plot.dg6	Delta graph with nusselt number contour plot
					Local Nu.xls	Excel file contains local nusselt number
					Line area avg Nu.xls	Excel file contains line and area averaged nusselt number
exp57	50000	12.0	1.5	3.5	d_nu1.txt	Raw Nusselt number in text data file
					total.bmp	Average IR camera bitmap image for camera calibration
					A.xls	Excel file with grayscale values to temperature camera calibration
					Summary Output data.docx	Word file with test conditions
					Contour plot.dg6	Delta graph with nusselt number contour plot
					Local Nu.xls	Excel file contains local nusselt number
exp58	50000	12.0	3.0	3.5	d_nu1.txt	Raw Nusselt number in text data file
					total.bmp	Average IR camera bitmap image for camera calibration
					A.xls	Excel file with grayscale values to temperature camera calibration
					Summary Output data.docx	Word file with test conditions
					Contour plot.dg6	Delta graph with nusselt number contour plot
					Local Nu.xls	Excel file contains local nusselt number
exp59	50000	12.0	5.0	3.5	d_nu1.txt	Raw Nusselt number in text data file
					total.bmp	Average IR camera bitmap image for camera calibration
					A.xls	Excel file with grayscale values to temperature camera calibration

					Summary Output data.docx	Word file with test conditions
					Contour plot.dg6	Delta graph with nusselt number contour plot
					Local Nu.xls	Excel file contains local nusselt number
exp60	50000	12.0	8.0	3.5	d_nu1.txt	Raw Nusselt number in text data file
					total.bmp	Average IR camera bitmap image for camera calibration
					A.xls	Excel file with grayscale values to temperature camera calibration
					Summary Output data.docx	Word file with test conditions
					Contour plot.dg6	Delta graph with nusselt number contour plot
					Local Nu.xls	Excel file contains local nusselt number

3. Listing of experimental data files for impingement array heat transfer with large hole spacing

Folder name	Rej	Hole Spacing (X/D=Y/D)	Z/D	D (mm)	Data file name	Description
exp61	8000	12.0	1.5	3.5	d_nu1.txt	Raw Nusselt number in text data file
					total.bmp	Average IR camera bitmap image for camera calibration
					A.xls	Excel file with grayscale values to temperature camera calibration
					Summary Output data.docx	Word file with test conditions
					Contour plot.dg6	Delta graph with nusselt number contour plot
					Local Nu.xls	Excel file contains local nusselt number
					Line area avg Nu.xls	Excel file contains line and area averaged nusselt number
exp62	8000	12.0	3.0	3.5	d_nu1.txt	Raw Nusselt number in text data file
					total.bmp	Average IR camera bitmap image for camera calibration
					A.xls	Excel file with grayscale values to temperature camera calibration
					Summary Output data.docx	Word file with test conditions
					Contour plot.dg6	Delta graph with nusselt number contour plot
					Local Nu.xls	Excel file contains local nusselt number
					Line area avg Nu.xls	Excel file contains line and area averaged nusselt number
exp63	8000	12.0	5.0	3.5	d_nu1.txt	Raw Nusselt number in text data file
					total.bmp	Average IR camera bitmap image for camera calibration

					A.xls	Excel file with grayscale values to temperature camera calibration
					Summary Output data.docx	Word file with test conditions
					Contour plot.dg6	Delta graph with nusselt number contour plot
					Local Nu.xls	Excel file contains local nusselt number
					Line area avg Nu.xls	Excel file contains line and area averaged nusselt number
exp64	8000	12.0	8.0	3.5	d_nu1.txt	Raw Nusselt number in text data file
					total.bmp	Average IR camera bitmap image for camera calibration
					A.xls	Excel file with grayscale values to temperature camera calibration
					Summary Output data.docx	Word file with test conditions
					Contour plot.dg6	Delta graph with nusselt number contour plot
					Local Nu.xls	Excel file contains local nusselt number
					Line area avg Nu.xls	Excel file contains line and area averaged nusselt number
exp65	20000	12.0	1.5	3.5	d_nu1.txt	Raw Nusselt number in text data file
					total.bmp	Average IR camera bitmap image for camera calibration
					A.xls	Excel file with grayscale values to temperature camera calibration
					Summary Output data.docx	Word file with test conditions
					Contour plot.dg6	Delta graph with nusselt number contour plot
					Local Nu.xls	Excel file contains local nusselt number

					Line area avg Nu.xls	Excel file contains line and area averaged nusselt number
exp66	20000	12.0	3.0	3.5	d_nu1.txt	Raw Nusselt number in text data file
					total.bmp	Average IR camera bitmap image for camera calibration
					A.xls	Excel file with grayscale values to temperature camera calibration
					Summary Output data.docx	Word file with test conditions
					Contour plot.dg6	Delta graph with nusselt number contour plot
					Local Nu.xls	Excel file contains local nusselt number
					Line area avg Nu.xls	Excel file contains line and area averaged nusselt number
exp67	20000	12.0	5.0	3.5	d_nu1.txt	Raw Nusselt number in text data file
					total.bmp	Average IR camera bitmap image for camera calibration
					A.xls	Excel file with grayscale values to temperature camera calibration
					Summary Output data.docx	Word file with test conditions
					Contour plot.dg6	Delta graph with nusselt number contour plot
					Local Nu.xls	Excel file contains local nusselt number
					Line area avg Nu.xls	Excel file contains line and area averaged nusselt number
exp68	20000	12.0	8.0	3.5	d_nu1.txt	Raw Nusselt number in text data file
					total.bmp	Average IR camera bitmap image for camera calibration
					A.xls	Excel file with grayscale values to temperature camera calibration

					Summary Output data.docx	Word file with test conditions
					Contour plot.dg6	Delta graph with nusselt number contour plot
					Local Nu.xls	Excel file contains local nusselt number
					Line area avg Nu.xls	Excel file contains line and area averaged nusselt number
exp69	30000	12.0	1.5	3.5	d_nu1.txt	Raw Nusselt number in text data file
					total.bmp	Average IR camera bitmap image for camera calibration
					A.xls	Excel file with grayscale values to temperature camera calibration
					Summary Output data.docx	Word file with test conditions
					Contour plot.dg6	Delta graph with nusselt number contour plot
					Local Nu.xls	Excel file contains local nusselt number
					Line area avg Nu.xls	Excel file contains line and area averaged nusselt number
exp70	30000	12.0	3.0	3.5	d_nu1.txt	Raw Nusselt number in text data file
					total.bmp	Average IR camera bitmap image for camera calibration
					A.xls	Excel file with grayscale values to temperature camera calibration
					Summary Output data.docx	Word file with test conditions
					Contour plot.dg6	Delta graph with nusselt number contour plot
					Local Nu.xls	Excel file contains local nusselt number
					Line area avg Nu.xls	Excel file contains line and area averaged nusselt number
exp71	30000	12.0	5.0	3.5	d_nu1.txt	Raw Nusselt number in text data file

					total.bmp	Average IR camera bitmap image for camera calibration
					A.xls	Excel file with grayscale values to temperature camera calibration
					Summary Output data.docx	Word file with test conditions
					Contour plot.dg6	Delta graph with nusselt number contour plot
					Local Nu.xls	Excel file contains local nusselt number
					Line area avg Nu.xls	Excel file contains line and area averaged nusselt number
exp72	30000	12.0	8.0	3.5	d_nu1.txt	Raw Nusselt number in text data file
					total.bmp	Average IR camera bitmap image for camera calibration
					A.xls	Excel file with grayscale values to temperature camera calibration
					Summary Output data.docx	Word file with test conditions
					Contour plot.dg6	Delta graph with nusselt number contour plot
					Local Nu.xls	Excel file contains local nusselt number
					Line area avg Nu.xls	Excel file contains line and area averaged nusselt number
exp73	50000	12.0	1.5	3.5	d_nu1.txt	Raw Nusselt number in text data file
					total.bmp	Average IR camera bitmap image for camera calibration
					A.xls	Excel file with grayscale values to temperature camera calibration
					Summary Output data.docx	Word file with test conditions
					Contour plot.dg6	Delta graph with nusselt number contour plot

					Local Nu.xls	Excel file contains local nusselt number
exp74	50000	12.0	3.0	3.5	d_nu1.txt	Raw Nusselt number in text data file
					total.bmp	Average IR camera bitmap image for camera calibration
					A.xls	Excel file with grayscale values to temperature camera calibration
					Summary Output data.docx	Word file with test conditions
					Contour plot.dg6	Delta graph with nusselt number contour plot
					Local Nu.xls	Excel file contains local nusselt number
exp75	50000	12.0	5.0	3.5	d_nu1.txt	Raw Nusselt number in text data file
					total.bmp	Average IR camera bitmap image for camera calibration
					A.xls	Excel file with grayscale values to temperature camera calibration
					Summary Output data.docx	Word file with test conditions
					Contour plot.dg6	Delta graph with nusselt number contour plot
					Local Nu.xls	Excel file contains local nusselt number
exp76	50000	12.0	8.0	3.5	d_nu1.txt	Raw Nusselt number in text data file
					total.bmp	Average IR camera bitmap image for camera calibration
					A.xls	Excel file with grayscale values to temperature camera calibration

					Summary Output data.docx	Word file with test conditions
					Contour plot.dg6	Delta graph with nusselt number contour plot
					Local Nu.xls	Excel file contains local nusselt number

APPENDIX C

SOFTWARE DIRECTORY

This Appendix C provides a brief description of each of the different software used to acquire raw data at different experimental and numerical condition.

Software	File Name	Description
Exel	A.xls	Make greyscale calibration equation by using IR image data and thermocouple data.
Matlab	BB.m	Determine greyscale value for each IR image. Read IR image, and output greyscale values
Matlab	CC.m	Calculate the experimental heat transfer coefficient and Nusselt number
Labview	Flat plate impingement_cal.vi	This program is used to determine the pressures, the thermocouples temperature, mean hole velocity, jet stagnation temperature, jet static temperature, mass flow rate, hole Reynolds number, and hole Mach number. Used to Calibrate thermocouple and pressure transducer
DeltaGraph 6	Contour plot	Read and plot Nusselt numbers in contour format
WinIR	total.bmp	Record IR image as Bitmap image

REFERENCES

[1] Martin H., 1977, "Heat and Mass Transfer Between Impinging Gas Jets and Solid Surfaces," Advances in Heat Transfer, Academic Press, **13**, pp. 1-60.

[2] Schulz A., 2001, "Combustor Liner Cooling Technology In Scope of Reduced Pollutant Formation and Rising Thermal Efficiencies," Heat Transfer in Gas Turbine Systems, Annals of the New York Academy of Sciences, **934**, pp. 135-146.

[3] Kercher D. M., and Tabakoff W., 1970, "Heat Transfer By a Square Array of Round Air Jets Impinging Perpendicular to a Flat Surface Including the Effect of Spent Air," ASME Transactions-Journal of Engineering for Power, **92**, pp. 73-82.

[4] Metzger D. E., and Korstad R., 1972, "Effects of Crossflow On Impingement Heat Transfer," ASME Transactions-Journal of Engineering for Power, **94**, pp. 35-41.

[5] Chance J. L., 1974, "Experimental Investigation of Air Impingement Heat Transfer Under an Array of Round Jets," TAPPI, **57**, No. 6, pp. 108-112.

[6] Metzger D. E., Florschuetz L. W., Takeuchi D. I., Behee R. D., and Berry R. A., 1979, "Heat Transfer Characteristics for Inline and Staggered Arrays of Circular Jets With Crossflow of Spent Air," ASME Transactions-Journal of Heat Transfer, **101**, pp. 526-531.

[7] Florschuetz L. W., Truman C. R., and Metzger D. E., 1981, "Streamwise Flow and Heat Transfer Distributions for Jet Array Impingement With Crossflow," ASME Transactions–Journal of Heat Transfer, **103**, pp. 337-342.

[8] Obot N. T., and Trabold T. A., 1987, "Impingement Heat Transfer Within Arrays of Circular Jets: Part 1-Effects of Minimum, Intermediate, and Complete Crossflow for Small and Large Spacings", ASME Transactions-Journal of Heat Transfer, **109**, pp. 872-879.

[9] Bailey J. C., and Bunker R. S., 2002, "Local Heat Transfer and Flow Distributions For Impinging Jet Arrays of Dense and Sparse Extent," ASME Paper No. ASME GT-2002-30473.

[10] San J.Y., Tsou Y.M., and Chen Z.C., 2007, "Impingement Heat Transfer of Staggered Arrays of Air Jets Confined in a Channel," International Journal of Heat and Mass Transfer, **50**, No. 19-20, pp. 3718-3727.

[11] Miao J.M., Wu C.Y., and Chen. P.H., 2009, "Numerical Investigation of Confined Multiple-Jet Impingement Cooling over a Flat Plat at Different Crossflow Orientations," Numerical Heat Transfer, Part A: Applications: An International Journal of Computation and Methodology, **55**, No. 11, pp. 1019-1050.

[12] Vadiraj K., and Prabhu S.V., 2008, "Influence of Spanwise Pitch on Local Heat Transfer Distribution for In-Line Arrays of Circular Jets with Spent Air Flow in Two Opposite Directions," Experimental Thermal and Fluid Science, **33**, pp. 84-95.

[13] Brevet P., Dejeu C., Dorignac E., Jolly M., and Vullierme J. J., 2002, "Heat Transfer to a Row of Impinging Jets In Consideration of Optimization," International Journal of Heat and Mass Transfer, **45**, pp. 4191-4200.

[14] Kline S. J., and McClintock F. A., 1953, "Describing Uncertainties in Single Sample Experiments," Mechanical Engineering, **75**, pp. 3-8.

[15] Moffat R. J., 1988, "Describing the Uncertainties in Experimental Results," Experimental Thermal and Fluid Science, **1**, No. 1, pp. 3-17.

[16] Park J., Goodro M., Ligrani P. M., Fox M., and Moon H.-K., 2007, "Separate Effects of Mach Number and Reynolds Number on Jet Array Impingement Heat Transfer," ASME Transactions-Journal of Turbomachinery, **129** (2), pp. 269-280.

[17] Goodro M., Ligrani P. M., Fox M., and Moon H.-K., 2010, "Mach Number, Reynolds Number, Jet Spacing Variations: Full Array of Impinging Jets," AIAA Journal of Thermophysics and Heat Transfer, **24** (1), pp. 133-144.

[18] Awasthi, M. K., 2014, "Study on Kelvin-Helmholtz Instability With Heat and Mass Transfer," ASME Transactions-Journal of Fluids Engineering, **136** (12), p. 121202-1 to 121202-9.

[19] Moatimid, G. M., and Hassan, M. A., 2013, "Three-Dimensional Viscous Potential Electrohydrodynamic Kelvin–Helmholtz Instability through Vertical Cylindrical Porous Inclusions with Permeable Boundaries," ASME Transactions-Journal of Fluids Engineering, **136** (2), pp. 021203-1 to 021203-10.

[20] Yang, L., Ligrani, P. M., Ren, J., and Jiang, H., 2015, "Unsteady Structure and Development of a Row of Impingement Jets, Including Kelvin–Helmholtz Vortex Development," ASME Transactions-Journal of Fluids Engineering, **137** (5), pp. 051201-1 to 051201-12.

[21] D. M. Kercher, W. Tabakoff, Heat transfer by a square array of round air jets Impinging perpendicular to a flat surface including the effect of spent air, ASME Transactions-Journal of Engineering for Power 92 (1970) 73-82.

[22] R. Chupp, H. Helms, P. McFadden, T. Brown, Evaluation of internal heat-transfer Coefficients for impingement cooled turbine airfoils, AIAA-Journal of Aircraft 6(3) (1969) 203-208.

[23] D. E. Metzger, R. Korstad, Effects of crossflow on impingement heat transfer, ASME Transactions-Journal of Engineering for Power 94 (1972) 35-41.

[24] J. Park, M. Goodro, P. M. Ligrani, M. Fox, H. K. Moon, Separate effects of Mach number and Reynolds number on jet array impingement heat transfer, ASME Transactions-Journal of Turbomachinery 129(2) (2007) 269-280.

[25] Y. M. Chung, K. H. Luo, Unsteady heat transfer analysis on an impinging jet, ASME Transactions-Journal of Heat Transfer 124 (2002) 1039-1048.

[26] D. H. Lee, H. J. Park, P. M. Ligrani, Visualization and structure of confined, milliscale, unsteady impinging slot jets and associated vortices, Experiments in Fluids 54 (2013) 1420-1434.

[27] C. O. Popiel, O. Trass, Visualization of a free and impinging round jet, Experimental Thermal and Fluid Science 4 (1992) 106-115.

[28] M. Angioletti, R. M. Di Tommaso, E. Nino, G. Ruocco, Simultaneous visualization of flow field and evaluation of local heat transfer by transitional impinging jets, International Journal of Heat and Mass Transfer 46 (2003) 1703-1713.

[29] T. S. O'Donovan, D. B. Murray, Jet impingement heat transfer - Part II: A temporal investigation of heat transfer and local fluid velocities, International Journal of Heat and Mass Transfer 50 (2007) 3302-3314.

[30] M. D. Fox, M. Kurosaka, L. Hedges, K. Hirano, The influence of vertical structures on the thermal fields of jets, Journal of Fluid Mechanics 255 (1993) 447-472.

[31] J. Lee, Z. Ren, J. Haegele, G. Potts, J. S. Jin, P. M. Ligrani, M. Fox, H.-K. Moon, Effects of jet-to-target plate distance and Reynolds number on jet array impingement Heat transfer, ASME Transactions-Journal of Turbomachinery (2014) to appear.

[32] L. Yang, J. Ren, H. Jiang, P. M. Ligrani, Experimental and numerical investigation of unsteady impingement cooling within a blade leading edge passage, International Journal of Heat and Mass Transfer 71 (2014) 57-68.

[33] R. Chauhan, N. S. Thakur, Heat transfer and friction factor correlations for impingement jet solar air heater, Experimental Thermal and Fluid Science 44 (2013) 760-767.

[34] L. Gao, Effect of jet hole arrays arrangement on impingement heat transfer, M.S. Thesis, Mechanical Engineering Department, Louisiana State University (2003).